

UCSB ATR-2 2016-1

Update on the High Fluence Advanced Test Reactor – 2 Reactor Pressure Vessel High Fluence Irradiation Project

Prepared by

G. R. Odette, T. Yamamoto, P. B. Wells, N. Almirall, K.
Fields, D. Gragg

University of California, Santa Barbara

and

R. K. Nanstad, M. A. Sokolov, J. P. Robertson
Oak Ridge National Laboratory

Document Completed: June 30, 2016

Prepared for

Dr. Keith Leonard (ORNL)

Dr. Katherine McCarthy (INL)

Dr. Richard Reister (DOE)

Disclaimer

This report was prepared as an account of work sponsored by an agency of the United States Government. Neither the United States Government nor any agency thereof, nor any of their employees, makes any warranty, express or implied, or assumes any legal liability or responsibility for the accuracy, completeness, or usefulness of any information, apparatus, product, or process disclosed, or represents that its use would not infringe privately owned rights. The above also applies to UCSB as an ORNL subcontractor. Reference herein to any specific commercial product, process, or service by trade name, trademark, manufacturer, or otherwise, does not necessarily constitute or imply its endorsement, recommendation, or favoring by the United States Government or any agency thereof. The views and opinions of authors expressed herein do not necessarily state or reflect those of the United States Government or any agency thereof.

Contents

Contents	iii
List of Figures.....	v
List of Tables	viii
Acknowledgements	ix
1. Introduction	1
1.1 Background – Reactor Pressure Vessel Embrittlement	1
1.2 Materials	8
1.2.1 UCSB Split Melt and Model Alloys	9
1.2.2 Surveillance and Program Alloy Matrix.....	10
1.3 Irradiation Conditions	12
1.4 Mechanical Property Testing	13
1.4.1 Hardness Testing	13
1.4.2 Tensile Testing	14
1.4.3 Shear Punch Testing	16
1.4.4 Automated Shear Punch Testing	19
1.5 Microstructural Characterization	20
1.5.1 Atom Probe Tomography	21
1.5.2 Small Angle Neutron Scattering.....	25
1.5.3 Small Angle x-ray Scattering (SAXS)	28
2. Results	30
2.1 Surveillance Steels	30
2.1.1 Mechanical Properties	30
2.1.2 Small Angle Neutron Scattering.....	34
2.2 UCSB Split Melt Steels and Program Alloys	36
2.2.1 Mechanical Properties	36
2.2.2 Atom Probe Tomography	37
2.2.3 Examples of Preliminary SAXS Results	39
3. Data Analysis and Evaluation	41
3.1 Property-Property Correlations	41
3.1.1 Shear Yield – Tensile Yield	41
3.1.2 Microhardness – Yield Stress Correlations	42
3.2 Microstructure-Property Correlations	43
3.3 Comparison with Surveillance Programs	44
3.4 Comparisons with Previous Test Reactor Data	48
3.5 The Effect of Chemistry on Precipitation and Hardening	50
3.5.1 Effect of Ni	51
3.5.2 Effect of Mn	52
3.5.3 Effect of P	52

3.6	Comparison of New ATR-2 Data to Previously Derived Microstructurally Based $\Delta\sigma_y$ Models	55
4.	TTS Predictions	58
5.	Summary and Future Work	60
6.	References	62

List of Figures

Figure 1.1 Predicted versus measured ΔT as a function of neutron fluence for RPV steels irradiated in test reactors, from [5].	3
Figure 1.2 Flux-fluence map for the UCSB embrittlement database including the large NRC sponsored UCSB IVAR program completed about a decade ago and the more recent NSUF sponsored high flux-high fluence ATR-1 irradiation that contained a matrix of RPV steels.	7
Figure 1.3 Schematic of the tensile loading box (left) and SSJ-2 tensile specimens (right). Note that half of the specimens have a gauge length of 5.00 mm (showed), while the others have a 2.2 mm gauge length.	15
Figure 1.4 Example stress-strain curve with 0.2% offset line.	16
Figure 1.5 Schematic of the single specimen punch shear punch tester.	17
Figure 1.6 A typical shear punch curve [9].	18
Figure 1.7 σ_y versus τ_y for steels with a wide range of yield strengths showing the empirical relation $\sigma_y \approx 1.77 \tau_y$ [9].	18
Figure 1.8 Automated shear punch instrument showing footprint on a lab bench.	20
Figure 1.9 Schematic of a Local Electrode Atom Probe. Note that it is not to scale [10].	22
Figure 1.10 SANS experimental setup.	26
Figure 1.11 XPD beamline end station C.	29
Figure 2.1 Stress-strain curves for the surveillance weld SW6 from the baseline and cup 7 irradiated conditions.	31
Figure 2.2 Baseline SPT curves for the surveillance alloy SW6.	34
Figure 2.3 Absolute scattering curves taken at a 45° angle with respect to the magnetic field for the surveillance weld SW2 showing the extra scattering in the cup 7 irradiated condition due to formation of precipitates.	35
Figure 2.4 Stress-strain curves for two alloys, LG and LC, from the cup 7 (red) and baseline (blue) conditions.	36
Figure 2.5 Cup 7 APT atom maps from a low Cu, medium Ni steel (LG) and a high Cu, medium Ni steel (LC), showing large volume fractions of (Cu)-Mn-Ni-Si precipitates.	38
Figure 2.6 Atom map from the 0.41%Cu, 0.84%Ni alloy with Cu (green) and Mn-Ni-Si (Pink) isosurfaces (left) and a 1-dimensional concentration profile through a precipitate showing separate Cu and Mn-Ni-Si rich regions (right).	39
Figure 2.7 Representative SAXS patterns for unirradiated and ATR-2 irradiated CM samples. The curves are offset for clarity.	40
Figure 2.8 Quantitative SAXS results for 3 CM-series alloys.	40
Figure 3.1 Tensile versus shear yield stress for a matrix of Rolls Royce alloys (red) that were previously tested, and a matrix of surveillance and Rolls Royce alloys tested recently as part of this experiment (blue).	42

Figure 3.2 Change in tensile yield stress versus change in microhardness for a subset of surveillance alloys in cup 7.	43
Figure 3.3 Hardening versus square root of precipitate volume fraction for surveillance alloys (red), measured by SANS, and UCSB SMS (blue), measured by APT.	44
Figure 3.4 Comparison between UCSB and surveillance unirradiated baseline data for σ_y (left) and s_u (right).	45
Figure 3.5 $\Delta\sigma_y$ versus fluence for the 9 new surveillance alloys with < 0.07 wt.% Cu (left) and > 0.07 wt.% Cu (right).	46
Figure 3.6 ATR-2 cup 7 hardening for various surveillance alloys along with predictions from existing models.	47
Figure 3.7 ATR-2 cup 7 hardening for the UCSB SMS and program alloys along with predictions from existing models.	48
Figure 3.8 $\Delta\sigma_y$ versus the square root of fluence (left) and effective fluence (right) for two high Cu ($\approx 0.4\%$), steels with 0.86%Ni (top) and 1.25%Ni (bottom) from the UCSB SMS matrix for a wide number of irradiation condition.	49
Figure 3.9 $\Delta\sigma_y$ versus the square root of fluence (left) and effective fluence (right) for two low Cu ($\approx 0.01\%$), steels with 0.74%Ni (top) and 1.68%Ni (bottom) from the UCSB SMS matrix for a wide number of irradiation condition	50
Figure 3.10 $\Delta\sigma_y$ versus Cu content at either 0.8%Ni (left) or 1.6%Ni (right) for two different conditions from the IVAR experiment (T6 and T16) and cup 7 from the ATR-2 experiment.	51
Figure 3.11 $\Delta\sigma_y$ versus Ni content at either 0.0%Cu (left) or 0.4%Ni (right) for two different conditions from the IVAR experiment (T6 and T16) and cup 7 from the ATR-2 experiment.	51
Figure 3.12 $\Delta\sigma_y$ versus Mn content at either 0.0%Cu (left) or 0.4%Cu (right) for two different conditions from the IVAR experiment (T6 and T16) and cup 7 from the ATR-2 experiment.	52
Figure 3.13 $\Delta\sigma_y$ versus P content at 0%Cu, 1.6%Mn and either 0.8%Ni (left) or 1.6%Ni (right) for two different conditions from the IVAR experiment (T6 and T16) and cup 7 from the ATR-2 experiment.	53
Figure 3.14 Square root of measured APT volume fraction versus square root of (2*Ni+Cu) determined by measuring the local APT bulk composition.	54
Figure 3.15 $\Delta\sigma_y$ versus a chemistry factor (CF) currently under development to predict hardening from an alloy's bulk composition for the surveillance alloys (blue) and UCSB SMS (pink).	55
Figure 3.16 Preliminary UCSB Avrami model predicting f_p as a function of fluence for the core UCSB SMS. The ATR-2 data points (shown in large red circles) were not used in the fitting of the model.	57
Figure 3.17 Preliminary UCSB Avrami model predicting $\Delta\sigma_y$ as a function of fluence for the core UCSB SMS. The ATR-2 data points (shown in large red circles) were not used in the fitting of the model.	58

Figure 4.1 Charpy measured ΔT versus tensile measured $\Delta\sigma_y$ for surveillance specimens from REAP database showing different correlations for base metals and welds along with correlations developed by Odette et al. 59

Figure 4.2 ΔT versus fluence for measured ΔT from surveillance programs (blue), measured $\Delta\sigma_y$ converted to ΔT using the Odette et al. correlations (green), and the ATR-2 $\Delta\mu H$ converted to ΔT (red) for a surveillance plate (left) and weld (right). 60

List of Tables

Table 1.1 Composition of UCSB split melt steels included in the tensile matrix.	10
Table 1.2 Composition (wt.%) of surveillance alloys.	11
Table 1.3 Composition (wt.%) of program alloys.	11
Table 1.4 Neutron flux, fluence ($E > 1$ MeV) and temperature for the various cups in the ATR-2 irradiation.	13
Table 1.5 Summary of tested and remaining specimens in tensile matrix. Note all conditions are at 290°C.	14
Table 2.1 Summary of the tested surveillance and program alloys in the baseline and cup 7 irradiated conditions.	32
Table 2.2 Microhardness data taken at ORNL for 11 surveillance alloys in the baseline and cup 7 irradiated conditions.	33
Table 2.3 Microhardness data taken at ORNL for 4 program alloys in the baseline and cup 7 irradiated conditions.	33
Table 2.4 Shear yield (τ_y) and ultimate stress (s_{max}) for the baseline surveillance alloys.	34
Table 2.5 SANS results for the surveillance alloys from cup 7 showing the average precipitate radius ($\langle r \rangle$), number density (N_p), volume fraction (f_p) and magnetic-to-nuclear scattering ratio (M/N).	35
Table 2.6 Yield strengths for baseline and cup7 irradiated UCSB SMS.	37
Table 2.7 Atom Probe Tomography data for the UCSB SMS from Cup 7.	39
Table 2.8 Fitted SAXS $\langle d_p \rangle$ (nm) and f_p (%) for 3 CM-series alloys and their compositionally similar L-series counterparts measured by APT.	41
Table 5.1 Summary of remaining alloys/samples each in condition as well as remaining tests to complete.	62

Acknowledgements

We wish to acknowledge many other individuals who have contributed to this work. First and foremost, the ATR-2 irradiation was made possible by NSUF and the outstanding team of scientists, engineers and managers at INL led by Michel Meyer, and including Michael Sprenger, Paul Murray, Joseph Nielson, Collin Knight, Thomas Maddock, Dan Ogden, James Cole, Todd Allen and Rory Kennedy. Other contributors include Keith Wilford and Tim Williams at Rolls Royce, Keith Leonard and Phil Edmondson at ORNL, William Server at ATI consulting, Lynne Ecker and David Sprouster at BNL, Timothy Hardin at EPRI, Grace Burke and Raymond Stofanak at BMPC, and Naoki Soneda at CRIEPI. We would also like to acknowledge the support of the National Institute of Standards and Technology (NIST) for providing the neutron research facilities to conduct the SANS studies and specifically John Barker for his significant help in conducting these experiments. We would also like to acknowledge the Center for Advanced Energy Studies (CAES) Microscopy and Characterization Suite (MaCS) where the sample preparation for Atom Probe Tomography was completed, including Jatu Burns, Allyssa Bateman, and Joanna Taylor who significantly contributed to this process. Many other individuals at UCSB also contributed most notably Doug Klingensmith, Nicholas Cunningham and Yuan Wu. The work was financially supported by DOE through the NSUF, NEUP and LWRS Program (via ORNL).

Executive Summary

The overarching goal of the UCSB ATR-2 irradiation experiment is to provide a foundational database for developing new physical models to predict embrittlement of reactor pressure vessel steels at high fluence for extended life operation. The irradiation was carried out in the Advanced Test Reactor at the Idaho National Laboratory, sponsored by the National Scientific User Facilities Program. This report focuses on the initial results of post irradiation examination (PIE) of a small subset of 1625 specimens of various types in ATR-2, representing 172 alloys, neutron irradiated over a range of flux (ϕ), fluence (ϕt) and temperature. The ATR-2 irradiation was highly successful and, even at this early stage, the PIE program is meeting key scientific and engineering objectives. Most notably, embrittlement at 1.4×10^{20} n/cm² and 290°C, as manifested by irradiation hardening, is generally systematically and significantly under-predicted by current regulatory models, including both the Eason-Odette- Nanstad-Yamamoto (EONY) model and the new American Society for Testing and Materials (ASTM) E900 Standard.

The initial microstructural characterization by atom probe tomography and small angle neutron and x-ray scattering shows that the high fluence hardening includes a significant contribution from so-called late blooming phases (LBP) in the form of nano-scale Mn-Ni-Si precipitates (MNSP). The work shows that MNSP LBP emerge at high fluence in both Cu-bearing and nearly Cu-free RPV steels, and in both intermediate and high Ni steels. Note, the E900 model grossly over-predicts embrittlement in very high 1.6% Ni steels, while under-predicting hardening experiment at < 1% Ni. More generally, the alloy compositional dependence at high fluence can be approximately treated by a chemistry factor that is a function of only Cu and Ni. The most important tentative conclusion is that, while late blooming MNSP will likely make a significant contribution to embrittlement under extended

life conditions that must be accounted for, it appears that their absolute contributions will be manageable for a majority of vessels in the US PWR fleet.

The ATR-2 irradiation was carried out at an intermediate flux that is ≈ 10 times the maximum level in the surveillance database and ≈ 70 times higher than vessel fluxes that will reach 10^{20} n/cm² in 80 full power years. Thus flux effects must be considered and characterizing the dependence of hardening on dose rate is another high priority of ATR-2 study. Hence, ATR-2 was designed to bridge the very large embrittlement existing databases developed by UCSB and others covering low flux surveillance to very high flux test reactor conditions. The early PIE results reported here also demonstrate how hardening measurements are related to one another and how that can be translated to transition temperature shifts.

In contrast to the EONY and ATM E900 treatments, the initial microstructural and mechanical property PIE are in remarkable quantitative agreement with previously developed physically based models, showing the predicted formation of late blooming Mn-Ni-Si phases and supporting the treatment of flux effects. The combined database will quantify the “when (flux and fluence), where (alloy compositions) and how much (hardening-shift contributions) of late blooming phases that are not treated in current regulatory models. In addition, UCSB ATR-2 will provide: (a) a test of the validity of the Master Curve fracture toughness assessment method in highly embrittled steels; (b) a large database on post irradiation annealing as a foundation for developing embrittlement remediation methods; and, (c) support for the development of a new class of high Ni advanced RPV alloys. The ATR-2 PIE program is also developing new mechanical property and microstructural characterization tools, such as an automated shear punch test tool and small angle x-ray scattering, respectively. Finally, the large ATR-2 experimental effort is being closely coupled to

fundamental models of embrittlement in way that experiments truly inform advanced modeling and uses modeling to guide efficient and targeted experiments.

1. Introduction

1.1 Background – Reactor Pressure Vessel Embrittlement

The rapid failure of the massive reactor pressure vessel (RPV) in a light-water reactor (LWR) is beyond a design basis accident, thus regulations require conservative fracture safe margins under both normal operation and accident conditions. Demonstrating such safety margins requires that the fracture toughness of the vessel steel be conservatively greater than any possible stress intensity factor due to loading of postulated cracks. In the unirradiated condition, RPV steels have high fracture toughness and vessel fracture is implausible under any postulated condition. However, in-service neutron irradiation degrades the fracture toughness of a RPV steels. Irradiation embrittlement depends on the combination of the sensitivity of the steel, controlled by compositional and starting microstructure metallurgical variables, and the irradiation condition, characterized by the flux and fluence of neutrons as well as irradiation temperature. In-service embrittlement effects are primarily quantified by shifting an unirradiated temperature dependent cleavage fracture toughness curve, for a vessel specific steel, by a temperature increment (ΔT), traditionally measured by corresponding shifts in Charpy V-notch (CVN) impact test energy temperature curves. More recently, ΔT for fracture toughness as a function of temperature Master Curves have been directly measured. Irradiation induced reductions in CVN upper shelf energy, or ductile tearing toughness also occur. Here we focus on developing accurate methods for predicting ΔT for low flux, high fluence extended life conditions.

Early recognition of the potential importance of RPV embrittlement led to including wall-mounted surveillance capsules in most US reactor vessels, nominally containing the most sensitive plant specific steels. Sets of surveillance steel CVN specimens, irradiated at a higher neutron flux than the vessel itself, are periodically removed and tested, to provide an

estimate of the ΔT that the RPV will experience at a later time. However, plant specific surveillance data is often not sufficient to predict the corresponding RPV ΔT [1]. Thus, regulatory models for ΔT as a function of metallurgical and irradiation variables have been developed based on large surveillance embrittlement databases, e.g. the Eason-Odette-Nanstad-Yamamoto model [2]. Physically motivated embrittlement models have been very successful in fitting the surveillance databases, but are explicitly limited to an intermediate neutron fluence that is less than one half the maximum expected during extended 80 year RPV life. Recently, the American Society Testing and Materials (ASTM) adopted an empirical ΔT fit (ASTM-E900) that is not formally restricted to intermediate fluence. However, it has been demonstrated that the ASTM E900 ΔT predictions are increasingly unreliable (and largely untested) at the higher fluence associated with extended RPV life [3, 4].

Unfortunately, there is almost no plant surveillance ΔT data for high neutron fluences at the long service times experienced during extended reactor life. Thus, test reactors, which can be used to irradiate materials to high fluence at high neutron flux in relatively short times, often have been used to investigate irradiation embrittlement. However as illustrated in Figure 1.1, and as is common with other surveillance-data based embrittlement formulations, the widely recognized Eason-Odette-Nanstad-Yamamoto model increasingly under-predicts ΔT for accelerated test reactor irradiations at higher fluence [5]. The ΔT under-prediction is due to a combination of flux effects, the fact that little surveillance data above a fluence of 5×10^{19} n/cm² was used to develop the EONY model, and the formation of new populations of hardening features at high fluence, primarily Mn-Ni-Si precipitates (MNSPs), or so called late blooming phases (LBP) [5].

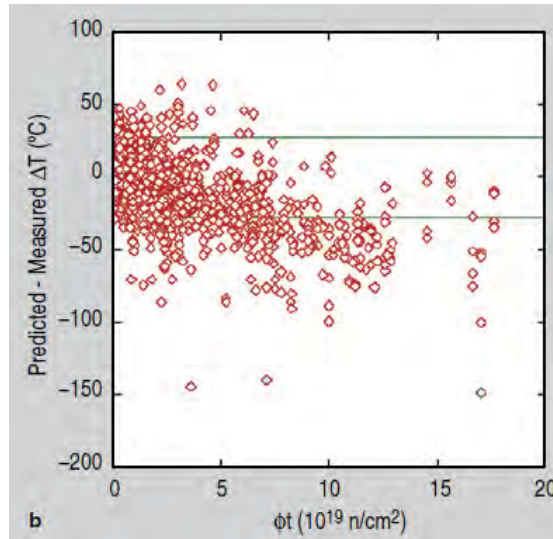


Figure 1.1 Predicted versus measured ΔT as a function of neutron fluence for RPV steels irradiated in test reactors, from [5].

Critical issues related to vessel integrity for extended operation that must be addressed in a timely fashion include:

- Accurate predictions of ΔT for *low-flux, high-fluence* conditions up to 80-full-power years of operation, largely in the absence of power reactor surveillance data.
- Proper use of accelerated test reactor data, that can reach high fluence, but that may be confounded by the effects of higher flux.
- Establishing the conditions for the formation of severely embrittling MNSP LBPs in both low and high Cu steels, and that are not explicitly treated in current regulatory models.
- Quantifying the potential for embrittlement remediation by post-irradiation annealing.
- Assessing the validity of the Master Curve Method in highly embrittled steels at high fluence.

Thus, a primary objective of the LWRS Program's ATR-2 materials irradiation task is to develop robust physical models to predict ΔT s at high-fluence (about 10^{20} n/cm² greater than 1 MeV) for vessel relevant fluxes pertinent to plant operation for 80 years. New features

of the models will include: (a) an improved treatment of flux effects in moderately accelerated test reactor irradiations that are needed to reach high fluence; (b) the influence of alloy composition on the development of MNSPs; and (c) other possible damage mechanisms that may be increasingly significant beyond a high incubation (threshold) fluence.

To address these issues, UCSB and its collaborators conceived, designed and carried out a very large, high-fluence, intermediate-flux irradiation experiment in the Idaho National Laboratory (INL) Advanced Test Reactor (ATR). This experiment, referred to as UCSB ATR-2, involved a multiyear irradiation of 1625 specimens, representing 172 RPV alloys in a variety of specimen configurations, over a range of irradiation temperatures and fluence. UCSB ATR-2 was sponsored by the National Scientific Users Facility (NSUF) program led by INL. The scientific and engineering objective of UCSB ATR-2 is to characterize RPV embrittlement in terms of irradiation hardening and the underlying hardening microstructure. As shown later in this report, irradiation induced increases in yield stress ($\Delta\sigma_y$) and related strength properties can be readily related to ΔT .

The report is organized as follows. We begin by a substantive, albeit far from detailed, description of the materials and experimental methods used in the post irradiation examination (PIE) research reported here, so that what we have done can be clearly understood. This section includes a description of the ATR-2 irradiation, which is the focus of this report. Many readers may choose to skip this section. The PIE results are then described in sections that encompass surveillance steels and other alloys, including split melt steels with controlled composition variations. After presenting the data, a section is devoted to analysis and evaluation of the significance of the results. The ATR-2 data analysis includes: a) property-property correlations; b) comparisons of the new data with various ΔT model predictions; c) corresponding comparisons with data from previous irradiations; d)

observations regarding composition and high-fluence effects (again by combining ATR-2 results with surveillance and other databases); and, e) comparisons of ATR-2 data with microstructurally based models. This is followed by a short section showing examples of how irradiation hardening based estimates of equivalent ATR-2 ΔT compare to actual surveillance shift data. The report concludes with a brief outline of future work.

2. Materials and Methods

2.1 The UCSB ATR-2 Irradiation and Post Irradiation Examination (PIE) Program

The main challenge associated with the development of an extended life embrittlement prediction model is that there is very little surveillance data at high fluence. To address this issue, a large-scale irradiation designed to reach a peak fluence of $> 1 \times 10^{20}$ n/cm² at an intermediate flux was carried out in the Advanced Test Reactor (ATR) at the Idaho National Laboratory (INL). The irradiation was proposed by the University of California, Santa Barbara (UCSB) in 2008 and awarded by NSUF in 2009.

The UCSB ATR-2 irradiation began in June of 2011 and was completed in January 2014. Specimens were delivered to Oak Ridge National Laboratory (ORNL) hot cells in August of 2015. The ATR-2 program involves an international consortium of participants including UCSB, ORNL, Rolls Royce (RR) in the United Kingdom, and the Electric Power Research Institute (EPRI). The Central Research Institute for the Electric Power Industry (CRIEPI) in Japan and Bechtel Marine Propulsion Corporation (BMPC) are in the process of joining the consortium. A number of US utilities also contributed surveillance base metals and welds to the ATR-2 irradiation.

UCSB and INL collaborated in the conceptual design of the irradiation test train. INL carried out the corresponding detailed engineering design and safety analysis, ultimately constructing and assembling a test train composed of the 13 thin-walled cups loaded at

UCSB. INL conducted the subsequent ATR irradiation. Preparatory work at UCSB was funded by DOE NEUP, NSUF and LWRSP (via ORNL) programs. The PIE to date has been funded by a residual NEUP grant, some remaining NSUF bridging funds, and now primarily by the LWRSP via ORNL. RR and EPRI are providing funding for a new alloy matrix and some surveillance steels, respectively. BMPC and CRIEPI will fund the PIE on steels that they contributed to the irradiation.

The test assembly included a thermal neutron shield and active temperature control in three zones for irradiations at nominal temperatures of ≈ 270 , 290 , and 310°C , plus one smaller zone at $\approx 250^\circ\text{C}$. The majority of the 172 RPV alloys in the experiment were provided by UCSB. ORNL and their subcontractor ATI Consulting acquired some surveillance base metals and welds. Other alloys were contributed by BMPC and CRIEPI. Notably, RR, who was a founding participant in the ATR-2 program, provided 50 new alloy compositions, along with 5 heat treatment variants. The RR matrix focuses on developing new, advanced high Ni steels and filling critical gaps in the database for existing vessels. A large number of other surveillance steels from various operating nuclear reactors were also included to enable a direct comparison between the intermediate flux ATR-2 and low flux power reactor surveillance irradiations.

UCSB fabricated and loaded 1,625 small specimens into the 13 thin walled-cups. The specimens included ≈ 400 sub-sized tensile specimens (SSJ-2 type), 1150 disc multipurpose coupons (DMC), and 50 disc compact tension (DCT) fracture specimens. The ATR-2 fluence ranged from $\approx 5 \times 10^{19}$ to 1.4×10^{20} n/cm². Note, not all the irradiation temperatures covered this entire fluence range, and the overall emphasis was on the 290°C condition. In this case, the target fluence ranged from approximately 40 to 80 years of LWR operation and bridges a

flux-fluence gap in the UCSB databases, as shown in Figure 1.2, which is needed to better understand extended life embrittlement.

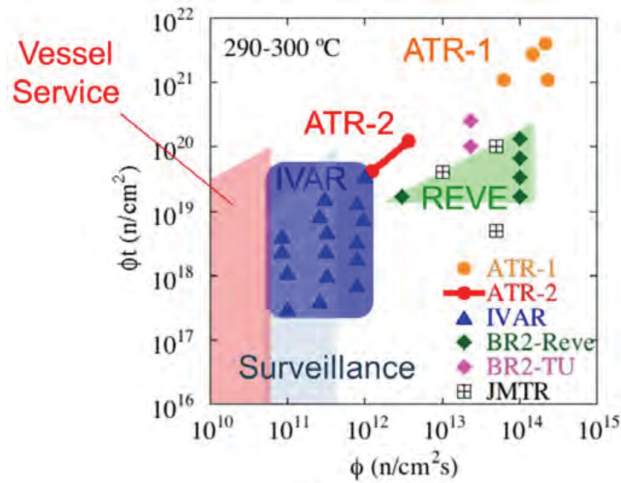


Figure 1.2 Flux-fluence map for the UCSB embrittlement database including the large NRC sponsored UCSB IVAR program completed about a decade ago and the more recent NSUF sponsored high flux-high fluence ATR-1 irradiation that contained a matrix of RPV steels.

The DMC support microhardness (μH), shear punch test (SPT) and a wide variety of microstructural characterization studies on all the alloys. The SST, DMC, μH and DCT specimens allow measurement and correlation of various property changes, including tensile yield stress, shear yield stress, microhardness, and the Master Curve (MC) ΔT and shape. In addition, the DCTs will further examine the validity of the assumed MC shape at extended life fluences, where large ΔT are expected.

The mechanical property measurements will be accompanied by extensive microstructural characterization studies, including: (a) small angle neutron scattering (SANS); (b) small angle x-ray scattering (SAXS) and x-ray diffraction (XRD); (c) resistivity-Seebeck coefficient (RSC) measurements; (d) atom probe tomography (APT); (e) positron annihilation spectroscopy (PAS); and (f) transmission electron microscopy (TEM). This suite of advanced characterization tools will be used to identify the detailed nature of various irradiation induced hardening features, especially late blooming phases.

The UCSB ATR-2 irradiation test assembly was completed in late spring of 2011 and was successfully installed in the ATR on May 26, 2011. The entire test assembly was shipped to ORNL in August 2015 and post irradiation examination (PIE) of the specimens began shortly thereafter.

In summary, a variety of relatively small specimens of many different RPV steels were irradiated in UCSB ATR-2 over a range of conditions. The specimens will be used to characterize both irradiation hardening and the underlying hardening microstructure. Most of these steels have been irradiated and tested in previous test reactor and surveillance programs over a wide range of flux, fluence and temperature conditions. The combined databases will be used to develop low-flux, high-fluence ΔT models.

1.2 Materials

A total of 172 alloys were included in the ATR-2 irradiation. These can broadly be split into 7 groups: UCSB split-melt steels, UCSB simple model alloys, UCSB acquired program alloys that have been included in other irradiations, UCSB and EPRI acquired surveillance steels, and the RR, CRIEPI and BMPC matrices. Each alloy matrix has a particular set of goals. The UCSB split melt steel matrix contains alloys with systematic variations in the main solute elements that dictate a material's sensitivity to irradiation embrittlement: Cu, Ni and Mn. The surveillance alloys will enable direct comparison of irradiation hardening at the intermediate test reactor ATR-2 flux with that for irradiations at much lower flux surveillance conditions. The RR matrix includes alloys that contain a much wider range of Ni and Mn contents than has previously been studied to develop better alloys for future RPV applications. The CREIPI and BMPC irradiations involve a smaller set of steels, but share generally similar objectives. The focus of the experiment to date has been on the UCSB split-melt steels and surveillance alloys, as well as selected RR steels, but the latter

will not be discussed further here. More details can be found elsewhere or in future reports [6].

1.2.1 UCSB Split Melt and Model Alloys

The UCSB matrix includes 34 split-melt steels (SMS) with systematic variations in Cu, Ni and Mn contents to investigate the individual and combined effects of these solutes. The SMS were processed and have microstructures and properties that are typical of A-533B steels used in RPVs. The SMS include the L and CM series, based on their supplier. The L and CM series are similar, but the CMs have a slightly larger base Mn content and a wider range of Ni. The compositions of a subset of the SMS, that were included in the experiment as tensile specimens, are given in Table 1.1. In addition to the SMS, 11 simple model ferritic alloys variously containing only Cu, Ni, Mn, Si and Mo were also included in the experiment, though have not been tested yet.

Table 1.1 Composition of UCSB split melt steels included in the tensile matrix.

Alloy Code	Cu									
	%	Ni%	Mn%	Cr%	Mo%	P%	C%	S%	Si%	Fe%
LB	0.40	0.18	1.35	0.06	0.53	0.005	0.16	0.005	0.22	97.10
LC	0.41	0.86	1.44	0.06	0.55	0.005	0.14	0.008	0.23	96.30
LD	0.38	1.25	1.38	0.06	0.53	0.005	0.19	0.015	0.23	96.02
LG	0.01	0.74	1.37	0.05	0.55	0.005	0.16	0.005	0.22	96.90
LH	0.11	0.74	1.39	0.09	0.55	0.005	0.16	0.005	0.24	96.72
LI	0.20	0.74	1.37	0.09	0.55	0.005	0.16	0.005	0.24	96.65
LJ	0.42	0.81	1.34	0.05	0.56	0.005	0.13	0.005	0.13	96.56
CM3	0.02	0.85	1.60	0.00	0.49	0.006	0.13	0.000	0.16	96.74
CM5	0.02	0.86	1.61	0.04	0.53	0.050	0.15	0.000	0.16	96.58
CM6	0.02	1.68	1.50	0.05	0.54	0.007	0.15	0.003	0.17	95.88
CM7	0.00	1.70	1.55	0.05	0.56	0.047	0.16	0.003	0.17	95.76
CM9	0.01	0.86	0.85	0.04	0.55	0.003	0.15	0.003	0.15	97.38
CM10	0.02	0.88	1.66	0.05	0.53	0.008	0.16	0.004	0.17	96.52
CM11	0.34	0.85	1.64	0.02	0.53	0.006	0.15	0.003	0.18	96.28
CM16	0.22	0.82	1.58	0.00	0.51	0.004	0.16	0.000	0.25	96.46
CM17	0.22	1.59	1.54	0.00	0.50	0.004	0.16	0.000	0.25	95.74
CM19	0.42	0.85	1.63	0.01	0.51	0.005	0.16	0.003	0.16	96.25
CM20	0.43	1.69	1.63	0.02	0.50	0.006	0.16	0.003	0.16	95.40
CM22	0.42	0.84	0.84	0.02	0.56	0.002	0.14	0.003	0.14	97.04
CM31	0.01	0.80	1.65	0.05	0.51	0.006	0.16	0.003	0.17	96.64

*L heat treatment: 900°C/1hr austenize, air cool, 664°C/4hr temper, air cool, 600°C/40hr stress relief, air cool. CM heat treatment: 900°C/30min austenize, salt quench to 450°C/hold for 10min, 660°C/4hr temper, air cool, 607°C/24hr stress relief, cool at 8°C/hr to 300°C, air cool.

1.2.2 Surveillance and Program Alloy Matrix

Nine surveillance materials were procured specifically for this experiment. In addition, eleven other archival surveillance alloys, which had been previously studied by UCSB in the Irradiation Variables Program (IVAR), were also included. While flux effects have been extensively studied for many years, they are still not fully understood. Thus, the surveillance alloys will allow for direct comparison of results from this high-flux test irradiation with those from the much lower flux surveillance irradiations. The compositions of the surveillance alloys are given in Table 1.2. Finally, a number of program plates and welds, seen in Table 1.3, that have been in a number of other irradiations were also included.

Table 1.2 Composition (wt.%) of surveillance alloys.

Alloy	Cu%	Ni%	Mn%	Cr%	Mo%	P%	C%	S%	Si%	Fe%
SB1*	0.20	0.60	1.33	0.11	0.49	0.005	0.22	0.016	0.23	96.82
SB2*	0.06	0.75	0.79	0.35	0.58	0.010	0.20	0.009	0.28	96.97
SB3*	0.05	0.56	1.32	0.08	0.59	0.010	0.24	0.016	0.24	96.89
SW1*	0.14	0.19	1.06	0.06	0.50	0.016	0.13	0.009	0.27	95.90
SW2*	0.36	0.78	1.42	0.04	0.49	0.013	0.18	0.011	0.18	96.54
SW3*	0.22	0.72	1.37	0.09	0.48	0.016	0.12	0.011	0.20	96.77
SW4*	0.03	0.90	0.94	0.03	0.23	0.004	0.14	0.014	0.32	97.39
SW5*	0.04	0.95	1.41	0.13	0.48	0.009	0.09	0.009	0.45	96.44
SW6*	0.29	0.60	1.44	0.14	0.36	0.014	0.10	0.011	0.50	96.55
QC1	0.24	0.54	1.70	0.06	0.43	0.014	0.09	0.016	0.56	96.35
QC2	0.24	0.56	1.68	0.07	0.40	0.014	0.09	0.016	0.55	96.38
D3	0.28	0.63	1.59	0.08	0.43	0.011	0.09	0.015	0.51	96.36
HB	0.22	0.07	1.37	0.16	0.46	0.014	0.13	0.016	0.29	97.27
MP	0.19	1.02	1.30	0.05	0.51	0.017	0.11	0.015	0.18	96.61
TW	0.15	0.08	1.61	0.15	0.49	0.019	0.12	0.014	0.28	97.09
WA	0.21	0.63	1.69	0.14	0.40	0.014	0.08	0.013	0.45	96.37
WB	0.28	0.69	1.63	0.10	0.40	0.018	0.09	0.009	0.54	96.52
WC	0.06	0.62	1.30	0.08	0.31	0.009	0.08	0.010	0.37	97.22
W62	0.23	0.60	1.61	0.12	0.39	0.016	0.08	0.007	0.59	96.59
W63	0.3	0.69	1.65	0.10	0.43	0.016	0.10	0.011	0.63	96.37
W65	0.22	0.60	1.45	0.09	0.39	0.015	0.08	0.015	0.48	96.88
W67	0.18	0.61	1.27	0.14	0.43	0.009	0.10	0.009	0.50	97.99

*Procured by ORNL and ATI Consulting and not identified by the plant specific vessel code since further verification of the results is needed

Table 1.3 Composition (wt.%) of program alloys.

Alloy	Cu%	Ni%	Mn%	Cr%	Mo%	P%	C%	S%	Si%	Fe%
EA	0.20	0.11	1.47	0.05	0.52	0.013	0.23	0.024	0.26	97.12
EC*	0.35	0.60	1.30	0.04	0.44	0.005	0.16	0.009	0.17	96.93
ED	0.40	0.60	1.36	0.04	0.44	0.006	0.12	0.013	0.51	96.51
FE	1.69	1.30	0.02	0.51	0.009	0.21	0.006	0.20	96.05	0.01
W73*	0.31	0.60	1.56	0.25	0.58	0.017	0.10	0.005	0.45	96.44
WM	0.27	0.57	1.61	0.10	0.41	0.017	0.08	0.007	0.62	96.59
HSST02	0.14	0.67	1.55	0.04	0.53	0.009	0.23	0.014	0.20	96.62
A302B	0.14	0.20	1.20	0.24	0.60	0.02	0.20	0.017	0.28	97.39
A508	0.03	0.8	0.74	0.36	0.59	0.015	0.20	0.005	0.026	97.47
JRQ*	0.14	0.82	1.40	0.12	0.50	0.019	0.18	0.004	0.25	98.61
PBW	0.2	1.20	1.30	0.04	0.54	0.010	0.11	0.017	0.18	99.64

*Alloys where data is reported here

1.3 Irradiation Conditions

The UCSB ATR-2 experiment reached a peak fluence of $\approx 1.4 \times 10^{20}$ n/cm², which is about 40% larger than what some RPVs will reach at an 80 year extended life. In addition, four capsules reached a peak fluence ranging from 5.1×10^{19} to 9.1×10^{19} n/cm². These capsules will be used to directly compare data from this experiment to the lower fluence data available in surveillance programs. The specimens were irradiated at four nominal temperatures: 250, 270, 290 and 310°C. The ≈ 109 cm long test train consisted of an assembly of concentric tubes, with an inner tube containing 13 thin-walled (0.125 mm) specimen cups. Temperatures were monitored by 28 thermocouples on the outside of an engineered gas gap tube. Finite element heat transfer models were used to design the gas gaps and calculate the predicted specimen temperatures. The gas gap provided active temperature control by adjusting a flowing He-Ar gas mixture based on temperature readings from the 28 thermocouples. Gas was provided to three separate compartments of the test train. One of the most remarkable features of the ATR-2 irradiation was that the entire test train was successfully removed and re-inserted to avoid a PALM cycle when the ATR lobe containing the test train (the I-22 position) ran at high power. Finally, a gadolinium shield was included in the test train to reduce the thermal neutron flux on the specimens, hence minimizing their activities. Overall the UCSB irradiation was a resounding success, primarily due to the extraordinary and creative contributions of the INL engineering team that designed and conducted the irradiation.

The average flux, fluence and irradiation temperature (target and as run) for each cup are given in Table 1.4. Except for the two bottom and two top cups, the as-run temperatures were very close to their target values. Details regarding determining the flux and temperature profiles in ATR-2 can be found in the INL as-run reports [7, 8].

Table 1.4 Neutron flux, fluence ($E > 1$ MeV) and temperature for the various cups in the ATR-2 irradiation.

Cup	Flux (10^{12} n/cm ² -s)	Fluence (10^{19} n/cm ²)	Target T _{irr} (°C)	Actual T _{irr} (°C)
1	1.34	5.11	290	247
2	1.94	7.43	290	268
3	2.54	10.35	290	280
4	3.13	11.90	270	268
5	3.36	12.80	250	255
6	3.58	13.70	290	285
7	3.64	13.90	290	291
8	3.60	13.70	290	293
9	3.47	13.20	290	293
10	3.21	12.30	310	319
11	2.89	11.05	290	292
12	2.17	9.08	290	264
13	1.52	5.79	290	238

1.4 Mechanical Property Testing

1.4.1 Hardness Testing

Vickers microhardness (μH) testing was carried out in the Low Activation Materials Development and Analysis Laboratory (LAMDA) at Oak Ridge National Laboratory. A Wilson microhardness tester was used to make 5 indents per specimen at a 10 kg load. Testing has been completed on 15 of the surveillance alloys from cup 7 along with their respective baselines. The mean and standard deviation microhardness were determined for the unirradiated baseline and irradiated condition. The difference, or ΔH_v (kg/mm^2), was determined by subtracting the baseline from the irradiated value. The standard deviation in ΔH_v was determined by a root sum square of the standard deviations of the baseline and irradiated microhardness measurements. Finally, the change in microhardness was converted to change in yield strength using an established relation $\Delta\sigma_y$ (MPa) = 3.33* ΔH_v (kg/mm^2), as further discussed in Section 3.1.2.

1.4.2 Tensile Testing

A total of 380 tensile specimens for 55 alloys were included in the experiment in 8 of the 13 cups. The current status of tensile testing is summarized in Table 1.5.

Table 1.5 Summary of tested and remaining specimens in tensile matrix. Note all conditions are at 290°C.

Cup	Fluence (10^{19} n/cm ²)	Tested Alloys	Tested Specimens	Remaining Specimens
3	10.35	0	0	139
6	13.70	0	0	19
7	13.90	43	92	47
8	13.70	8	8	9
9	13.20	0	0	18
11	11.05	0	0	17
12	9.08	0	0	17
13	5.79	0	0	17

SSJ-2 type tensile specimens, shown in Figure 1.3, are nominally 16 mm long with a gauge section width of 1.2 mm and thickness of 0.5 mm. It should be noted that approximately half of the specimens have a nominal gauge length of 5.0 mm, while the others have a 2.2 mm gauge length. No significant differences in the tensile properties have been observed between the two gauge lengths. Groups of ≈ 18 specimens were loaded in boxes designed to maximize heat transfer.

The dog-bone tensile specimens are clamped by grips in an alignment fixture prior to placement in on an MTS 810 load frame. The specimens were loaded at a rate of 0.008 mm/s at strain rates of 0.002 to 0.003/min. Standard engineering stress-strain curves are recorded based on precise measurements of the width and thickness of the gauge section of individual specimens. A best fit to the elastic loading region is used to establish the 0.2% offset yield stress ($\sigma_y \approx s_y$). The ultimate engineering stress (s_u) at maximum load is also recorded. The tensile tests on irradiated specimens are generally stopped at a load that is $\approx 70\%$ of the

maximum to keep the specimen intact. An example stress-strain curve, with a 0.2% offset line is shown in Figure 1.4.

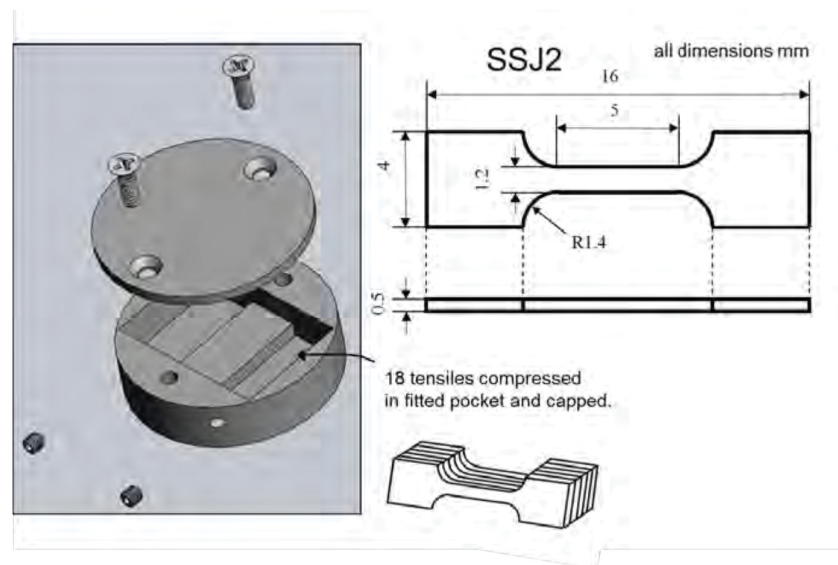


Figure 1.3 Schematic of the tensile loading box (left) and SSJ-2 tensile specimens (right). Note that half of the specimens have a gauge length of 5.00 mm (showed), while the others have a 2.2 mm gauge length.

The focus of tensile testing thus far has been on the two highest ϕt ($\approx 1.4 \times 10^{20}$ n/cm²) conditions at 290°C, cups 7 and 8 (note the RR alloys are not discussed here). One hundred of the 156 specimens in these conditions have been tested; those remaining are being held for future resistivity-Seebeck coefficient (RSC) measurements. Three or more unirradiated (control) specimens were tested to establish the baseline yield stress (σ_{yu}) and ultimate engineering tensile stress (s_{uu}), and used to determine the corresponding irradiation hardening ($\Delta\sigma_y$ and Δs_u).

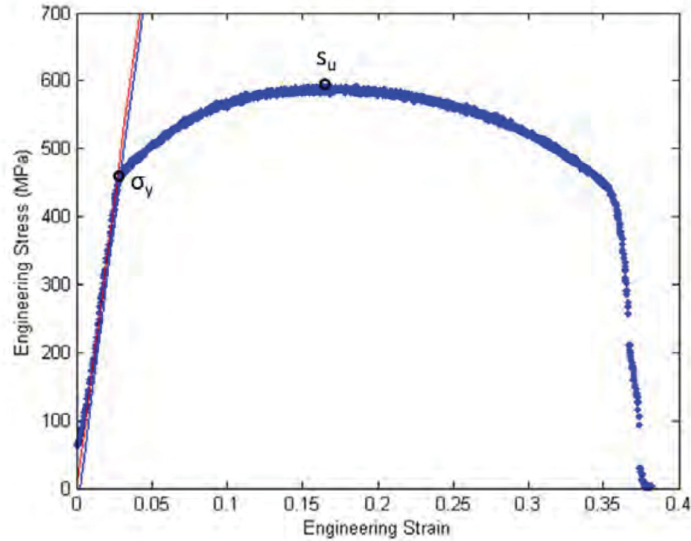


Figure 1.4 Example stress-strain curve with 0.2% offset line.

1.4.3 Shear Punch Testing

The majority of specimens (≈ 1000 out of 1625) in ATR-2 are 20 mm diameter x 0.5 mm thick discs DMCs. The DMCs were included for all the alloys because they permit a wide range of PIE studies on a single specimen based on a sequence of tests, such as shear punch tests, μ H and a host of microstructural characterization methods. The effects of irradiation on constitutive properties will be obtained from shear punch tests (SPT) on the DMCs with minimal specimen preparation. The load-displacement data from SPT can be used to derive true-stress, true-strain (σ - ϵ) data. However, here SPT is used to measure the shear yield stress (τ_y) and its relation to σ_y . A previously established relation, of $\sigma_y \approx 1.77\tau_y$, is close to the theoretical Von Mises value of $\sqrt{3}$ [9]. To facilitate DMC testing, we have developed an automated SPT apparatus that is briefly described in the next section. However, in this report, SPT were conducted using a simpler single specimen punch fixture. The SPTs were carried out on 10 unirradiated surveillance steels and four unirradiated RR alloys that span a wide range of σ_y . The test fixture is shown in Figure 1.5. These tests were carried out as part of qualification and calibration of the automated SPT apparatus.

The basic premise of a shear punch test is very similar to a tensile test. A specimen is clamped tightly in a fixture with a punch above it and a die below. The punch and die are precision machined and aligned to have optimal diametrical clearance. A measured load is applied to the top of the punch, while the backside displacement of the extruded disc blank being sheared is measured with a lever arm displacement meter. The displacement increases until the punched disc is injected into the die.

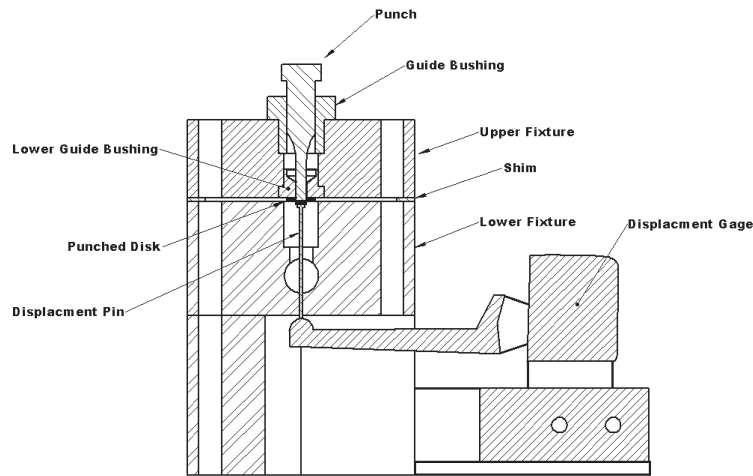


Figure 1.5 Schematic of the single specimen punch shear punch tester.

The shear stress is calculated based on punch load (P), the average of the punch and die diameter (D), and specimen thickness (t) as $\tau = P/(\pi Dt)$. The shear strain (e_s) is defined by dividing the measured backside displacement by the DMC thickness. Thus, the measured load and displacement can be converted to shear stress and strain. A typical shear punch curve is shown in Figure 1.6 [9].

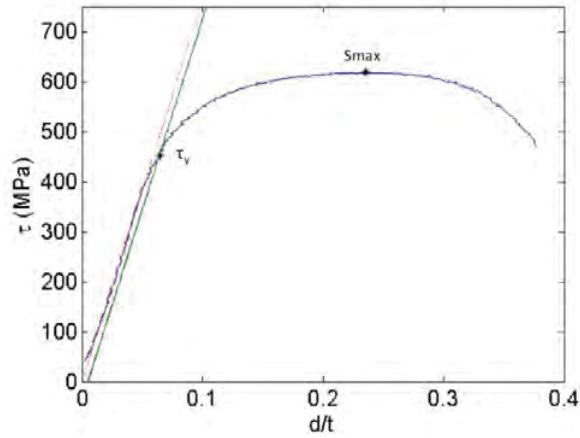


Figure 1.6 A typical shear punch curve [9].

As in a tensile test, the quasi-linear elastic region is fit and a 0.2% offset parallel line is used to index the shear yield stress (τ_y). For ideal shear dominated conditions, the theoretical relation between τ_y and the uniaxial yield stress (σ_y) is given by the von Mises yield criterion as $\sigma_y = \tau_y\sqrt{3}$. A best fit empirical correlation developed by UCSB on the Rolls Royce steels found $\sigma_y \approx 1.77\tau_y$, within $\approx 2.5\%$ of the theoretical relation [9]. A plot of σ_y versus τ_y for these steels with a wide range of yield stress is shown in Figure 1.7.

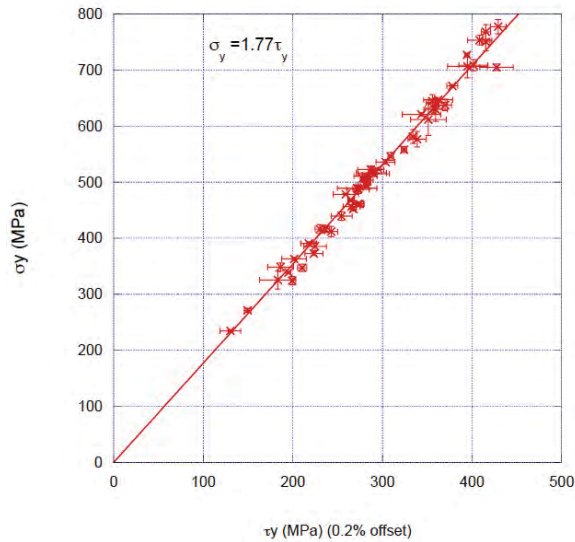


Figure 1.7 σ_y versus τ_y for steels with a wide range of yield strengths showing the empirical relation $\sigma_y \approx 1.77 \tau_y$ [9].

1.4.4 Automated Shear Punch Testing

The single punch used for the SPT results reported here requires a standard load frame to apply forces to the punch. Single punch tests are time consuming and potentially subject to variability due to factors such as clamping loads. Further, such tests result in higher radiation exposures to the test personnel from the activated steel samples due to the increased time and handling required for testing. To address these issues, we have developed an automated shear punch tester. The instrument consists of a pneumatically clamped upper assembly, with a hydraulic actuator and a load sensor. A precision punch is coupled to the load sensor through a hardened guide for accurate alignment. Both the guide and punch are interchangeable so different SPT diameters can be used. The lower assembly consists of an indexing loading table that supports and positions the DMC for testing. The loading table can be removed and exchanged to support varying diameter test coupons, though the focus to date has been on designing the instrument to test the 20 mm DMCs. The current design allows four 3.0 mm punch diameter SPTs per 20 mm coupon; however the SPT can easily be modified to obtain a larger number of tests per DMC.

A precision die is placed under the test specimen that is exactly matched to the punch for optimal clearance. A spring-loaded follower contacts the bottom face of the test specimens and tracks the bottom-face deflection throughout the punching process. The load cell and deflection sensor provide the load-displacement data necessary to compute shear stress and strain. The SPT tool is computer-controlled (clamping, load actuation, blank ejection, and digital data acquisition).

The main benefit of the automated instrument, shown in Figure 1.8, is a much higher testing throughput relative to the single punch fixture. Another advantage is that the automated SPT instrument is self-contained, occupying a relatively small footprint, and does

not require a load frame, facilitating installation in the LAMDA facility. Further, automated SPT will involve reduced personal radiation exposures. The automated SPT system is still undergoing full qualification and calibration on a large matrix of unirradiated alloys, hence, was not used to generate irradiated data at this time.

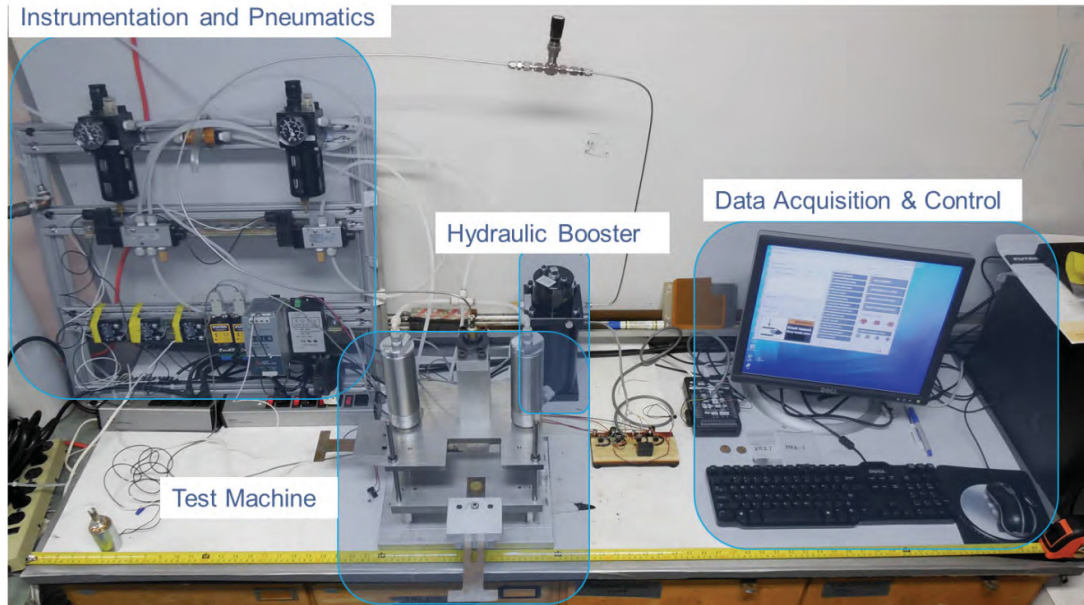


Figure 1.8 Automated shear punch instrument showing footprint on a lab bench.

1.5 Microstructural Characterization

The nano-scale precipitates that form under irradiation in RPV steels are characterized by radii from $\approx 1\text{-}3$ nm and number densities from $\approx 10^{23}\text{-}10^{24}$ m^{-3} . The precipitate sizes and character make imaging them by standard TEM techniques very difficult. Thus, the primary methods used here to characterize these precipitates are atom probe tomography (APT) and small angle neutron scattering (SANS). All techniques have their own inherent strengths and weaknesses, but can be highly complementary in combination. For example, both APT and SANS measure precipitate size distributions, average size ($\langle r \rangle$), number density (N) and volume fraction (f_p), while APT can also measure the precipitate compositions and morphologies. SANS samples precipitates in large volumes of material, while APT typically

samples volumes that are ≈ 13 orders of magnitude smaller. SANS requires beam time at user nuclear reactor facilities, with limited access. APT requires hot Focused Ion Beam (FIB) micro-machining that is possible only at a very limited number of facilities. Here, both techniques have been used on a small subset of alloys to date. A brief description of these techniques follows.

1.5.1 Atom Probe Tomography

Atom probe tomography (APT) is a destructive microscopy technique that measures compositional distributions on the nano-scale, including precipitates and solute segregation. An APT specimen is fabricated, by electropolishing or FIB milling (FIBing), a needle typically ≈ 100 nm in diameter with a smoothly rounded tip. The needle is then mounted on a stage in an atom probe, in this case a Local Electrode Atom Probe (LEAP), in ultrahigh vacuum ($< 10^{-10}$ torr) and cooled to cryogenic temperatures (20-60K). In LEAPs, a high voltage electrode is located close to the needle tip to create a very high local electric field at the needle tip. A standing voltage is applied that is just below that needed to electrostatically evaporate the atoms from the tip surface, where the field is highly concentrated. High frequency voltage pulses (100-200 kHz) are then used to increase the field to the point that there is a significant probability that a tip atom will be ionized and evaporated, typically at a steady rate of 0.2-0.5% per pulse, that can be controlled by modifying the standing voltage. The tip is sequentially evaporated along the needle axis until a sufficient number of ions are collected or the tip breaks, which is often the case.

The evaporated ions are accelerated by the electric field and pass through an aperture in the local electrode prior to being individually counted by a position sensitive detector. The position of the ion on the detector is determined by the x-y timing of a voltage pulse in the cross

wire detector after charge amplification by a microchannel plate. A schematic of a LEAP is tip-electrode configuration is shown in Figure 1.9.

The time-of-flight between the voltage pulse causing evaporation and detection is used to determine the field emitted ion's mass-to-charge ratio, which is specific, with some overlaps, to a particular element and isotope. The detector position is used to determine the ion's location on the tip surface based on application of simple electrostatic field optics to a perfectly rounded needle tip. If ions evaporate prior to or slightly after the peak of the voltage pulse, then they acquire slightly less energy than those that evaporate at the peak voltage. Thus, there is a spread in the time-of-flight and corresponding mass-to-charge ratio spectrum. The LEAPs used for this report are equipped with so-called reflectrons, which alter the flight paths of ions with varying energies, and significantly reduce spread in the time-of-flight, thus improving mass resolution. The drawback to the high mass resolution instruments is that some ions are lost in the reflectron, reducing the collection efficiency from $\approx 65\%$ to 37% .

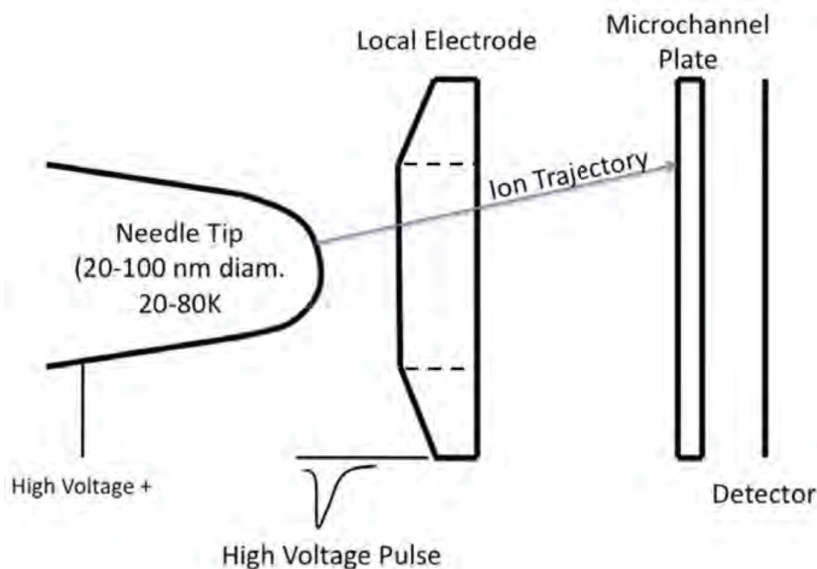


Figure 1.9 Schematic of a Local Electrode Atom Probe. Note that it is not to scale [10].

Three-dimensional (3D) reconstruction of the atomic positions is carried out with a proprietary software package, here the Cameca Integrated Visualization and Analysis

Software (IVAS) by assuming there is a uniform layer-by-layer removal of atoms from the tip. After each ion is evaporated, the associated volume is divided by the area of the evaporating surface within the field of view of the detector, incrementally changing the needle length in the z-direction, hence the position of the reconstructed tip surface. The next ion that evaporates is assumed to come from the repositioned surface. By continuously repeating this process a full 3D map of the element specific map of the atomic positions can be created. Note field emission of multi-atom/element ions is common, as is multiple ion charge to mass ratios for a particular isotope.

The resulting 3-dimensional datasets are then used to measure spatial distribution of the solutes, in this case the precipitates formed under irradiation. Precipitates are characterized by IVAS cluster analysis algorithms. The basic premise is that the atomic density of solute atoms is higher in precipitates than in the matrix. First, the distance (d) between specific solutes, here Cu, Ni, Mn and Si, and their Nth nearest solute neighbor is found, where the Nth atom is defined as the order (K). If d is less than a cutoff distance defined by the user (d_{\max}), the solute is considered to be a core atom. After all core has been defined, all atoms within d_{\max} , even those that are not solutes, are considered to be in the cluster. Clusters that have fewer than N_{\min} atoms are excluded from the analysis. In addition to characterizing the precipitate size distribution, $\langle r \rangle$, N and f_p , APT also measures the local bulk, matrix and precipitate compositions. Note the typical maximum volume of a sampled tip is less than $600,000 \text{ nm}^3$, equivalent to ≈ 50 million atoms. Nanoscale precipitation is governed by the local tip composition, which is seldom completely uniform from tip to tip. However, fluctuations in local compositions can be exploited to establish the relation between the alloy composition and the characteristics of the precipitates. For example, in this work the f_p closely tracks the local alloy Cu, Ni, Mn and Si contents. However, APT may not

be practically applicable to highly heterogeneous materials, or when number of feature of interest is low in the sampled tip volume. Of course many tips can be examined, but beyond a point this becomes impractical, especially in the cases of activated materials.

While APT is arguably the best tool for measuring the detailed nature of the precipitates that form under irradiation, the data must be cautiously interpreted in the face of a number of measurement artifacts. The most significant artifact is so-called trajectory aberrations. Trajectory aberrations are due to flattened or dimpled regions that form around a precipitate, deviating from an ideally rounded tip. In the case of RPV steels the deviation in local curvature causes surrounding matrix atoms to be focused onto the detector in the precipitate region. The flattened or dimpled region is caused by the lower potential needed to evaporate the precipitate solutes compared to the surrounding Fe matrix. Non-physically high precipitate atomic densities, which can be as high as 3 to 4 times that of the surrounding bcc matrix, signal trajectory aberrations. The reconstruction algorithm does not have any information on the incoming ion trajectory, only the location they hit the detector. As a result both focused matrix and actual precipitate solutes are reconstructed as if they originated from the same tip region. Although significant progress has been made in understanding trajectory aberrations, and other APT artifacts, this knowledge has not been converted to a standard practice and improving the fidelity of APT reconstructions is still work in progress. In this report, all Fe that is nominally reconstructed in a precipitate is treated as an artifact and excluded from compositional and size measurements.

APT needle preparation was performed at the Center for Advanced Energy Studies (CAES) Microscopy and Characterization Suite (MaCS) using their Focused Ion Beam dedicated to working with activated specimens. After liftouts were created, they were welded to posts on a 22 grid coupon and partially sharpened to minimize the activated material on the

coupon. The coupons were then shipped to UCSB where the final tip shaping was completed. A Cameca LEAP 3000X HR was used to run all samples using voltage mode with a 20% pulse fraction, a detection rate of 0.4 to 0.8%/pulse and a specimen temperature < 50K.

1.5.2 Small Angle Neutron Scattering

Small Angle Neutron Scattering (SANS) is based on coherent scattering of cold neutrons by atomic nuclei around the $\theta = 0$, Bragg peak. In the case of solute rich precipitates embedded in a solvent rich matrix, the coherent scattering cross section, $d\Sigma/d\Omega$, is a function of θ , or more precisely the scattering vector, $q = 4\pi\sin\theta/\lambda$, where λ is the neutron (or x-ray) wavelength. As shown in Figure 1.10, 2θ is the angle between the incident beam and detector x-y position. The magnitude $d\Sigma/d\Omega(q)$ depends on the square of the coherent scattering length density difference between the matrix and precipitate. The coherent nuclear scattering length (b) is a property of a specific nuclear isotope. The coherent magnetic b is a function of the atomic magnetization of in the precipitate or matrix phase. Scattering length density (SLD), ρ , is the product of the atomic density and the scattering length, usually taken as the averages for the matrix and precipitate, respectively. The amplitude of $d\Sigma/d\Omega(q)$ is a function of $\Delta\rho^2$ between the matrix and precipitate, and the corresponding q dependence is a function of the size, or size distribution, of the precipitates. The $d\Sigma/d\Omega(q)$ generally scales with $(1/qr)^2$, hence, smaller precipitates produce scattering at higher q . This makes it relatively easy to characterize nm-scale precipitates formed during irradiation in a matrix phase that is would otherwise be free of features in this size range in the unirradiated condition. The precipitate scattering is reflected in the difference between irradiated (with nano precipitates) versus unirradiated (without nano precipitates) steels. If $\Delta\rho^2$ is known, SANS can be used to determine the precipitate size distribution, $\langle r_p \rangle$, N_p and f_p .

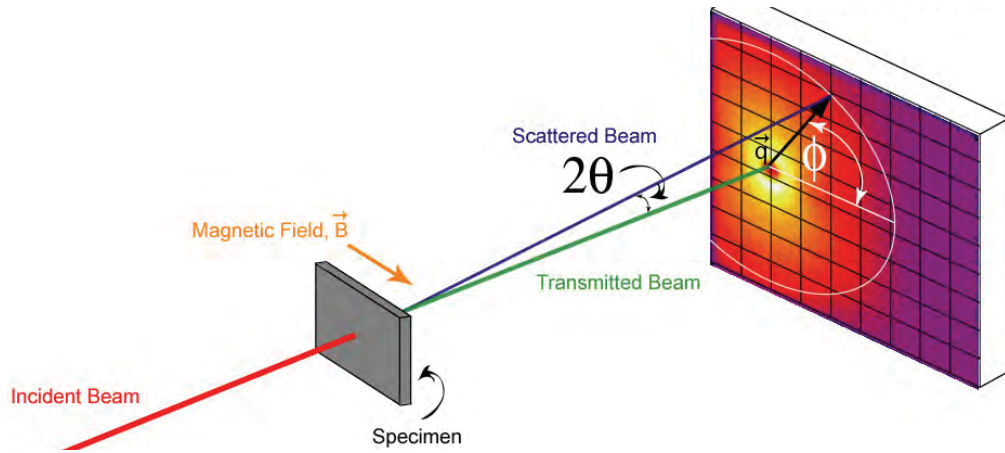


Figure 1.10 SANS experimental setup.

SANS (and SAXS) measures the number of scattered neutron counts, I , at a detector position at q and ϕ where ϕ is the azimuthal angle around the beam, $I(q,\phi)$, for a specified total beam fluence on the specimen. The total $I(q,\phi)$ for the steel is isolated by appropriate adjustments for background and beam attenuation. The corresponding precipitate $I_p(q,\phi)$ is found by subtracting an unirradiated (nano precipitate free) control. The $I_p(q,\phi)$ is then converted to a $d\Sigma/d\Omega(q,\phi)_p$, using a known isotropic scattering standard, in this case water.

Precipitates in ferromagnetic Fe produce both nuclear (N) and magnetic (M) small angle scattering, depending on their respective SLD. The nuclear SLD depends on the precipitate and matrix compositions that are not known a priori, so $\Delta\rho_n^2$ is also unknown. However, the Cu, Mn, Ni, Si solute rich precipitates are believed to be non-magnetic, or only weakly magnetic. Thus when the Fe matrix is magnetically fully saturated with a known magnetic SLD, $\Delta\rho_m^2$, the $d\Sigma/d\Omega(q)_m$ is known. The magnitude of the magnetic scattering varies with $\sin(\phi)^2$, ranging from 0 parallel to 1 perpendicular to the magnetic field, respectively. In practice, a fitted magnetic to nuclear scattering ratio (M/N) is used to convert the data at all ϕ to a magnetic scattering cross section, that is then fit to extract the precipitate size distribution $\langle r_p \rangle$, N_p and f_p .

SANS measurements were carried out on the NG7 beam line at the National Institute of Standards and Technology Center for Neutron Research. Small (dimensions) coupons were mounted in an automated sample changer in a 1.5 T horizontal magnetic field. The average neutron wavelength was 5 Å. A 2D ^3He detector measured the scattering intensity, I , as a function of q and ϕ . The $I(q, \phi)$ are measured for both unirradiated controls, that do not contain nano precipitates, and the irradiated steels. The $I(q, \phi)$ are corrected and normalized to one another by background subtraction and transmission measurements, as well as adjustments for different sample volumes probed by the neutron beam; the differences are generally minimal. Variations in detector pixel efficiencies are accounted for in converting $I_p(q, \phi)$ to an absolute $d\Sigma/d\Omega(q)_{n/m}$ differential scattering cross-sections using an isotropic scattering water standard. After conversion of the entire set of detector cross sections to an equivalent $d\Sigma/d\Omega(q)_m$, the data are least square fit using the assumed $\Delta\rho_m^2$ and a spherical q -dependent form factor and log normal size distribution. The fitting parameters are the precipitate size-distribution mode radius (r_m) and width parameter (β) and $d\Sigma/d\Omega(0)_m$. The fitted parameters are then used to calculate the precipitate $\langle r \rangle$, N_p and f_p . Multiple scattering features can be fit simultaneously. Multiple feature fits are also used to remove scattering artifacts due to experimental uncertainties and bias. Finally we note that scattering at very high q is due to an essentially isotropic incoherent background from various sources, but discussion is beyond the scope of this report. The irradiated and unirradiated $d\Sigma/d\Omega(q)$ are approximately the same at high q which is a useful check on the data. The major difference is due to the removal of solutes from the matrix by precipitation that can be readily accounted for if necessary. Further details regarding SANS theory, experimental details and data analysis can be found elsewhere [10–14].

The major assumption in the SANS analysis is that the precipitates are non-magnetic. This assumption has been shown to be valid for Cu rich precipitates that are dominant at lower fluence. However, this assumption may not be valid at high fluences where Mn, Si and most importantly, Ni, are the dominant solutes in the precipitates. Specifically, if the precipitates are partially magnetic, then the magnetic scattering contrast, $\Delta\rho_m^2$, assumed in the analysis is too large, resulting in an underestimate of the precipitate f_p and N_p . Work is ongoing to address this issue, including magnetic property measurements of the bulk precipitate phases, as well as SANS measurements at various temperatures. Further, Small Angle x-ray Scattering (SAXS) will be used to better evaluate the magnetization of the precipitates. The results of this research will be presented in future reports.

1.5.3 Small Angle x-ray Scattering (SAXS)

This section describes a collaboration between UCSB and Dr. Lynne Ecker and Dr. David Sprouster at the Brookhaven National Laboratory (BNL), and their input is reflected in what follows. SAXS is generally similar to SANS but with several major differences: a) SAXS is due to scattering length density (SLD) differences between the feature and the matrix that scale with the square of their respective electron densities; b) SAXS measurements can be made on very small material volumes; and, c) the count times for a SAXS measurements are on the order of seconds to minutes, rather than hours for SANS. Hence SAXS has a tremendous potential for characterizing irradiated materials, like the ATR-2 alloys.

SAXS was performed at the BNL National Synchrotron Light Source-II (NSLS-II) using the high-energy x-rays at the Powder Diffraction beamline (XPD). A total of 50 paired unirradiated control and irradiated ATR-2 alloys have been characterized to date. Figure 1.11 shows the hutch region of the XPD beamline that is specially configured to deal with

radioactive materials; notably the beamline station includes a sample changing and positioning robot.

The experiment was initially optimized for resolving the small (2-5 nm diameter) irradiation-induced precipitates. The 52.01 keV x-rays provided an accessible q-range of $0.17\text{-}7.5\text{ nm}^{-1}$. However, SAXS on previous irradiated RPV samples (IVAR, BR2 and ATR1) indicated that in some cases there are subtle changes in a population of larger diameter scattering features, that were identified as carbides (Fe_3C and Mo_2C), consistent with companion x-ray diffraction (XRD) measurements. Thus the SAXS experimental set up was modified to improve characterization of these larger carbides, in part so as to better isolate the signal from the nano-precipitates. In order to increase the q-range at the low end, a smaller beamstop was fabricated, the sample to detector distance was increased, and the incident x-ray energy was reduced to 42.6 keV. This combination of adjustments resulted in an expanded q-range of $0.065\text{-}6\text{ nm}^{-1}$, with a corresponding detectable particle diameter from $\approx 1\text{-}100\text{ nm}$. Data collected in the lower q-range not only allows improved fitting of the carbides and nanoscale precipitates, but also could be used in the future to quantify the effects of irradiation on these coarser scattering feature populations.



Figure 1.11 XPD beamline end station C.

Multiple scattering patterns were collected to improve the statistics and achieve a better powder average of the whole sample (while carefully avoiding saturation of the detector). Typical count times were 0.5-1 sec/sample (depending on the sample). Each diffraction or scattering pattern consisted of the average of 100-500 individual exposures. All raw two-dimensional patterns were background corrected by subtracting the dark current image and Kapton/air scattering. Noticeable artifact regions of the detector, such as the beam stop and dead pixels, were masked. The corrected and masked two-dimensional detector images were then averaged and radially integrated to obtain the one-dimensional SAXS patterns.

Similar to SANS, analysis of SAXS data requires knowledge of the composition and atomic density of the scattering feature. In practice this requires complementary APT and SANS measurements, and where possible, XRD based identification of the precipitate phase and crystal structure. In the interim, the nano precipitate size distribution, $\langle r_p \rangle$, N_p and f_p were evaluated based on assuming the scattering features were either Cu or Mn-Ni-Si G-phase. Thus these results must be considered preliminary and tentative.

2. Results

2.1 Surveillance Steels

2.1.1 Mechanical Properties

We plan to obtain SST, SPT and μ H data all alloys and irradiation conditions in ATR-2. This will not only provide cross-checks on the results of individual techniques, but an imperative, as only a limited number of alloys were included as tensile specimens. A subset of alloys from cup 7 has been tested to date. The tensile matrix includes a large number of surveillance steels, the UCSB SMS CM and L-series, and other previously irradiated program alloys. The results for the surveillance and program alloys are presented below. Property-property correlations are discussed in Section 3.1.

Two tensile specimens for the surveillance and program alloys were tested, along with three or more baseline specimens. Example stress-strain curves for the baseline and irradiated condition is shown in Figure 2.1 for the surveillance alloy SW6, which contains 0.29%Cu, 0.6%Ni, 1.44%Mn and 0.50%Si.

SW6: 0.29%Cu, 0.6%Ni, 1.44%Mn, 0.50%Si

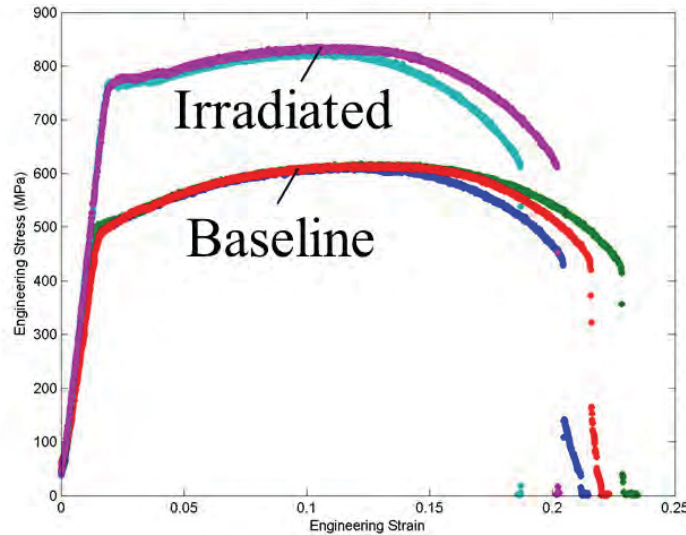


Figure 2.1 Stress-strain curves for the surveillance weld SW6 from the baseline and cup 7 irradiated conditions.

The redundant tests are generally in good agreement. Tensile curves for the other the alloys are given in Appendices A.1 and A.2 for the surveillance and program alloys, respectively. The measured σ_{ywi} , $\Delta\sigma_y$ and the corresponding nominal standard deviations (SD) are given in Table 2.1. We recognize that the number of tests was far too small for SD meaningful in a standard statistical sense, but they rather simply reflect the spread in the data. In general the surveillance alloys have fairly small variation in the measured $\Delta\sigma_y$ with an average SD of 16 MPa, which is $\approx 7\%$ of the average yield stress increase.

Table 2.1 Summary of the tested surveillance and program alloys in the baseline and cup 7 irradiated conditions.

Alloy	Baseline Samples			Cup 7 Irradiated Samples				
	Specimens	σ_y (MPa)	\pm (MPa)	Specimens	σ_y (MPa)	\pm (MPa)	$\Delta\sigma_y$ (MPa)	\pm (MPa)
SB1	3	447	5	2	691	6	244	7
SB2	4	404	17	2	582	5	178	17
SB3	4	469	16	2	620	6	151	18
SW1	4	476	11	2	641	16	165	19
SW3	4	443	19	2	734	1	291	19
SW4	3	471	4	2	616	19	144	19
SW5	3	472	8	2	678	8	206	12
SW6	3	493	11	2	764	3	271	11
QC1	3	461	8	2	721	18	260	20
QC2	4	447	18	2	730	8	283	19
D3	3	456	11	2	755	9	299	14
HB	3	443	19	2	613	8	169	21
MP	3	441	5	2	655	16	214	16
WA	6	516	23	2	757	8	241	25
WB	3	474	4	2	737	3	263	5
WC	5	479	21	2	654	6	175	22
W62	4	476	20	2	754	9	278	22
W63	3	479	8	2	738	4	259	9
W65	3	433	18	2	666	7	233	19
W67	3	528	10	2	671	7	143	13
EC*	4	508	8	2	740	8	232	12
JRQ*	3	450	8	2	673	1	222	8
W73*	3	489	13	2	728	16	239	20

*Program Alloy

Microhardness testing has been completed at ORNL on 11 surveillance alloys and 4 of the program steels at a 10 kg load. The results are given in Table 2.2 and Table 2.3 for the surveillance and program alloys, respectively. In addition to the measured ΔH_v , the estimated $\Delta\sigma_y$ using the relation $\Delta\sigma_y$ (MPa) = 3.33 ΔH_v (kg/mm²) is also shown.

Table 2.2 Microhardness data taken at ORNL for 11 surveillance alloys in the baseline and cup 7 irradiated conditions.

Alloy	Baseline Samples		Cup 7 Irradiated Samples					
	H _v (kg/mm ²)	± (kg/mm ²)	H _v (kg/mm ²)	± (kg/mm ²)	ΔH _v (kg/mm ²)	± (kg/mm ²)	Δσ _y (MPa) (3.33*ΔH _v)	± (MPa)
SB1	212	3	278	5	66	6	220	20
SB2	198	5	254	3	56	6	186	20
SB3	209	4	253	8	43	9	143	30
SW1	204	2	251	5	47	5	157	17
SW2	192	4	301	4	109	6	363	20
SW3	198	3	302	4	104	5	346	17
SW4	192	3	256	3	64	4	213	13
SW5	198	2	264	3	66	4	220	13
SW6	209	4	298	1	89	4	296	13
QC1	203	4	276	2	73	5	243	17
D3	202	3	279	3	77	4	256	13

Table 2.3 Microhardness data taken at ORNL for 4 program alloys in the baseline and cup 7 irradiated conditions.

Alloy	Baseline Samples		Cup 7 Irradiated Samples					
	H _v (kg/mm ²)	± (kg/mm ²)	H _v (kg/mm ²)	± (kg/mm ²)	ΔH _v (kg/mm ²)	± (kg/mm ²)	Δσ _y (MPa) (3.33*ΔH _v)	± (MPa)
EA	203	2	263	5	59	5	196	18
EC	210	2	272	2	62	3	206	9
ED	200	3	273	2	73	4	243	12
FE	247	2	299	2	51	3	170	9

Manual shear punch testing was carried out on a subset of baseline surveillance alloys in order to directly tie to a large previously established database using the same test fixture. Examples of baseline shear stress-shear strain curves for alloy SW6 are shown in Figure 2.2. The other baseline curves are shown in Appendix A.3 and the results are given in Table 2.4.

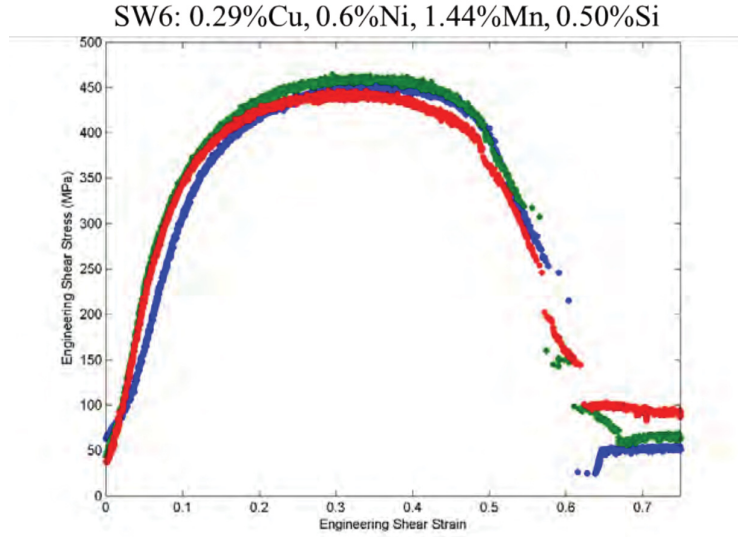


Figure 2.2 Baseline SPT curves for the surveillance alloy SW6.

Table 2.4 Shear yield (τ_y) and ultimate stress (s_{max}) for the baseline surveillance alloys.

Alloy	Tests	τ_y (MPa)	\pm (MPa)	s_{max} (MPa)	\pm (MPa)
SB1	3	268	10	454	9
SB2	4	290	14	435	10
SB3	4	294	28	459	6
SW1	3	265	9	439	0
SW3	3	263	8	435	6
SW4	3	251	31	424	1
SW5	3	253	3	435	6
SW6	3	265	19	455	12
QC1	4	244	16	436	4
D3	3	262	9	443	6

2.1.2 Small Angle Neutron Scattering

Small Angle Neutron Scattering (SANS) was carried out at the National Institute of Standards and Technology (NIST) Center for Neutron Research using the NG7 beamline. The focus was on the surveillance alloys from Cup 7 where either tensile and/or microhardness data was also available. An example of baseline and irradiated scattering cross section curves for SW2, containing 0.36%Cu and 0.78%Ni, is shown in Figure 2.3 The curves are for $\phi = 45^\circ$, which represents the nuclear plus 50% of the magnetic scattering.

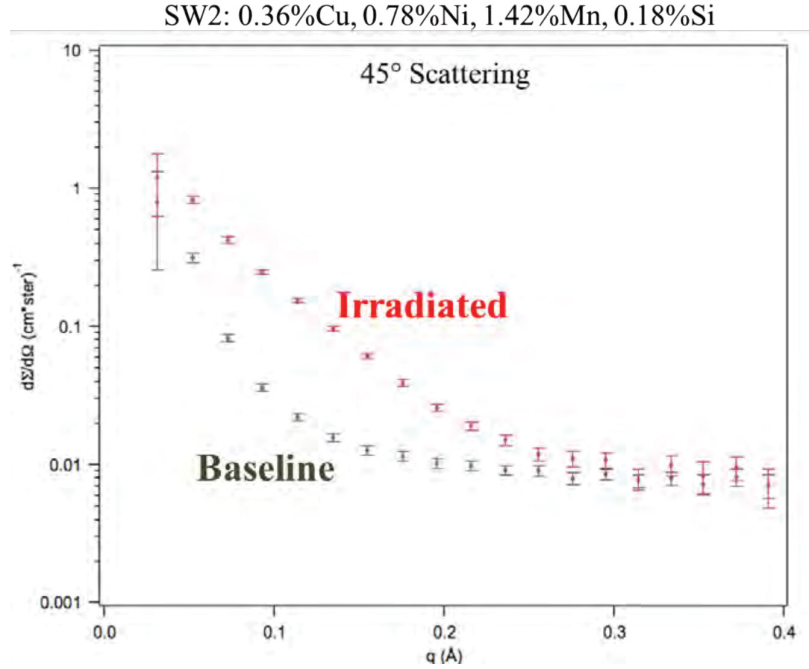


Figure 2.3 Absolute scattering curves taken at a 45° angle with respect to the magnetic field for the surveillance weld SW2 showing the extra scattering in the cup 7 irradiated condition due to formation of precipitates.

The large bulge in scattering cross section in the irradiated curve (red) between $q \approx 0.5$ and 2.5 nm^{-1} is due to precipitates which formed under irradiation. Analysis yielded $\langle r_p \rangle = 1.62 \text{ nm}$, $N_p = 3.7 \times 10^{23} \text{ m}^{-3}$ and $f_p = 0.65\%$. The corresponding scattering curves for 8 other alloys are shown in Appendix A.4 and the SANS results are given in Table 2.5.

Table 2.5 SANS results for the surveillance alloys from cup 7 showing the average precipitate radius ($\langle r \rangle$), number density (N_p), volume fraction (f_p) and magnetic-to-nuclear scattering ratio (M/N).

Alloy	$\langle r \rangle$ (nm)	N_p (10^{23} m^{-3})	f_p (%)	M/N
SB1	1.44	3.1	0.38	2.1
SB2	1.32	1.5	0.14	14.8
SW1	1.46	1.8	0.23	1.6
SW2	1.62	3.7	0.65	2.2
SW3	1.74	3	0.65	2.6
SW4	1.31	2.1	0.20	2.1
SW5	1.32	2.1	0.21	2.7
QC1	1.53	2.8	0.42	2.2
D3	1.49	3.5	0.49	2.6

2.2 UCSB Split Melt Steels and Program Alloys

2.2.1 Mechanical Properties

Tensile testing has been completed on the matrix of 22 UCSB split-melt steels (SMS) from Cup 7. The L and CM series SMS matrix has systematic variation in Cu, Ni, Mn and P contents. Examples of the baseline and irradiated stress-strain curves for two alloys, a 0.01% Cu, 0.74% Ni alloy (LG) and a 0.41% Cu, 0.86% Ni alloy (LC), are shown in Figure 2.4. While the baseline σ_y for both steels are approximately the same, the alloy containing higher Cu (LC), experiences significantly more irradiation hardening. The corresponding tensile data for all of the SMS alloys is given in Table 2.1 and the comparisons of irradiated and baseline tensile curves for all UCSB SMS are shown in Appendix A.5. A preliminary analysis of this data is discussed in Section 3.5.

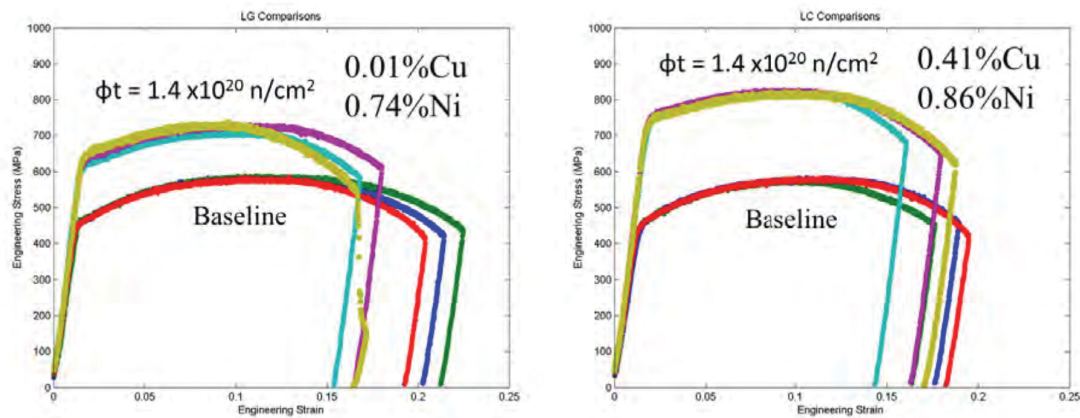


Figure 2.4 Stress-strain curves for two alloys, LG and LC, from the cup 7 (red) and baseline (blue) conditions.

Table 2.6 Yield strengths for baseline and cup7 irradiated UCSB SMS.

Alloy	Baseline Samples			Cup 7 Irradiated Samples				
	Specimens	σ_y (MPa)	\pm (MPa)	Specimens	σ_y (MPa)	\pm (MPa)	$\Delta\sigma_y$ (MPa)	\pm (MPa)
LB	3	447	5	2	619	1	172	5
LC	3	446	2	3	737	4	291	4
LD	5	445	3	3	799	7	355	7
LG	3	457	5	3	622	21	165	21
LH	4	458	9	2	647	1	190	9
LI	4	454	8	2	673	0	219	8
LJ	3	504	7	2	741	10	237	12
CM3*	4	363	68	2	486	122	123	45
CM5	2	363	17	2	615	2	252	17
CM6	3	407	7	4	653	12	246	14
CM7*	3	445	39	2	741	49	300	45
CM9	4	398	7	2	567	3	169	7
CM11	3	405	19	2	721	40	316	45
CM16	3	440	5	2	695	35	255	36
CM17	3	432	14	2	867	5	434	15
CM19	3	434	25	2	731	16	297	29
CM20	3	434	1	2	898	18	463	18
CM22	3	405	28	2	681	15	275	32
CM31	4	439	9	2	598	18	159	20

*Two populations of samples, strong or weak, were found for these alloys. The $\Delta\sigma_y$ for was very similar when using the weak irradiated and baseline or strong irradiated or baseline.

2.2.2 Atom Probe Tomography

Atom probe tomography (APT) was carried out on six of the UCSB from cup 7. Specimens were partially fabricated in the CAES MaCS lab and FIBed to their final shape and run in the 3000X HR LEAP at UCSB. Examples of atom maps for LG and LC (the same alloys that are in Figure 2.4) are shown in Figure 2.5. These APT results show that large f_p of Cu-rich precipitates and/or MNSP LBP can form at high fluences even in Cu-free, medium Ni steels. In the Cu-bearing alloy, as illustrated by LC in Figure 2.6, the precipitates have a highly Cu-enriched region (the green surface), which forms first, with a Mn-Ni-Si enriched appendage (the pink surface). The separation of the Cu and Mn-Ni-Si rich regions is also shown in the composition profile through the highlighted precipitate. Such co-precipitation has been seen many times in both test reactor [15] and surveillance irradiated steels [16, 17],

and confirms the hypothesis that the Cu precipitates act as nucleation sites for a separate MNSP phase [15]. The APT results on the six alloys are given in Table 2.7.

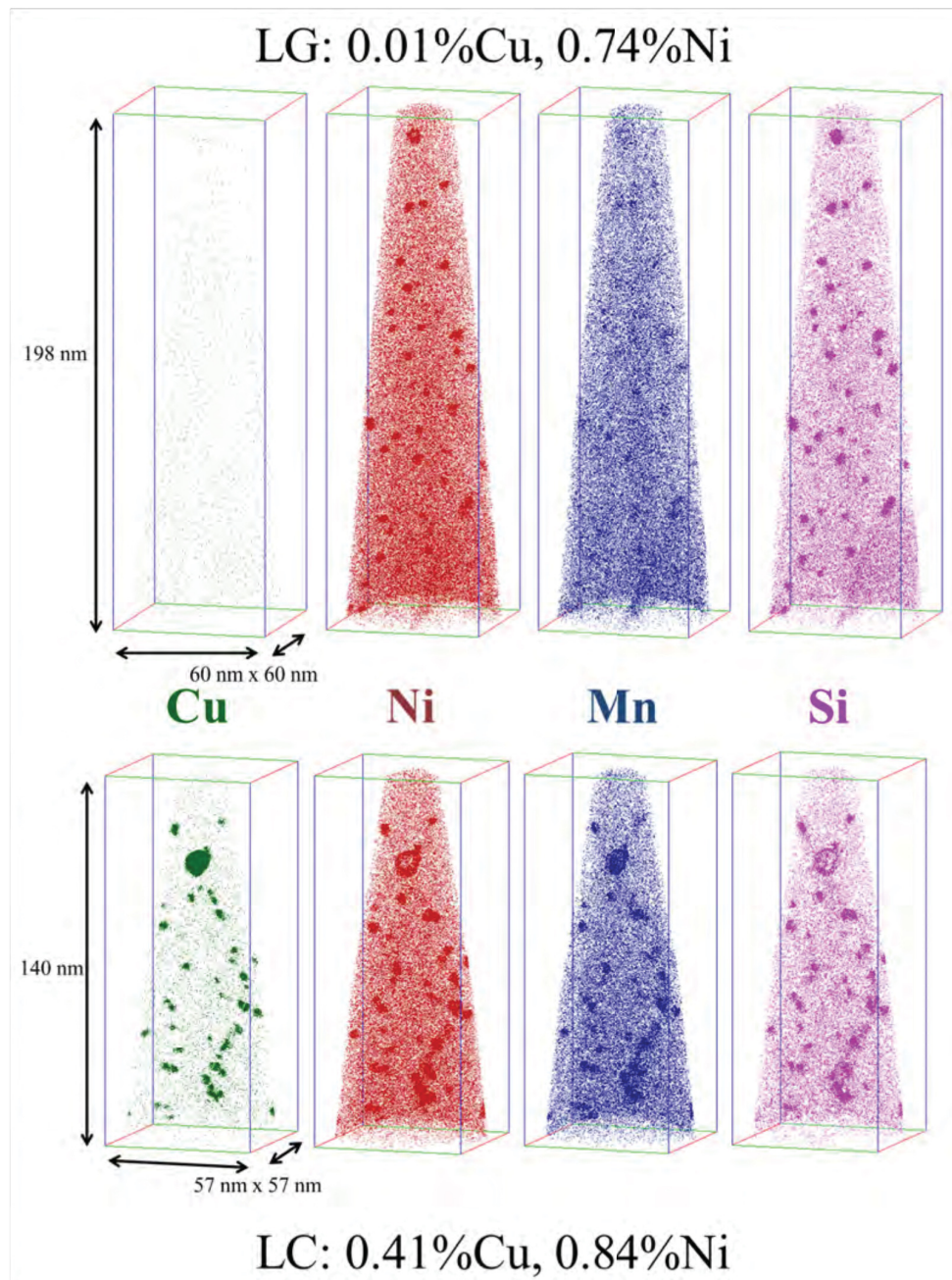


Figure 2.5 Cup 7 APT atom maps from a low Cu, medium Ni steel (LG) and a high Cu, medium Ni steel (LC), showing large volume fractions of (Cu)-Mn-Ni-Si precipitates.

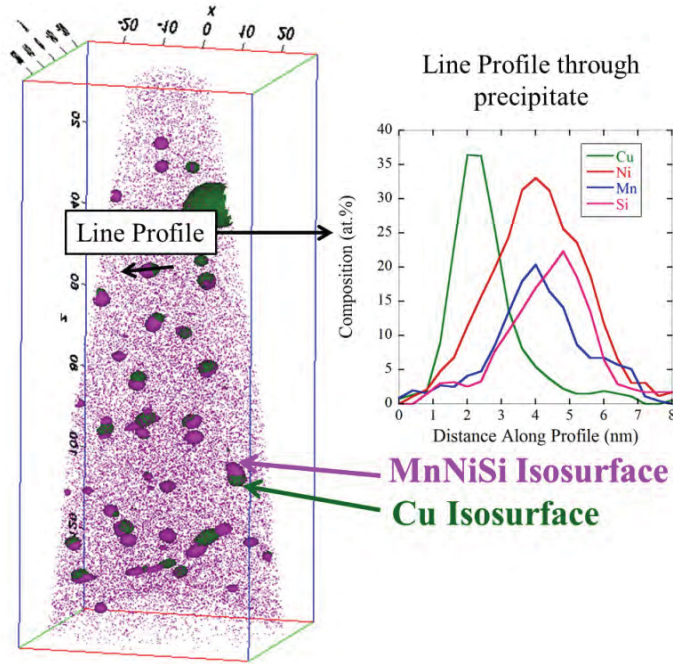


Figure 2.6 Atom map from the 0.41%Cu, 0.84%Ni alloy with Cu (green) and Mn-Ni-Si (Pink) isosurfaces (left) and a 1-dimensional concentration profile through a precipitate showing separate Cu and Mn-Ni-Si rich regions (right).

Table 2.7 Atom Probe Tomography data for the UCSB SMS from Cup 7.

Alloy	Composition (at.%)												Precipitate Values		
	Bulk				Matrix				Precipitate				<d> (nm)	N_p (m^{-3})	f_p (%)
	Cu	Ni	Mn	Si	Cu	Ni	Mn	Si	Cu	Ni	Mn	Si			
LC	0.23	0.86	0.93	0.46	0.05	0.61	0.76	0.32	24.3	36.5	22.1	17.1	3.30	4.68E+23	0.71
LD	0.20	1.18	0.95	0.51	0.05	0.82	0.77	0.33	17.3	43.7	19.8	19.3	3.18	5.37E+23	0.85
LG	0.01	0.75	0.72	0.45	0.01	0.61	0.64	0.32	0.2	50.0	13.3	36.6	2.98	1.68E+23	0.23
LH	0.08	0.67	1.16	0.44	0.06	0.58	1.03	0.33	6.4	38.6	29.6	25.4	2.63	3.54E+23	0.35
LI	0.16	0.74	1.20	0.40	0.05	0.56	1.06	0.30	22.3	37.8	21.7	18.2	2.83	3.95E+23	0.45

2.2.3 Examples of Preliminary SAXS Results

Figure 2.7 shows SAXS cross section curves for two UCSB SMS, CM3 and CM11, for both irradiated and baseline conditions. The CM11 scattering curve has been increased by an order of magnitude to enable comparisons between the two alloys. Figure 2.8 shows the corresponding nano precipitate size distributions, including one for CM16. Note, determining size distributions and $\langle r_p \rangle$ does not require knowledge of the nano precipitate SLD. In order

to get a preliminary estimate of the corresponding N_p and f_p , SLD corresponding to the G-phase and pure Cu precipitates were used. The results are given in Table 2.8. The SAXS-APT $\langle d \rangle$ agreement is good and the f_p values are reasonably similar in 2 out of the 3 cases. The results for a much larger ATR-2 SAXS database and refined analysis will be reported in the future.

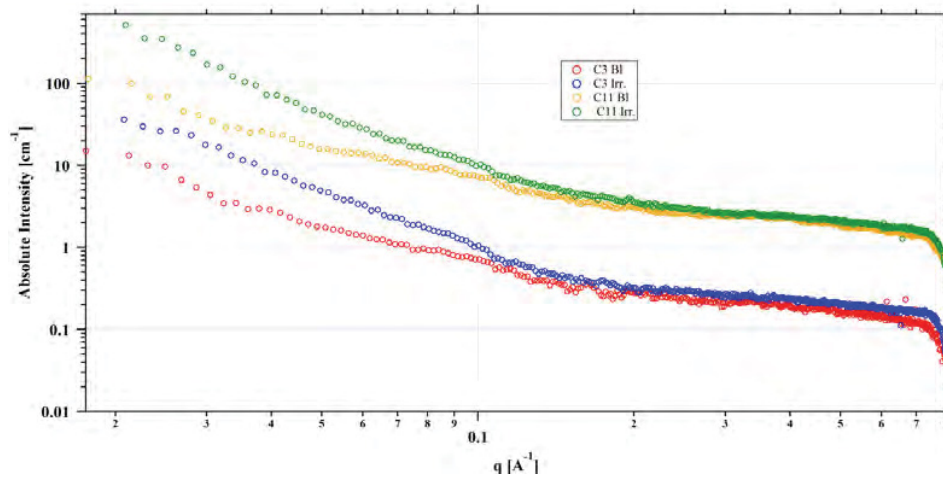


Figure 2.7 Representative SAXS patterns for unirradiated and ATR-2 irradiated CM samples. The curves are offset for clarity

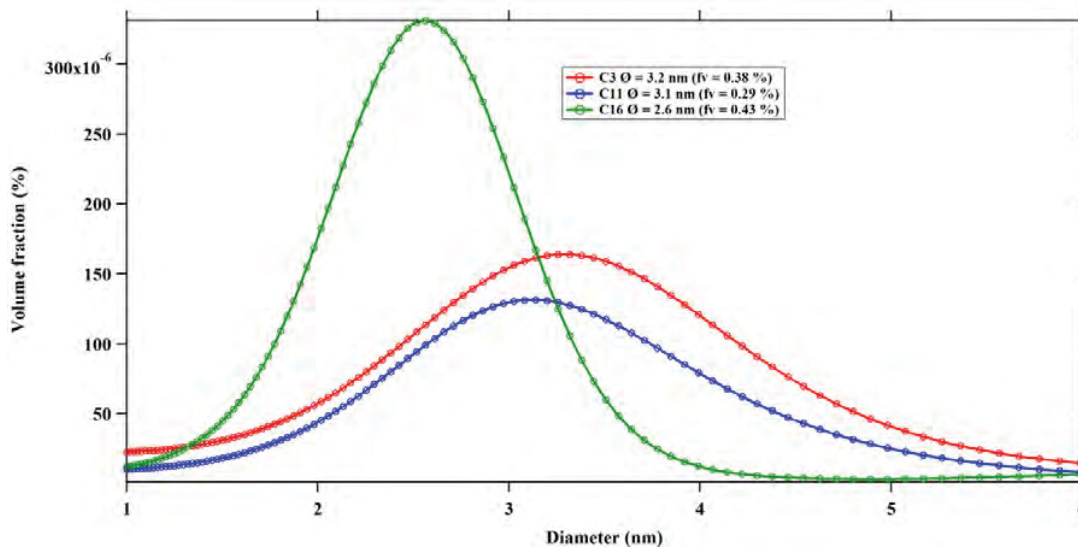


Figure 2.8 Quantitative SAXS results for 3 CM-series alloys.

Table 2.8 Fitted SAXS $\langle d_p \rangle$ (nm) and f_p (%) for 3 CM-series alloys and their compositionally similar L-series counterparts measured by APT.

CM alloy	SAXS Data			APT Data		
	$\langle d_p \rangle$ (nm)	f_p Cu SLD (%)	f_p G-phase SLD (%)	L alloy*	$\langle d_p \rangle$ (nm)	f_p (%)
CM3	3.2	0.24	0.38	LG	3.0	0.23
CM11	3.1	0.19	0.29	LC	3.3	0.71
CM16	2.6	0.38	0.43	LI	2.8	0.45

*Note that no APT data is available for CM alloys, so the SAXS data is compared to APT data from compositionally similar L alloys, for which APT data has been taken.

3. Data Analysis and Evaluation

3.1 Property-Property Correlations

Here we compare limited ATR-2 SST, SPT and μ H test data to each other and to existing values from surveillance reports. These preliminary results generally show good agreement with previously established correlations.

3.1.1 Shear Yield – Tensile Yield

Previous work at UCSB established a correlation between the SST σ_y and the SPT (τ_y), as $\sigma_y = 1.77\tau_y$, for all the RR alloys with a very wide range of strengths [9]. Figure 3.1 shows the previous data and fit line in red. New baseline data and fit line for the surveillance alloys, along with 4 RR steels with a wide range of strengths, are shown in blue with a near ideal Von Mises slope: $\sigma_y = 1.74\tau_y$. In general the new data is slightly more scattered and there is one data point with a very low σ_y .

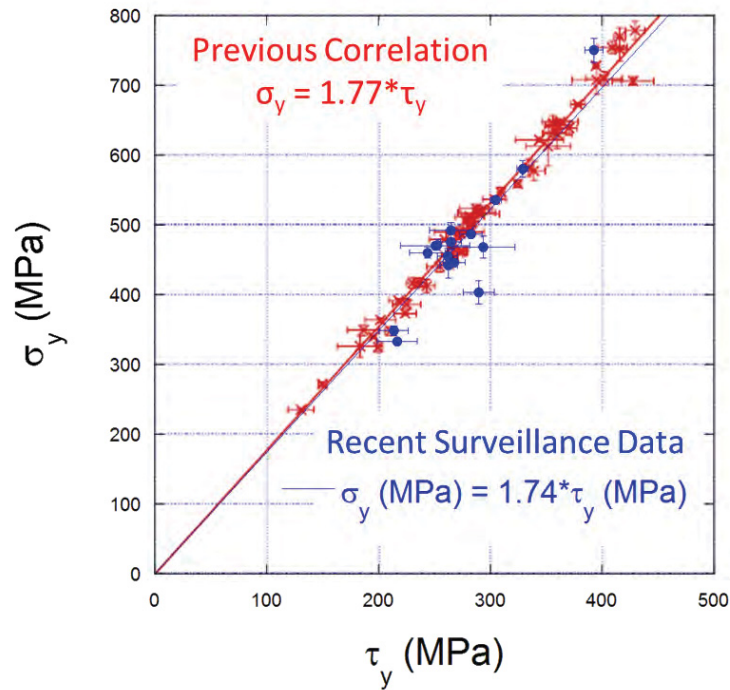


Figure 3.1 Tensile versus shear yield stress for a matrix of Rolls Royce alloys (red) that were previously tested, and a matrix of surveillance and Rolls Royce alloys tested recently as part of this experiment (blue).

3.1.2 Microhardness – Yield Stress Correlations

Changes in 10 kg Vickers microhardness (ΔH_v) after irradiation can be correlated with corresponding changes in yield stress ($\Delta \sigma_y$). This is shown in Figure 3.2 for a subset of the surveillance alloys in cup 7. The best-fit line for this data gives $\Delta \sigma_y$ (MPa) = 3.23 * ΔH_v (kg/mm²) very close to our nominal correlation of $\Delta \sigma_y$ (MPa) = 3.33 * ΔH_v (kg/mm²). Simple empirical irradiation hardening correlations in the literature report $\Delta \sigma_y = C \Delta H_v$, with $C \approx 3.0 - 3.6$ MPa/kg-mm² [18]. Note, μH inherently measures an average flow stress between 0 and 10% strain, rather than σ_y [19]. An extensive unpublished study of a large database by Williams and Odette showed that C depends on both the unirradiated and irradiated μH , and is influenced by the reduced post yield strain hardening following irradiation. Applying the

relations derived in this work gives an average $C \approx 3.4$ for the ATR-2 steels. Thus the use of $3.33 \text{ MPa}/[\text{kg}/\text{mm}^2]$ is reasonable, but will be refined by a much larger ATR-2 database.

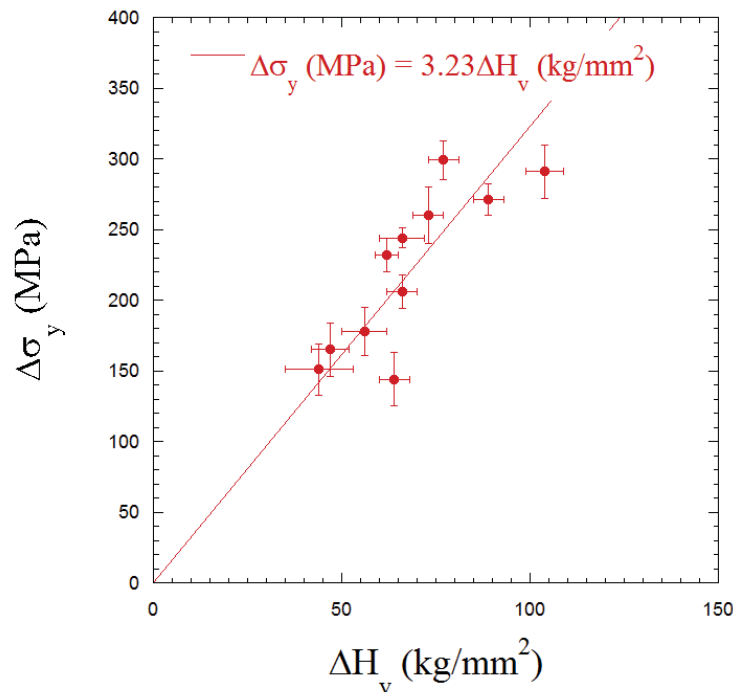


Figure 3.2 Change in tensile yield stress versus change in microhardness for a subset of surveillance alloys in cup 7.

3.2 Microstructure-Property Correlations

The dominant hardening features in RPV steels at high 80 year extended life fluence are Cu-rich precipitates and MNSPs. Dispersed barrier models of irradiation (precipitation) hardening can be used to relate $\Delta\sigma_y$ to f_p and r_p . Figure 3.3 shows the $\Delta\sigma_y$ for alloys in Cup 7 versus $\sqrt{f_p}$, measured with either SANS (red) and APT (blue). The SANS data are all surveillance alloys, and the APT data measured are all UCSB SMS. There is good general agreement between hardening and $\sqrt{f_p}$ for both techniques, though the SANS data points show slightly more hardening at a given f_p . This could suggest a relative bias in the measurement of f_p between the two techniques, or a difference in the unirradiated dispersed barrier hardening between the surveillance alloys and SMS. Future research will include

obtaining APT data on the surveillance alloys and SANS data on the UCSB SMS, in part so as to better clarify this issue.

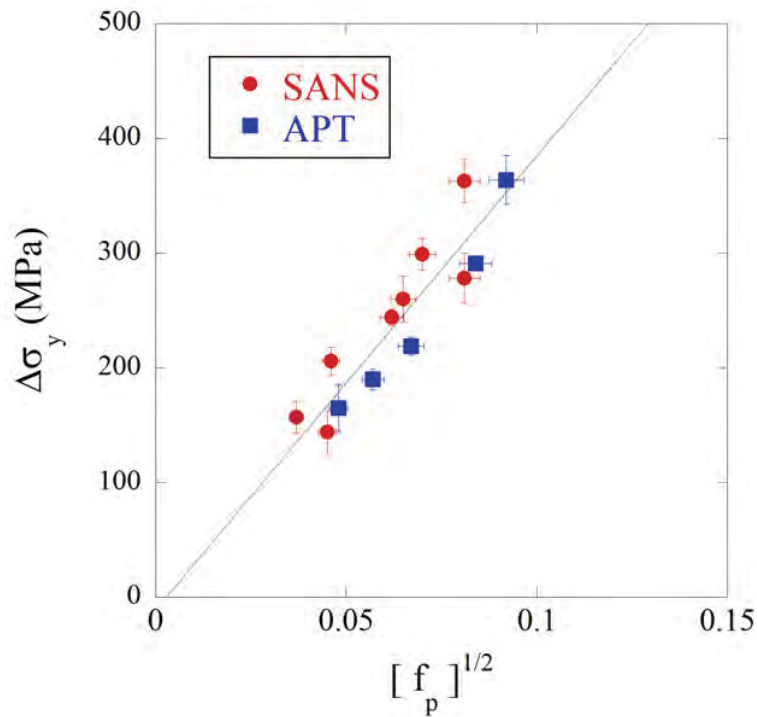


Figure 3.3 Hardening versus square root of precipitate volume fraction for surveillance alloys (red), measured by SANS, and UCSB SMS (blue), measured by APT.

3.3 Comparison with Surveillance Programs

The surveillance alloys were included in the ATR-2 irradiation in order to compare $\Delta\sigma_y$, at high flux, to the corresponding changes at lower power reactor flux. Thus it is important to demonstrate the ATR-2 surveillance alloys have unirradiated properties consistent with those found in surveillance reports. Note that these reports are now generally available through the Reactor Embrittlement Archive Project (REAP) led by Oak Ridge National Lab [20]. Figure 3.4 compares the measured yield (σ_y) and ultimate tensile stress (s_u) found in the surveillance reports to those measured by UCSB. A 1:1 agreement line is shown in black. In general, the surveillance report and UCSB data match fairly close, but there is slight bias in the surveillance data with, which are on average $\approx 5\%$ higher for σ_y and 3%

higher for s_u than the UCSB results. This difference is fairly small considering the potential material variability, and the different tensile specimens used: standard ASTM round-bar tensile specimens in the surveillance reports and the much smaller UCSB SSJ-2 type SST.

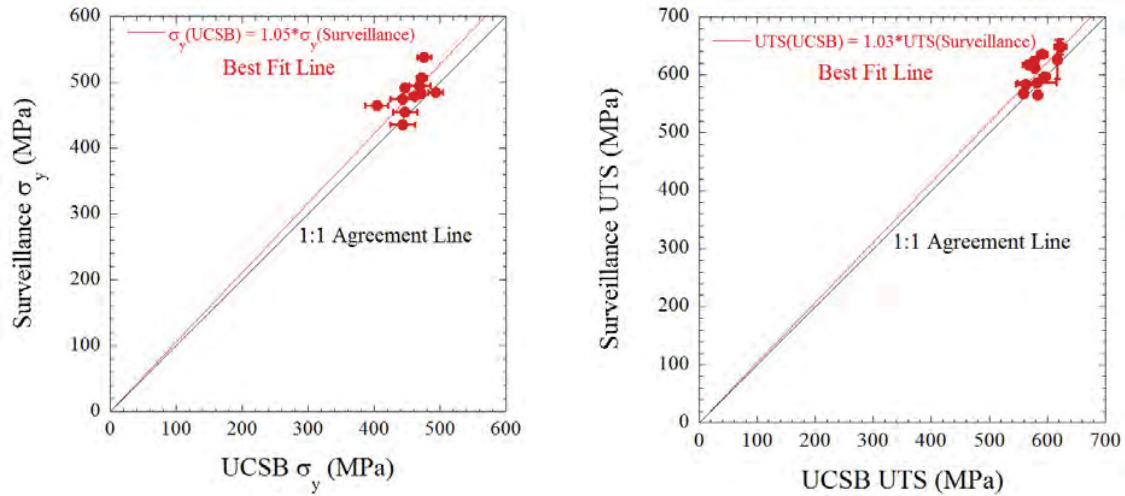


Figure 3.4 Comparison between UCSB and surveillance unirradiated baseline data for σ_y (left) and s_u (right).

The main goal of this work is to develop low flux ΔT models beyond the fluence range available in the existing surveillance database. ATR-2 reached high fluence, but at a higher flux. However, we will ignore possible flux effects in the case of the surveillance data for the time being, though this is a large focus of future work. Figure 3.5 shows $\Delta\sigma_y$ versus fluence for 9 surveillance alloys having either low Cu (left < 0.07) or higher Cu (right > 0.07). The data at lower fluence ($< 1 \times 10^{20}$ n/cm²) is from actual surveillance programs and the highest fluence data points are from the ATR-2 irradiation. For the low Cu steels, the $\Delta\sigma_y$ generally increases approximately linearly with fluence. The higher Cu steels show a large increase in $\Delta\sigma_y$ at low fluence followed by a steady or slightly accelerated increase to the ATR-2 condition. Effects of Cu and Ni are observed in both cases, and the lower 0.14%Cu, 0.19%Ni steel hardens much less than the other with higher concentrations of these solutes.

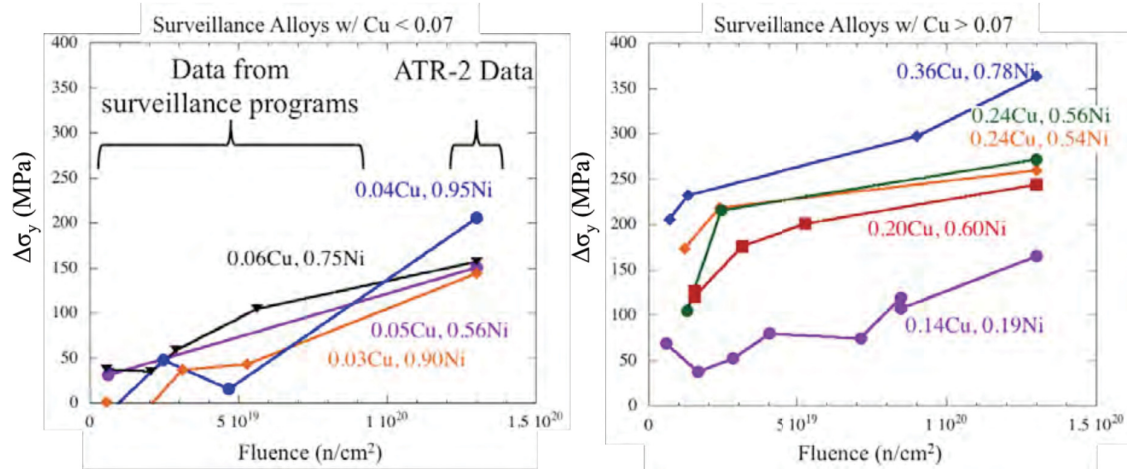


Figure 3.5 $\Delta\sigma_y$ versus fluence for the 9 new surveillance alloys with < 0.07 wt.% Cu (left) and > 0.07 wt.% Cu (right).

Figure 3.6 shows the measured hardening from ATR-2 cup 7 along with predictions from various existing ΔT surveillance database based Eason-Odette-Nanstad-Yamamoto (EONY) and ASTM E900 models, as well as a $\Delta\sigma_y$ model derived from the UCSB Irradiation Variables (IVAR) database. In the case of both EONY and E900 the ΔT predictions have been converted to $\Delta\sigma_y$ using established correlations [6]. With few exceptions, all of these the models under-predict the high fluence ATR-2 data. The under-predictions are as much as 129 MPa, averaging 62 and 54 MPa for EONY and E900, respectively. The under-predictions for the IVAR model are generally slightly less, averaging 45 MPa. Again these comparisons do not account for potential flux effects. A major focus of future work will be on PIE on lower fluence ATR-2 conditions to more directly bridge to the surveillance data and help to better understand flux effects.

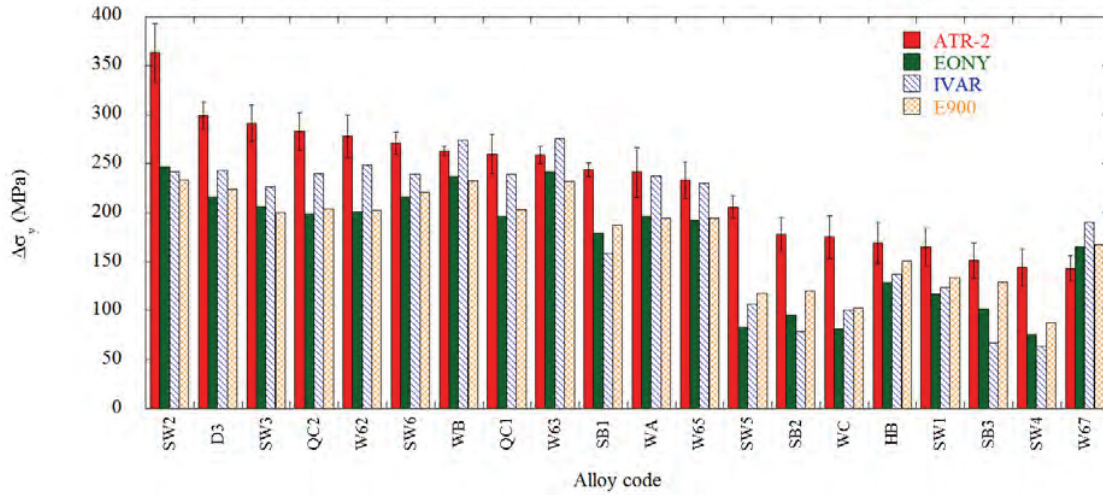


Figure 3.6 ATR-2 cup 7 hardening for various surveillance alloys along with predictions from existing models.

Figure 3.7 shows a similar comparison for the UCSB L and CM-series SMS and the program alloys that have been previously irradiated but not in surveillance programs. Here only the EONY and E900 predictions are compared with the ATR-2 data. In this case, both models generally under-predict, but E900 gives 4 very large over-predictions for alloys CM20, CM17, CM7 and CM6, which all have high Ni from 1.59 to 1.70%. The average error for the EONY model is a 78 MPa under-prediction, though the E900 model has an average 24 MPa over-prediction, due to the very large over-predictions in the high Ni steels. Another measure of the quality of the models is the root mean square difference (RMSD), calculated as

$$RMSD = \sqrt{\frac{\sum_{i=1}^n (X_A - X_P)^2}{n}}$$

where n is the number of data points, X_A is the measured ATR-2 $\Delta\sigma_y$ and X_P is the predicted $\Delta\sigma_y$ from a given model. The RMSD for the EONY model is 89 MPa vs 159 MPa for the E900 model.

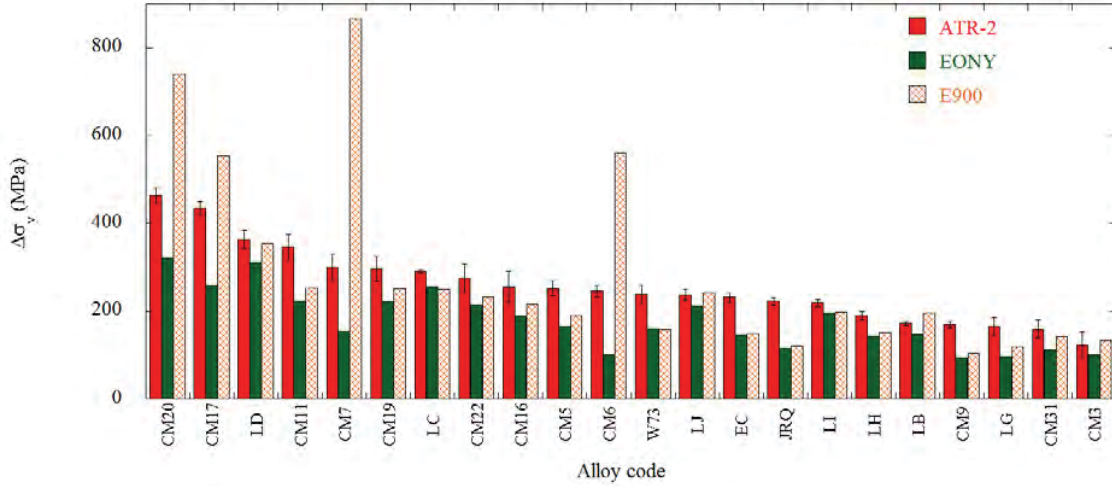


Figure 3.7 ATR-2 cup 7 hardening for the UCSB SMS and program alloys along with predictions from existing models.

3.4 Comparisons with Previous Test Reactor Data

The UCSB SMS, program alloys and a number surveillance plates and welds have previously been irradiated in a number of other test reactor irradiations over a wide range of flux and fluence. Figure 3.8 and Figure 3.9 compares examples of data from high Cu steels and low Cu steels, respectively, with the EONY predictions. The highest fluence data point on each plot is the recent data from ATR-2. The plots are for $\Delta\sigma_y$ versus the square root of both the actual fluence (ϕt) and an effective fluence (ϕt_e) to account for flux effects. The same types of plots for the other alloys are shown in Appendix A.6. The ϕt_e is determined by a simple flux scaling model in the form

$$\phi t_e = \phi t \left(\frac{\phi_r}{\phi} \right)^p$$

where ϕ_r is an arbitrary reference flux, set at 3×10^{11} n/cm²-s, and p the flux-scaling power. Previous studies have found that $p \approx 0.25$ collapses data for a very wide range of flux (\approx a factor of 1200) into a much narrower ϕt_e trend band [6]. Note both higher and lower p values have also been found, ranging from ≈ 0.15 to 0.5. As shown in Figure 3.8 and Figure 3.9, the

ATR-2 data is under-predicted by EONY and shows a distinct upswing relative to the data at lower flux and fluence.

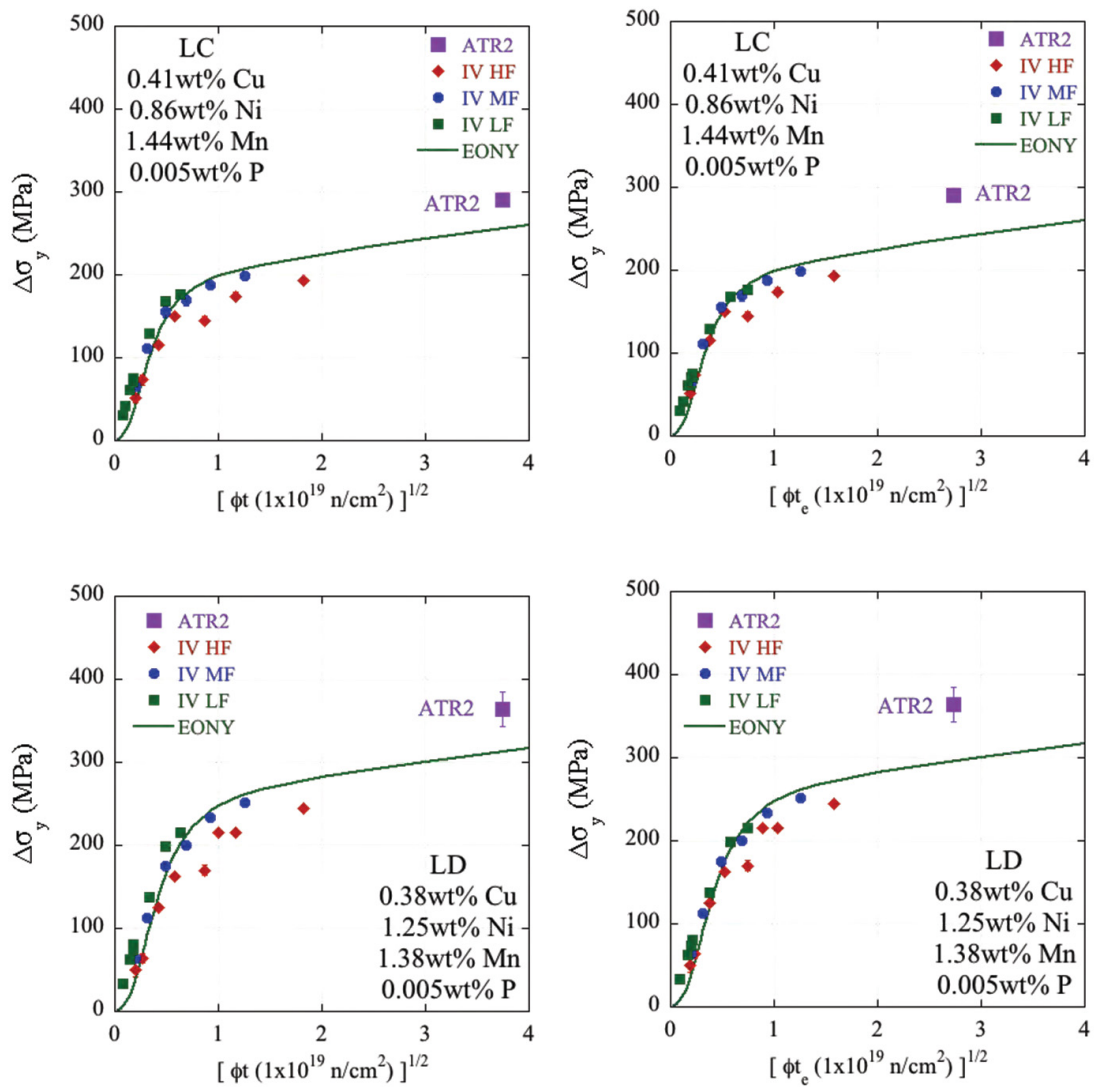


Figure 3.8 $\Delta\sigma_y$ versus the square root of fluence (left) and effective fluence (right) for two high Cu ($\approx 0.4\%$), steels with 0.86%Ni (top) and 1.25%Ni (bottom) from the UCSB SMS matrix for a wide number of irradiation condition.

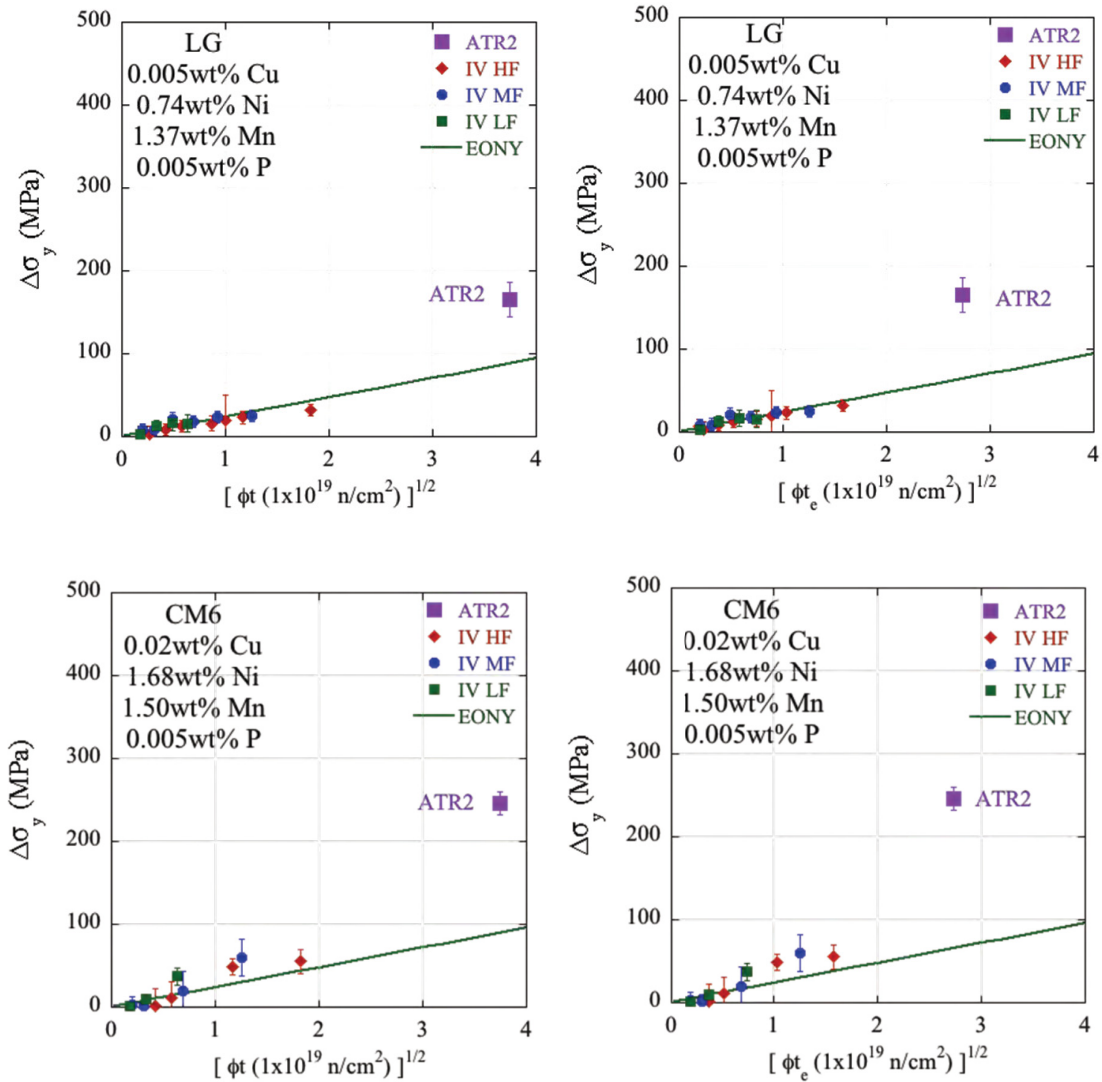


Figure 3.9 $\Delta\sigma_y$ versus the square root of fluence (left) and effective fluence (right) for two low Cu ($\approx 0.01\%$), steels with 0.74%Ni (top) and 1.68%Ni (bottom) from the UCSB SMS matrix for a wide number of irradiation condition

3.5 The Effect of Chemistry on Precipitation and Hardening

The UCSB SMS have systematic variations in Cu, Ni, Mn and P thus they provide a basis to directly assess alloy composition effects on precipitation and hardening. Figures compare data from ATR-2 cup 7 to two conditions from the IVAR experiment, T6 ($\phi = 1 \times 10^{12} \text{ n/cm}^2\text{-s}$, $\phi t = 3.4 \times 10^{19}$) and T16 ($\phi = 3 \times 10^{11} \text{ n/cm}^2\text{-s}$, $\phi t = 1.6 \times 10^{19} \text{ n/cm}^2$).

Figure 3.10 shows the effect of Cu for both $\approx 0.8\%$ Ni (left) and $\approx 1.6\%$ Ni (right). Note the highest bulk Cu is $\approx 0.4\%$, but the data are plotted based on the estimated initial Cu in solution of $\approx 0.25\%$. The effect of Cu is generally similar, but somewhat weaker at the higher ATR-2 fluence.

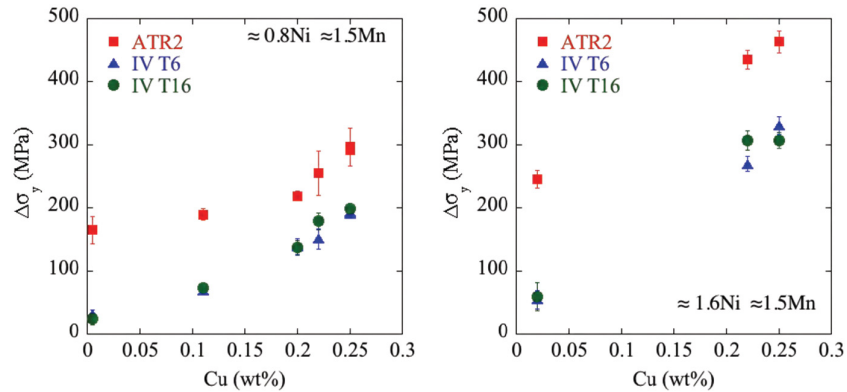


Figure 3.10 $\Delta\sigma_y$ versus Cu content at either $0.8\% \text{ Ni}$ (left) or $1.6\% \text{ Ni}$ (right) for two different conditions from the IVAR experiment (T6 and T16) and cup 7 from the ATR-2 experiment.

3.5.1 Effect of Ni

Figure 3.11 shows the effect of Ni at both $\approx 0.0\%$ Cu (left) and $\approx 0.4\%$ bulk Cu right. The effect of Ni is generally similar, but stronger at the higher ATR-2 fluence.

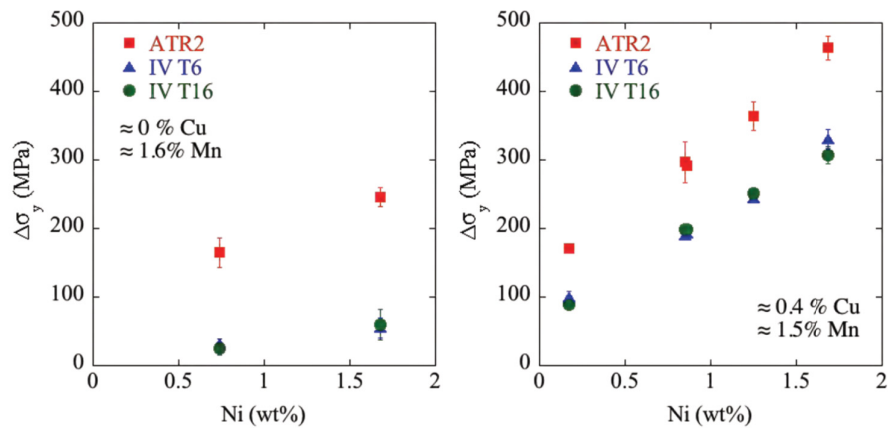


Figure 3.11 $\Delta\sigma_y$ versus Ni content at either $0.0\% \text{ Cu}$ (left) or $0.4\% \text{ Ni}$ (right) for two different conditions from the IVAR experiment (T6 and T16) and cup 7 from the ATR-2 experiment.

3.5.2 Effect of Mn

Figure 3.12 shows the effect of Mn at 0.0%Cu (left) and 0.4% bulk Cu (right) at 0.8%Ni. The effects of Mn are weak in all cases.

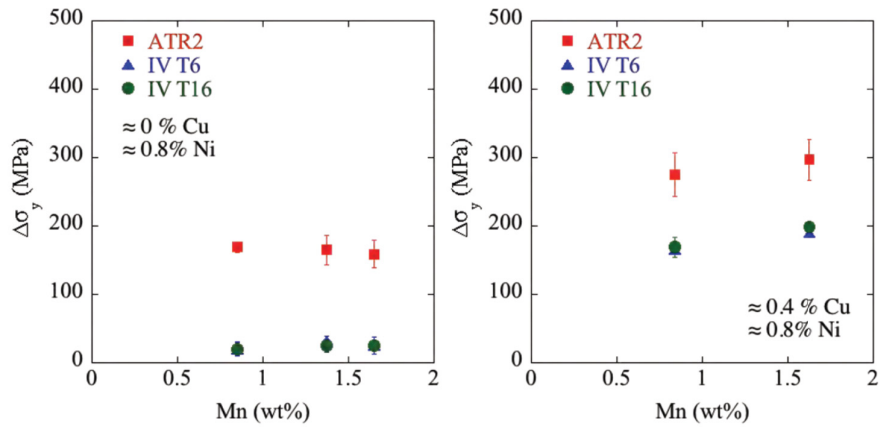


Figure 3.12 $\Delta\sigma_y$ versus Mn content at either 0.0%Cu (left) or 0.4%Cu (right) for two different conditions from the IVAR experiment (T6 and T16) and cup 7 from the ATR-2 experiment.

3.5.3 Effect of P

Figure 3.13 shows the effect of P at 0.0%Cu, 1.6%Mn and either 0.8%Ni (left) or 1.6%Ni (right). The effect of P is generally moderate, but is stronger for lower Ni and at higher ATR-1 fluence.

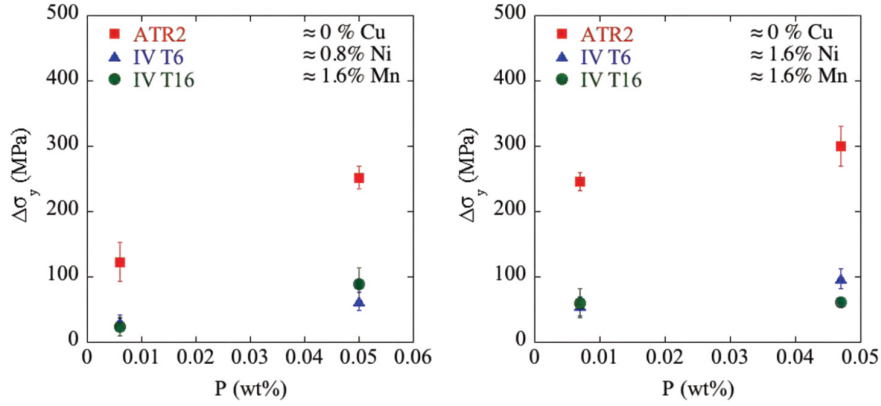


Figure 3.13 $\Delta\sigma_y$ versus P content at 0%Cu, 1.6%Mn and either 0.8%Ni (left) or 1.6%Ni (right) for two different conditions from the IVAR experiment (T6 and T16) and cup 7 from the ATR-2 experiment.

Figure 3.14 shows the APT f_p for a number of alloys irradiated to very high fluence in the ART-1 experiment ($\phi = 2.3 \times 10^{14}$ n/cm²-s, $\phi t = 1.1 \times 10^{21}$ n/cm²) plotted against the $\sqrt{(2\text{Ni} + \text{Cu})}$. The correlation is excellent. The precipitates are believed to be essentially fully phase separated in this case, and the behavior can be understood based on the fundamental thermodynamics of the Fe-Cu-Ni-Mn-Si system. A full discussion of the observed behavior is beyond the scope of this report.

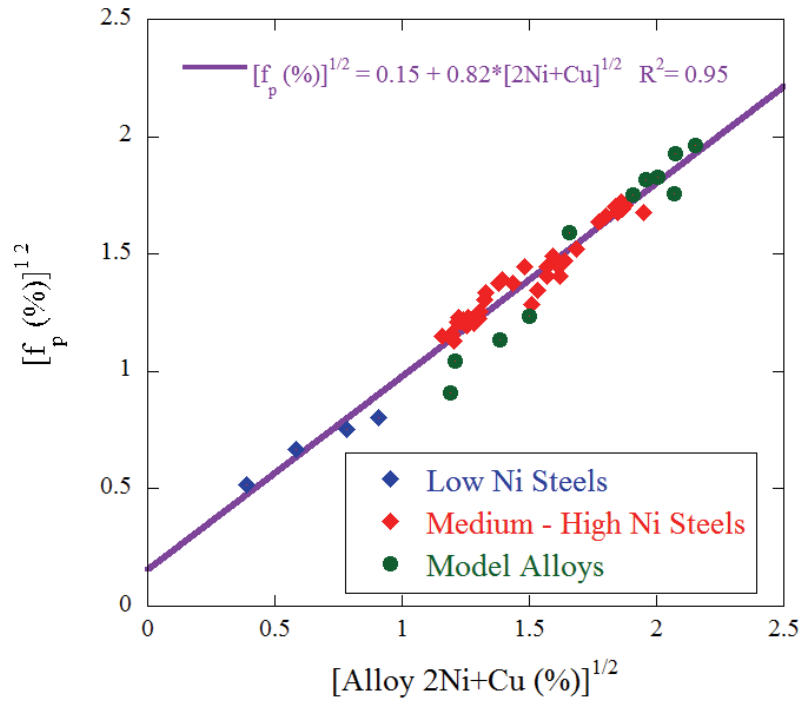


Figure 3.14 Square root of measured APT volume fraction versus square root of (2*Ni+Cu) determined by measuring the local APT bulk composition.

Figure 3.14 inspires consideration of a chemistry factor that depends only on Ni and Cu. Figure 3.15 plots the ATR-2 hardening for the SMS (blue symbols) as well as the surveillance and other program steels (pink symbols) for a least squares fit chemistry factor $CF = \sqrt{\{kNi + [Cu (< Cu_{max}) - Cu_o]\}}$ and a fitted maximum $Cu_{max} = 0.25$, $k = 0.27$ and $Cu_o = 0.03$. The data are reasonable correlated by this CF and are fairly similar for the SMS and other steels as shown by the colored fit lines

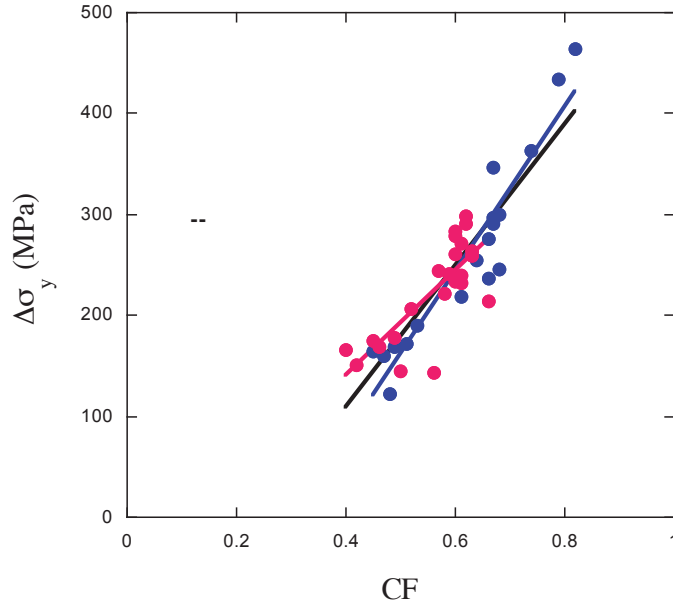


Figure 3.15 $\Delta\sigma_y$ versus a chemistry factor (CF) currently under development to predict hardening from an alloy's bulk composition for the surveillance alloys (blue) and UCSB SMS (pink).

3.6 Comparison of New ATR-2 Data to Previously Derived Microstructurally Based $\Delta\sigma_y$ Models

Previous studies have shown that the precipitate f_v can be modeled with a simple Avrami equation [6, 21, 22] as

$$f(\phi t_e) = f_{max} \left\{ 1 - \exp \left[- \left(\frac{\phi t_e}{\phi t_0} \right)^\beta \right] \right\} \quad (3.1)$$

Here f_{max} is the saturation f_p , ϕt_e is the effective fluence, ϕt_0 is the fluence requires to reach 63% of f_{max} and β is a parameter that depends on the kinetic rate controlling precipitation mechanisms [6, 21, 22]. For example, $\beta = 3/2$ corresponds to the case of diffusion controlled growth N pre-existing precipitates, while $\beta = 2.5$ corresponds to the case when the nucleation of precipitates is [6]. The $f_p(\phi t_e)$ curve has a sigmoidal shape when plotted on log plot ϕt_e . For diffusion controlled growth of N precipitates f_p initially increases with $3/2$ but slows at higher ϕt_e when most of the solute has been depleted from the matrix, saturating at full phase

separation. In the continuous nucleation case, f_p initially increases with the $5/3$ power of ϕt_e before slowing and saturating. In Cu-bearing alloys, CRPs rapidly grow to saturation long before MNSPs, so in these cases, a two feature Avrami model, CRP and MNSP, is needed. One (MNSP) or 2 (CRP + MMNSP) Avrami models were previously fit to the UCSB SMS database for 6 core steels [23]. The fit parameters for the Avrami models are the maximum f_{max} , the Avrami curve shape factor, β and the indexing fluence ϕt_0 when $f_p = 0.63f_{max}$. To mitigate the considerable covariance between these parameters, f_{max} and β were fixed at values independently estimate for both CRP and MNSP. The f_{max} for the CRP was determined based on each individual alloy's bulk Cu and Ni contents. The f_{max} for MNSPs were based on the very high fluence ATR-1 data, believed to represent nearly full phase separation. The corresponding β was fixed at 1.5 for CRP term due to rapid nucleation, while the β for the MNSP was fixed at 2.5, to represent a slower precipitate nucleation rate. This left $\phi t_{0,crp}$ and $\phi t_{0,mnsp}$ as the single paramters.to the to be best fit to microstructural database on the 6 core alloys.

While the UCSB ATR-2 data will ultimately be used in fitting the Avrami model, here we simply compare the new data to the previous f_p model for the 6 core alloys in Figure 3.16. The previously acquire data points span more than 3 orders of magnitude in flux. The model, assuming $p = 0.25$ shows remarkable agreement with the new ATR-2 data points, shown in large red circles, in 4 of the 6 cases. The ATR-2 f_p is slightly lower in one case (0.23%) and significantly lower in another case (0.48%). It should be noted that only 1-2 tips of each alloy have been analyzed, though more specimens will be run and analyzed shortly.

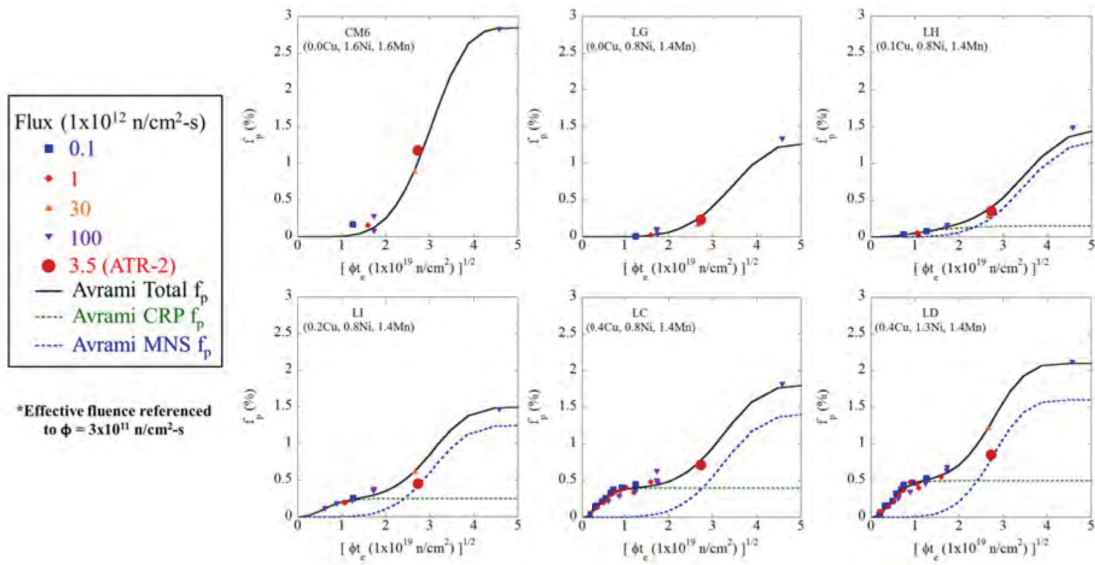


Figure 3.16 Preliminary UCSB Avrami model predicting f_p as a function of fluence for the core UCSB SMS. The ATR-2 data points (shown in large red circles) were not used in the fitting of the model.

The fitted f_p Avrami model can be converted to $\Delta\sigma_y$ predictions, by using an prototypical relation for the precipitate hardening contribution $\sigma_{yp} = 5300 \text{ MPa}\sqrt{f_p}$ and combining this with 180 MPa of pre-existing Mo_2C dispersed barrier hardening in both unirradiated and irradiated steels based on a simple root sum square superposition law [15]. Figure 3.17 the compares the previously derived Avrami $\Delta\sigma_y$ model to the new ATR-2 data. The Avrami model is in excellent agreement in 3 cases and over-predicts the ATR-2 $\Delta\sigma_y$ for the 3 others. Obviously, however, the overall ATR-2 database will be used to further refine the Avrami models.

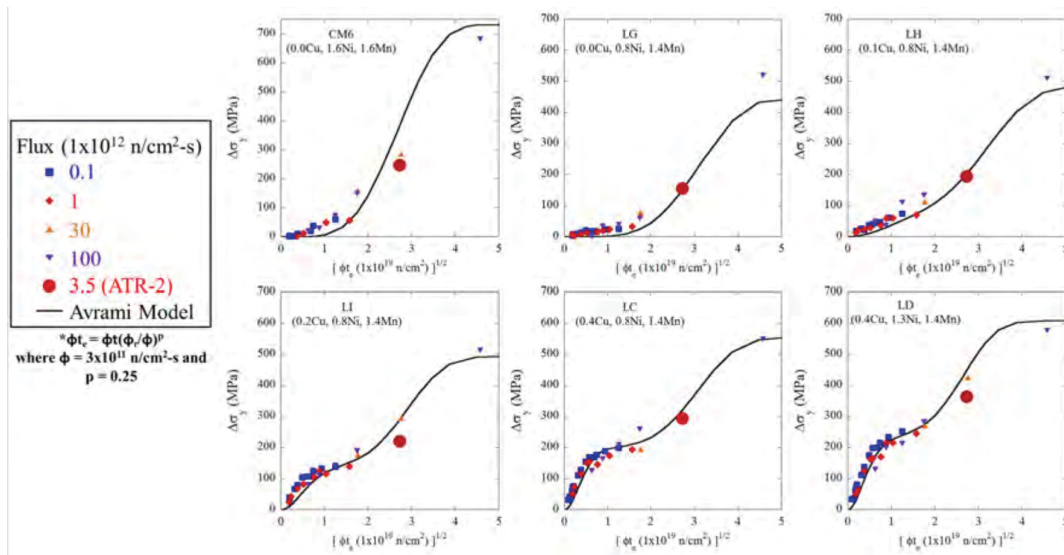


Figure 3.17 Preliminary UCSB Avrami model predicting $\Delta\sigma_y$ as a function of fluence for the core UCSB SMS. The ATR-2 data points (shown in large red circles) were not used in the fitting of the model.

4. TTS Predictions

Both power reactor $\Delta\sigma_y$ and CVN ΔT data are available in public domain surveillance reports found in the REAP database [20]. Figure 4.1 shows ΔT versus $\Delta\sigma_y$ plots of data for the 9 new the surveillance base metals (left) and welds (right). The solid lines are linear fits to the data, while the dashed lines are correlations developed by Odette and collaborators based on a large independent RPV steel database [6]. The agreement between the correlation and the surveillance data for the nine materials is good, but the simple linear fits represent this particular subset of data slightly better. Note that the Odette correlations predict a slightly higher $\Delta T/\Delta\sigma_y$ for welds versus plates. The $\Delta T/\Delta\sigma_y$ linear fit slopes are reversed values of $0.79^\circ\text{C}/\text{MPa}$ for base metals and $0.63^\circ\text{C}/\text{MPa}$ for welds. A linear best fit C for both product forms gives $0.67^\circ\text{C}/\text{MPa}$, which is close to the canonical value of $0.7^\circ\text{C}/\text{MPa}$ long proposed by UCSB for converting irradiation hardening to embrittlement estimates [24]. Note the results are also broadly consistent with other work in the literature. It should be emphasized

that any average conversion factor ($^{\circ}\text{C}/\text{MPa}$) may not be fully accurate for a particular RPV steel.

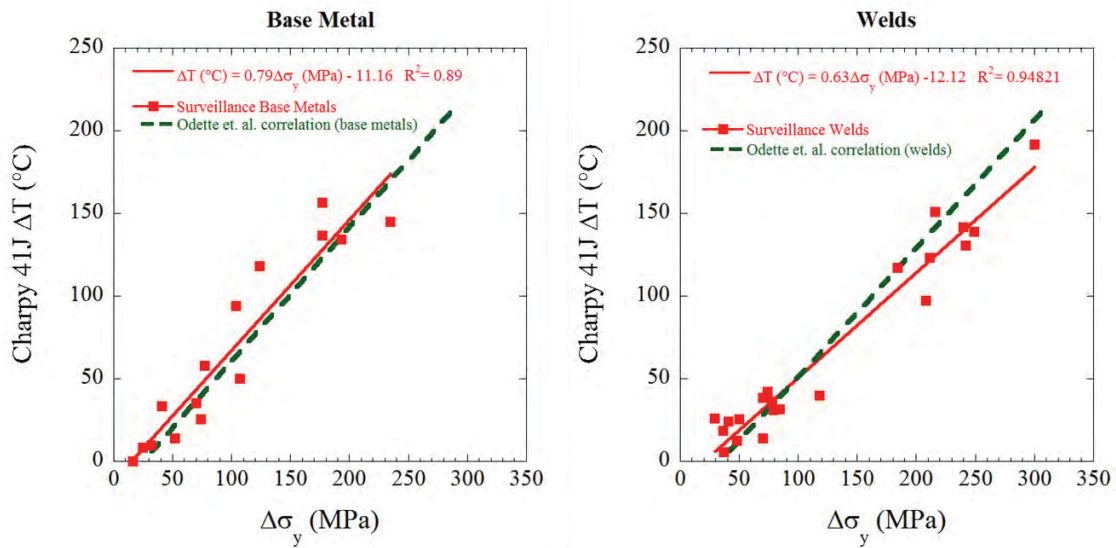


Figure 4.1 Charpy measured ΔT versus tensile measured $\Delta\sigma_y$ for surveillance specimens from REAP database showing different correlations for base metals and welds along with correlations developed by Odette et al.

Figure 4.2 shows two examples of ΔT versus fluence for a surveillance plate (left) and weld (right). The blue diamonds are actual surveillance Charpy ΔT data. The green diamonds are surveillance measured $\Delta\sigma_y$ converted to ΔT using the Odette et al. correlations. The measured and converted ΔT values agree very well. The red squares are the estimated ATR-2 ΔT derived from the ORNL microhardness tests at 1.4×10^{20} n/cm². The ΔT estimation procedure involves converting the ΔH_v to $\Delta\sigma_y$ using the nominal factor of 3.33 MPa/[kg/mm²] and then converting the $\Delta\sigma_y$ to ΔT using the correlations developed by Odette.

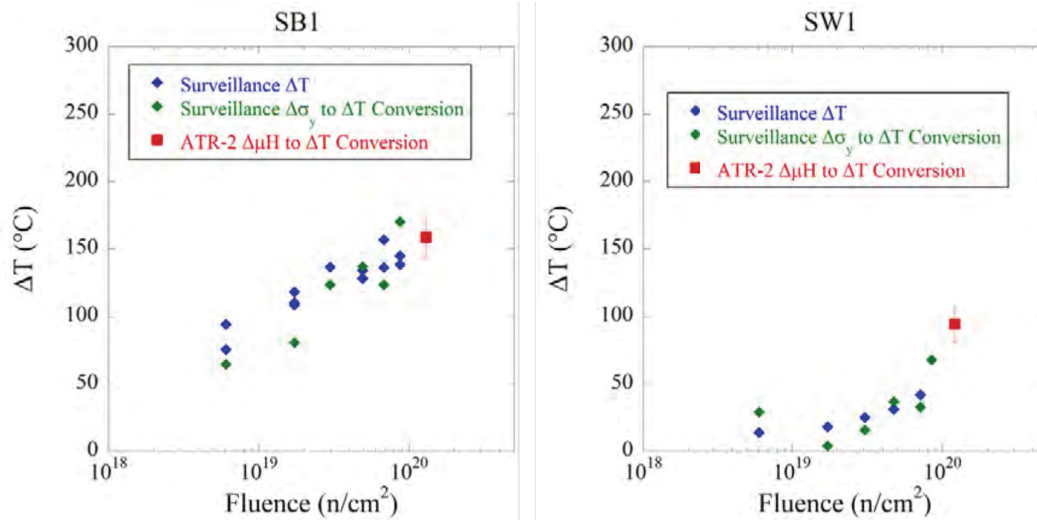


Figure 4.2 ΔT versus fluence for measured ΔT from surveillance programs (blue), measured $\Delta\sigma_y$ converted to ΔT using the Odette et al. correlations (green), and the ATR-2 $\Delta\mu H$ converted to ΔT (red) for a surveillance plate (left) and weld (right).

5. Summary and Future Work

Extended life operation of our nation’s light water reactors will require demonstrating that the reactor pressure vessels will operate within conservative safety margins. The UCSB ATR-2 experiment is designed to investigate embrittlement at extended life fluences with several main goals. First, it will add to the general understanding of the underlying mechanisms leading to RPV embrittlement by generating large databases of both microstructural and mechanical property data. These databases, in combination with others, will help to further refine correlations between microstructure and mechanical property changes under irradiation. A second goal is to develop physically based models of flux effects. Third, ATR-2 will further explore absolutely critical questions regarding, not the “if of LBP”, which is resolved, but more precisely the “when, where and how” of MNSP evolution as a function of flux, fluence, irradiation temperature and alloy composition. The experimental research will be tightly coupled to modeling studies in a UCSB collaboration

led by the University of Wisconsin (Dane Morgan PI). Here, modeling will inform experiments and vice versa.

In addition, the data generated in the experiment will be used to further refine and calibrate reduced order ΔT engineering prediction models, like the Avrami treatment described above. The reduced order models will be fit to both massive worldwide test reactor (including ATR-2 and IVAR) and surveillance databases, in support of robust regulatory models for extended life. Other ATR-2 PIE objectives include post irradiation annealing hardening studies both to explore critical mechanisms and as a possible remediation tool. Further ATR-2 PIE will address unresolved Master Curve issues like shape changes and ΔT shifts in highly embrittled steels.

While we have made major progress in about 9 months of PIE, the data and analysis reported here is just the tip of the iceberg. It is difficult to precisely quantify what remains to be done since we are engaged in what we describe as road mapped discovery research, in a way that does not make this an oxymoron. The most open ended aspect of future work is microstructural characterization. However, with appropriate effort and creativity, we hope that characterization of the nano-precipitates will be facilitated by the use of synchrotron facilities, especially the BNL NLS-II light source. However, Table 5.1 illustrates unmet PIE tests in terms of alloy-conditions and types of tests that remain to be completed for the 172 alloys, where S are the number of remaining specimens and A are the number of remaining alloys for a particular condition.

Table 5.1 Summary of remaining alloys/samples each in condition as well as remaining tests to complete.

Cup	ϕt (10^{19} n/cm ²)	T _{irr} (°C)	DCTs		Tensile		DMCs		Number of Tests		
			S	A	S	A	S	A	SST	μ H APT SANS	SPT SAXS
1	5.11	247	4	1	0	0	10	10	NA	Selected	All
2	7.43	268	0	0	0	0	198	136	NA	Selected	All
3	10.35	280	0	0	139	44	120	84	All	Selected	All
4	11.90	268	0	0	0	0	103	80	NA	Selected	All
5	12.80	255	0	0	0	0	99	94	NA	Selected	All
6	13.70	285	14	1	19	1	4	2	All	Selected	All
7	13.90	291	0	0	47	0	132	73	All	Selected	All
8	13.70	293	0	0	9	0	182	135	All	Selected	All
9	13.20	293	14	1	18	1	5	1	All	Selected	All
10	12.30	319	0	0	0	0	103	85	NA	Selected	All
11	11.05	292	0	0	17	9	186	117	All	Selected	All
12	9.08	264	14	1	17	1	4	1	All	Selected	All
13	5.79	238	0		17	9	99	80	All	Selected	All

6. References

1. Odette GR and Lucas GE. "Embrittlement of nuclear reactor pressure vessels", *JOM* 2001;53:18–22.
2. Eason ED, Odette GR, Nanstad RK and Yamamoto T. "A physically-based correlation of irradiation-induced transition temperature shifts for RPV steels", *J. Nucl. Mater.* 2013;433:240–254.
3. "Standard Guide for Predicting Radiation-Induced Transition Temperature Shift in Reactor Vessel Materials," ASTM International, 2015; ASTM E900-15.
4. Odette GR and Yamamoto T. "Presentation on the Proposed E900 Standard to the ASTM subcommittee 10.02," 2015; Presented to the ASTM Subcommittee E10.02.
5. Odette GR and Nanstad RK. "Predictive reactor pressure vessel steel irradiation embrittlement models: Issues and opportunities", *JOM* 2009;61(7):17–23.
6. Eason ED, Odette GR, Nanstad RK and Yamamoto T. "A physically based correlation of irradiation-induced transition temperature shifts for RPV steels," Oak Ridge National Lab, 2007; ORNL/TM-2006/530.
7. "As-Run Thermal Analysis of the UCSB-2 Experiment in the ATR," 2016; ATR NSUF ECAR No. 3218, Project No. 30946

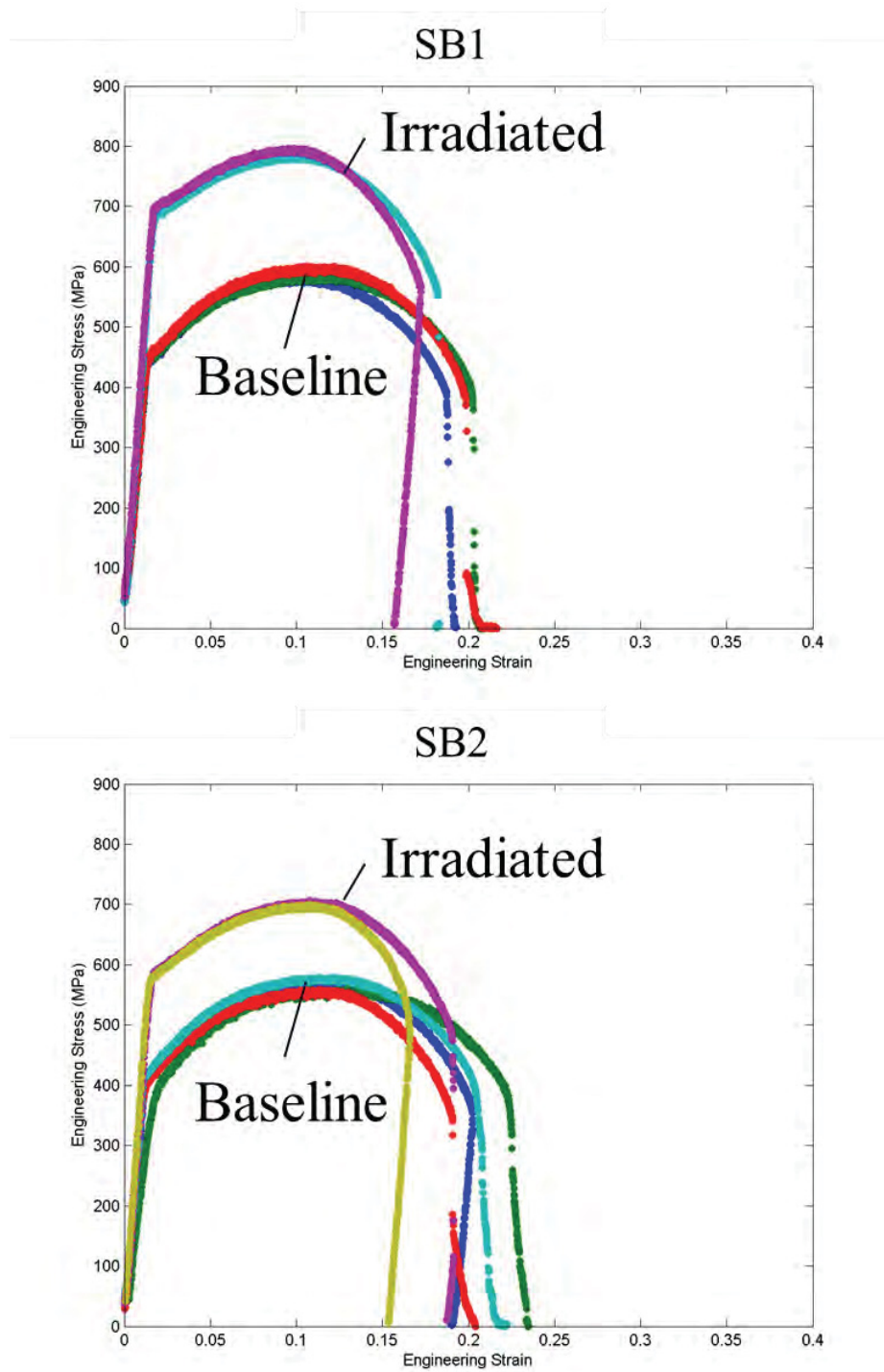
8. "As-Run Physics Analysis for the UCSB-2 Leadout Experiment in I-22," 2016; ATR NSUF ECAR No. 3219, Project No. 30946
9. Milot TS. "Establishing Correlations for Predicting Tensile Properties Based on the Shear Punch Test and Vickers Microhardness Data" [PhD Thesis]. University of California, Santa Barbara, 2013.
10. Cunningham NJ. "Study of the Structure, Composition, and Stability of Y-Ti-O nm-Scale Features" [PhD Thesis]. University of California, Santa Barbara, 2012.
11. Mader E. "Kinetics of irradiation embrittlement and the post-irradiation annealing of nuclear reactor pressure vessel steels" [PhD Thesis]. University of California, Santa Barbara, 1995.
12. Wirth BD. "On the Character of the Nano-Scale Features in Reactor Pressure Vessel Steels" [PhD Thesis]. University of California, Santa Barbara, 1998.
13. Alinger MJ. "On the Formation and Stability of Nanometer Scale Precipitates in Ferritic Alloys during Processing and High Temperature Service" [PhD Thesis]. University of California, Santa Barbara, 2004.
14. Alinger MJ, Odette GR and Hoelzer DT. "On the role of alloy composition and processing parameters in nanocluster formation and dispersion strengthening in nanostructured ferritic alloys", *Acta Mater.* 2009;57(2):392–406.
15. Wells PB, Yamamoto T, Miller B, Milot T, et al. "Evolution of manganese–nickel–silicon-dominated phases in highly irradiated reactor pressure vessel steels", *Acta Mater.* 2014;80:205–219.
16. Edmondson PD, Miller MK, Powers KA and Nanstad RK. "Atom probe tomography characterization of neutron irradiated surveillance samples from the R . E . Ginna reactor pressure vessel", *J. Nucl. Mater.* 2016;470:147–154.
17. Miller MK, Powers KA, Nanstad RK and Efsing P. "Atom probe tomography characterizations of high nickel, low copper surveillance RPV welds irradiated to high fluences", *J. Nucl. Mater.* 2013;437(1-3):107–115.
18. Busby JT, Hash MC and Was GS. "The relationship between hardness and yield stress in irradiated austenitic and ferritic steels", *J. Nucl. Mater.* 2005;336(2-3):267–278.
19. He MY, Odette GR, Yamamoto T and Klingensmith D. "A universal relationship between indentation hardness and flow stress", *J. Nucl. Mater.* 2007;367-370:556–560.
20. "Reactor Embrittlement Archive Project", *Oak Ridge Natl. Lab.* Accessed 06-30-2016,

<https://reap.ornl.gov>.

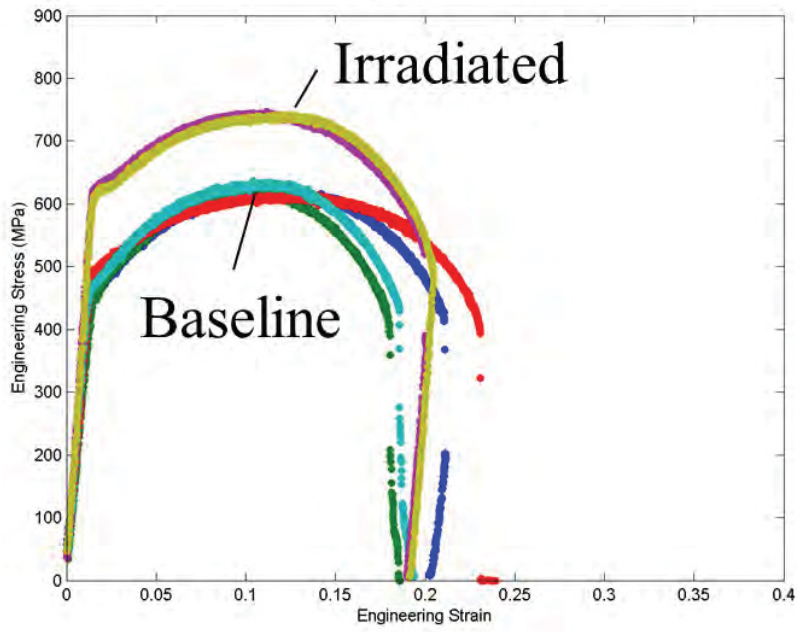
21. Odette GR, Yamamoto T and Klingensmith D. "On the effect of dose rate on irradiation hardening of RPV steels", *Philos. Mag.* 2005;85(4-7):779–797.
22. Porter DA, Easterling KE and Sherif MY. "Phase Transformations in Metals and Alloys" Third Edit. CRC Press, 2009.
23. Wells PB. "The Character, Stability and Consequences of Mn-Ni-Si Precipitates in Irradiated Reactor Pressure Vessel Steels" [PhD Thesis]. University of California, Santa Barbara, 2016.
24. Odette GR and He MY. "Cleavage toughness master curve model", *J. Nucl. Mater.* 2000;283-287:120–127.

Appendix A

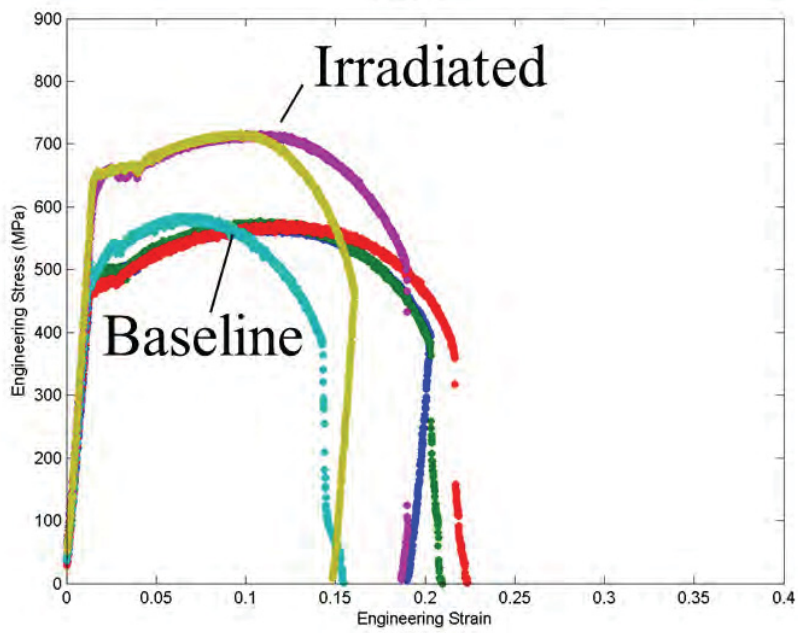
A.1 Comparison of Irradiated and Baseline Stress-Strain Curves for Surveillance Alloys



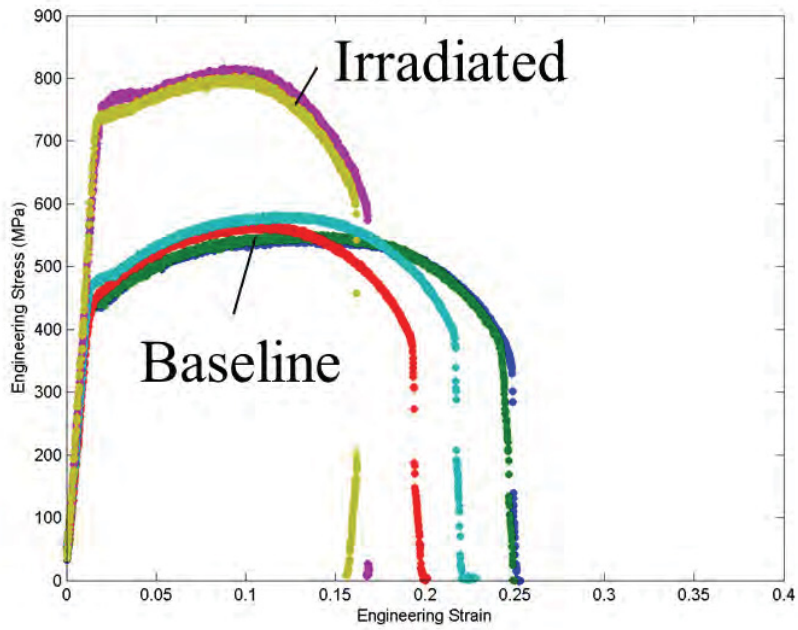
SB3



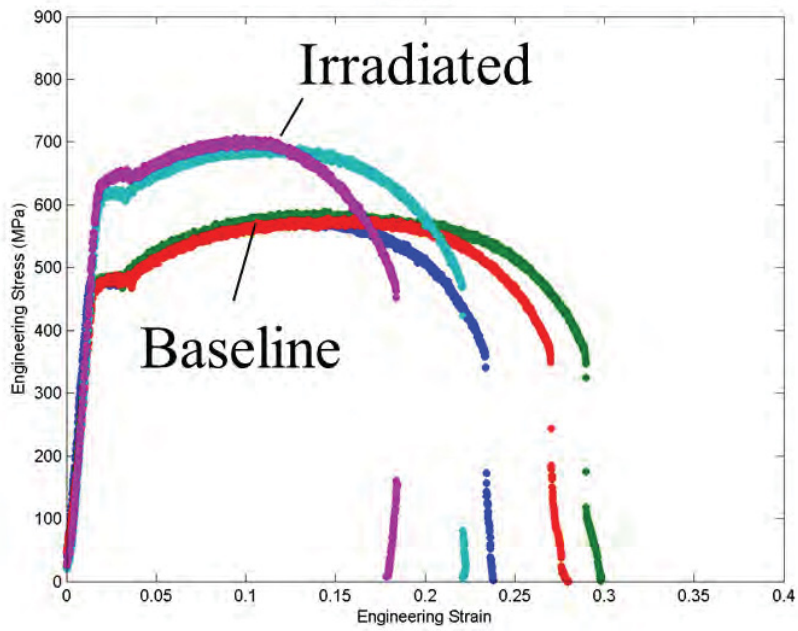
SW1



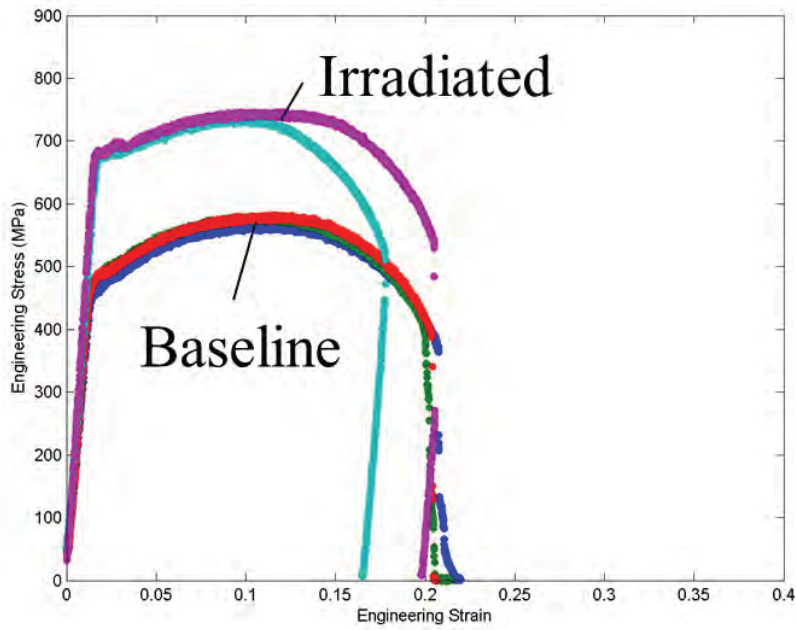
SW3



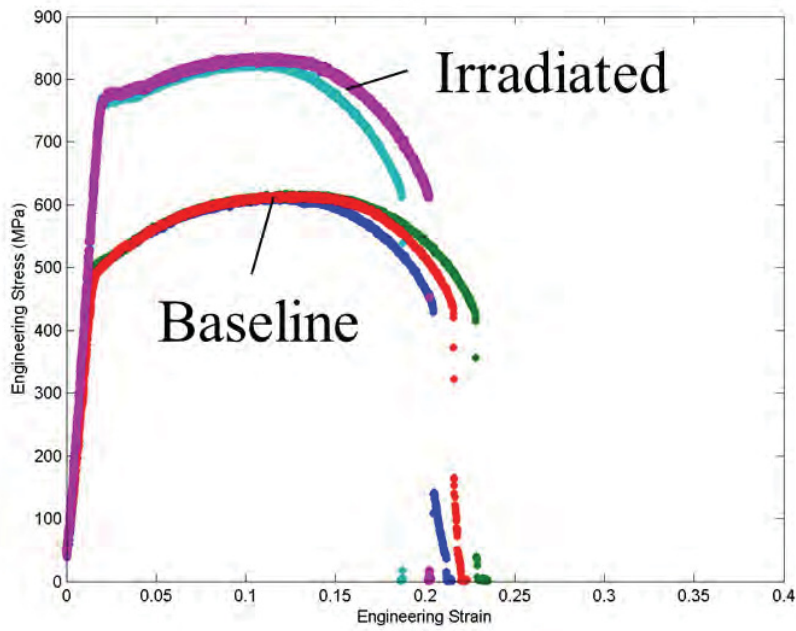
SW4



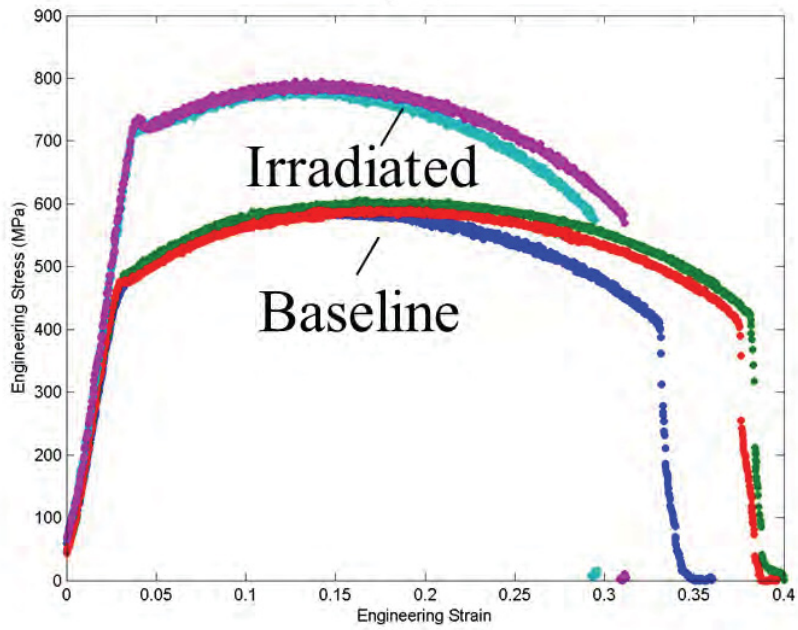
SW5



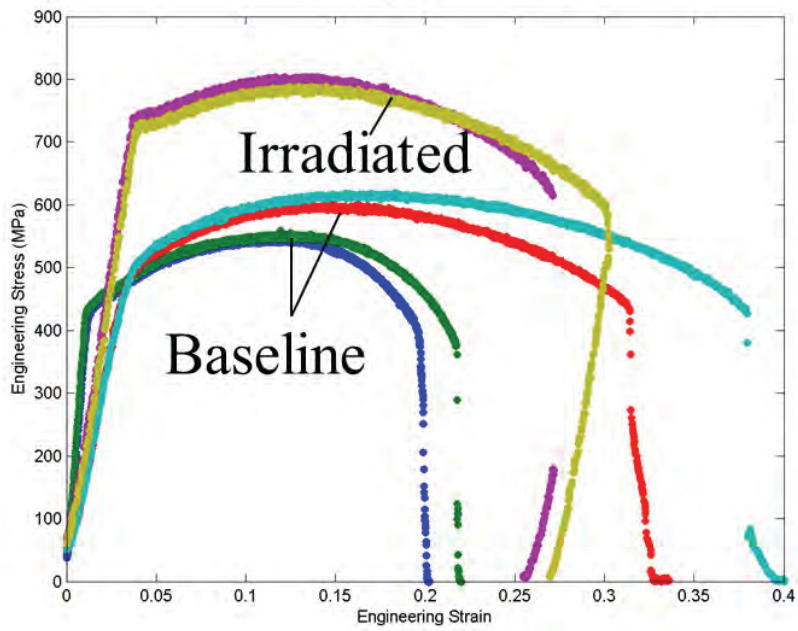
SW6



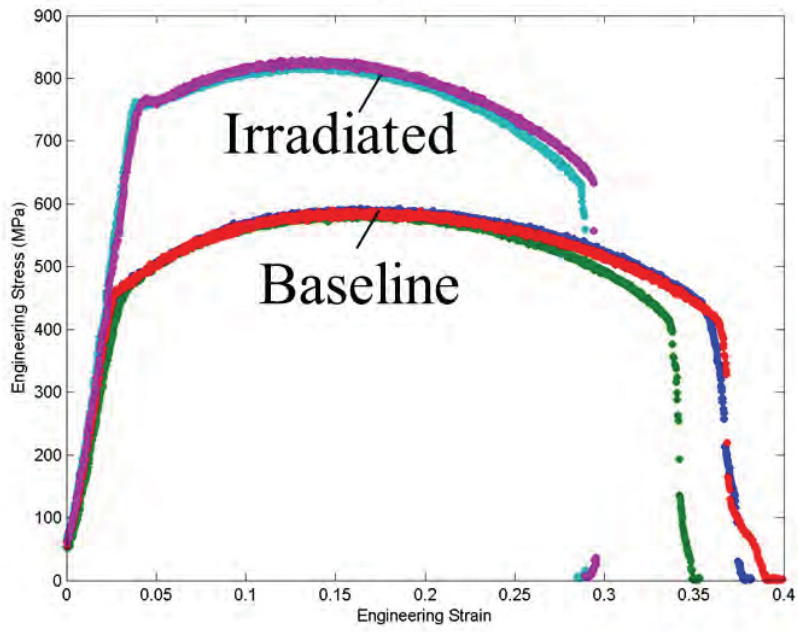
QC1



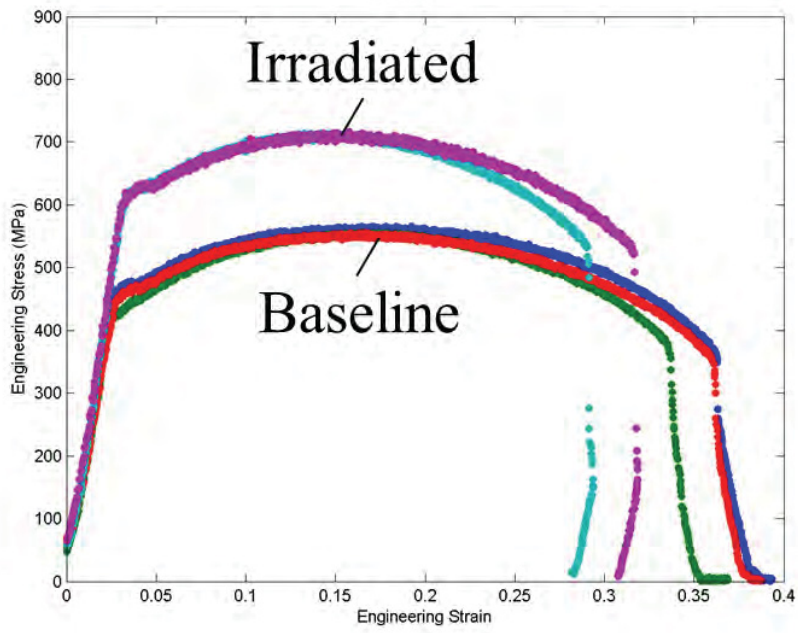
QC2



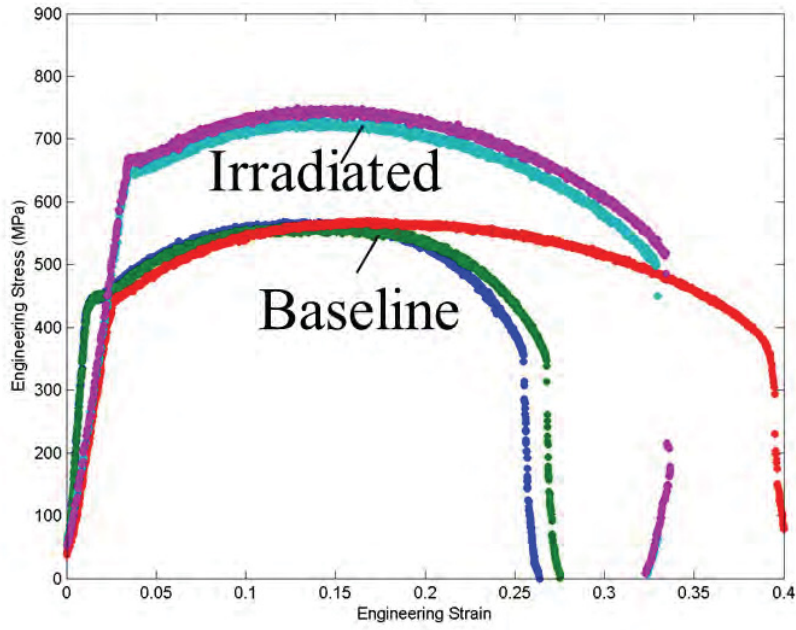
D3



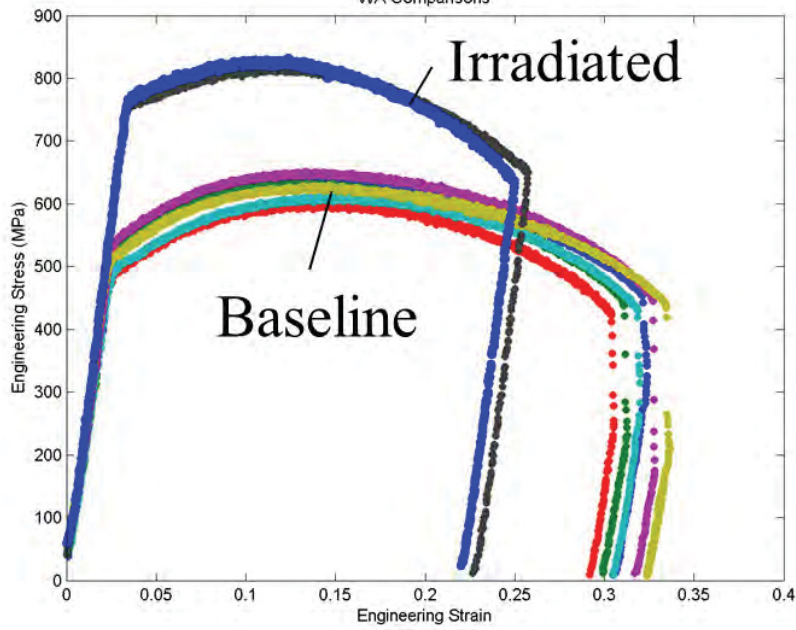
HB

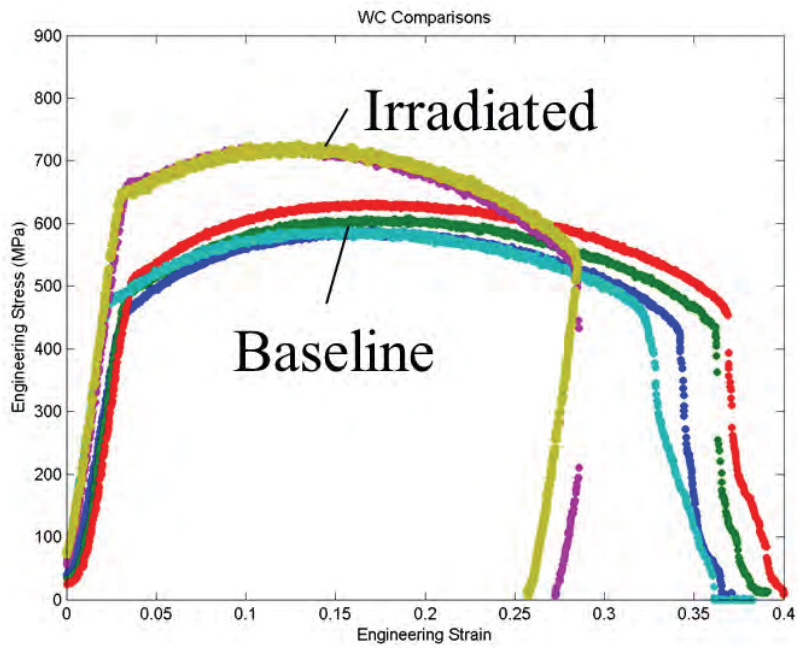
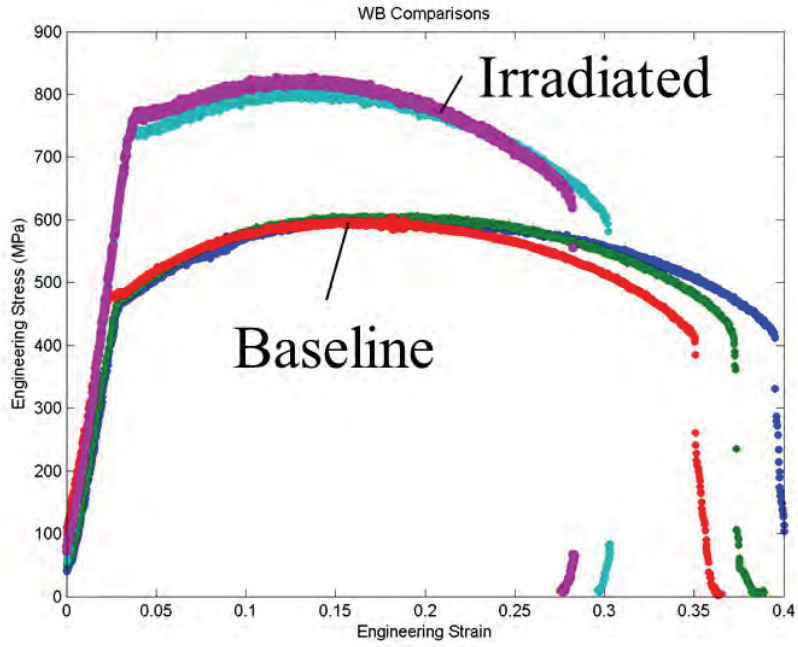


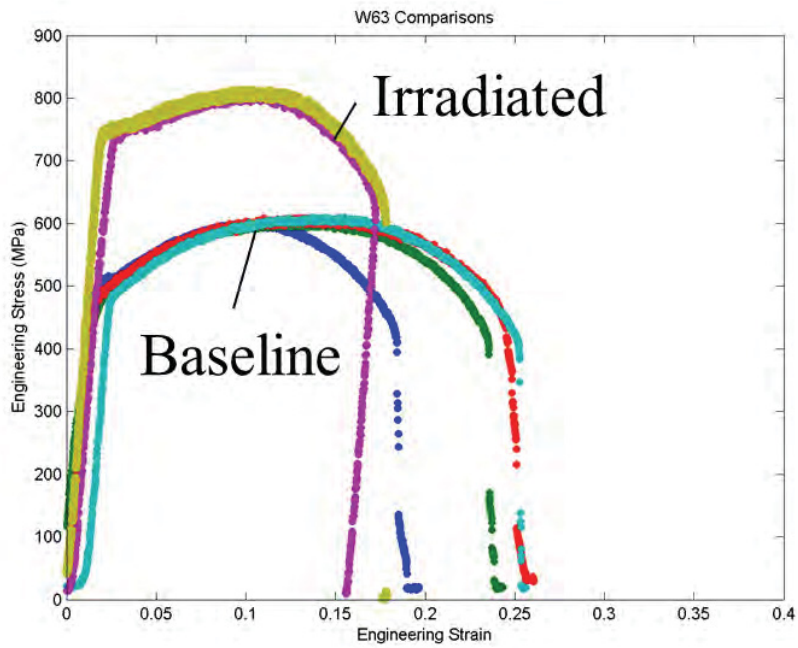
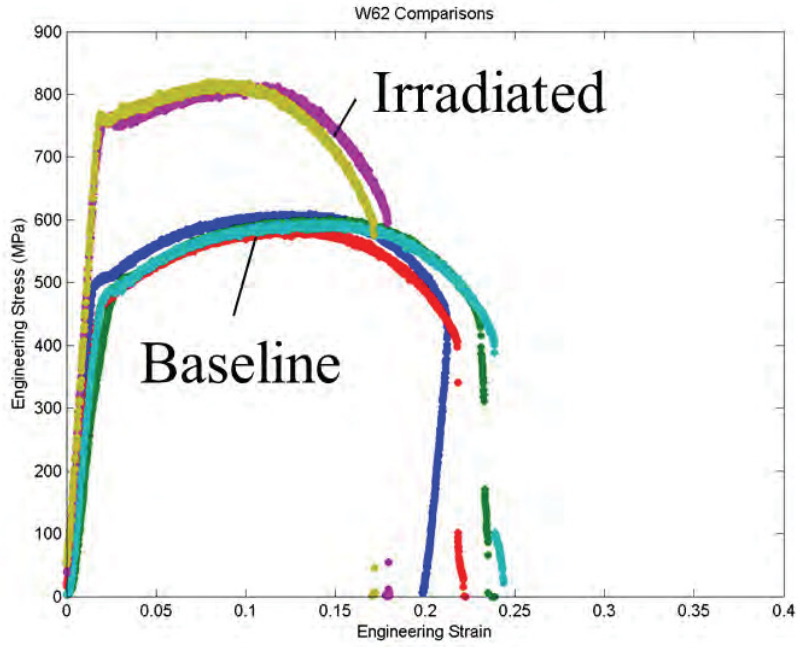
MP

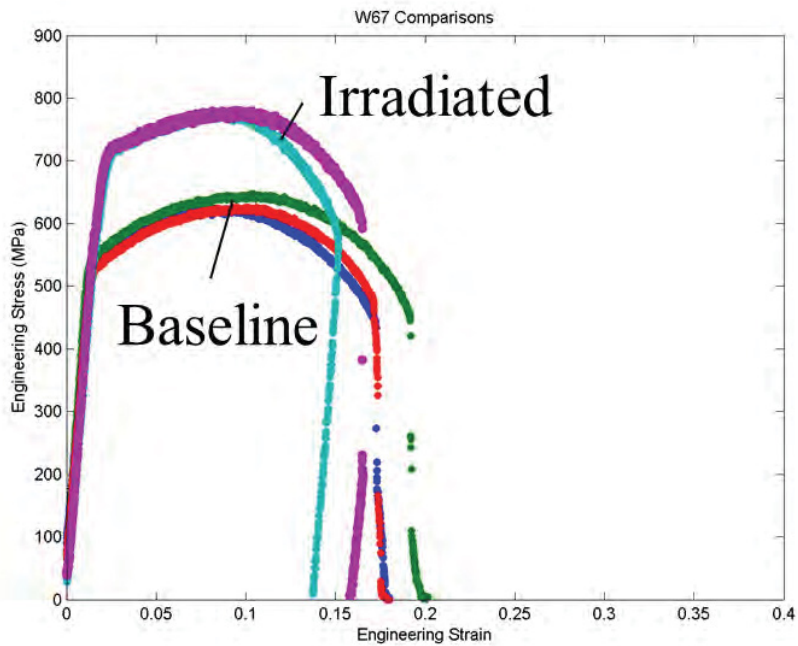
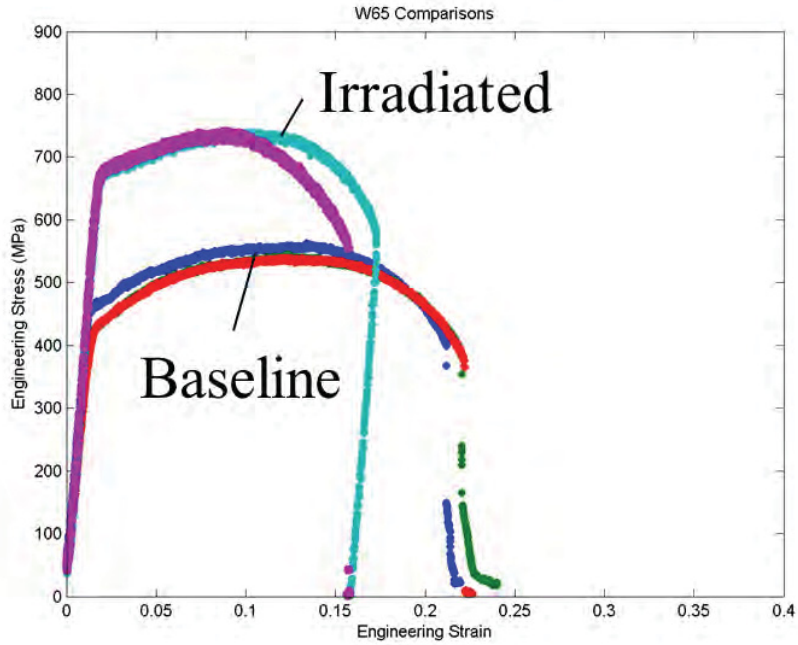


WA Comparisons

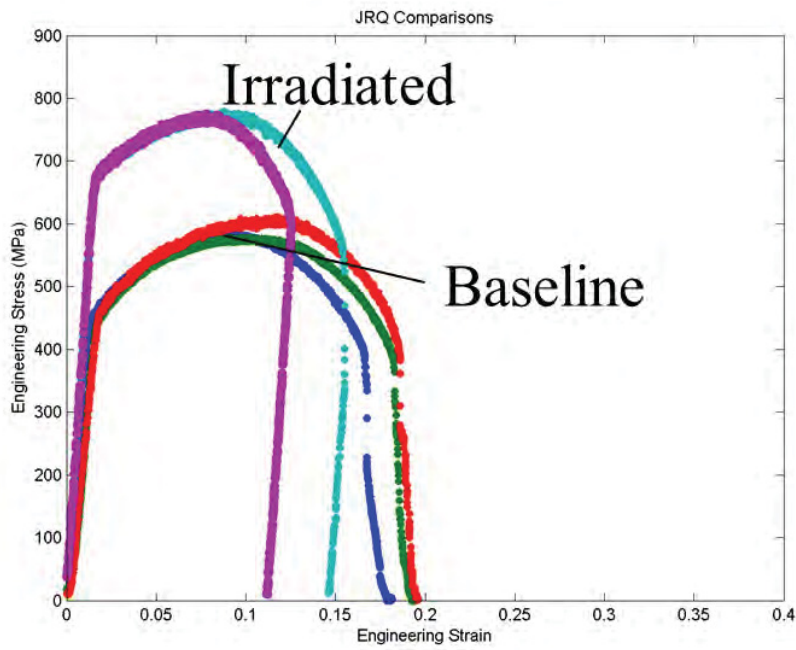
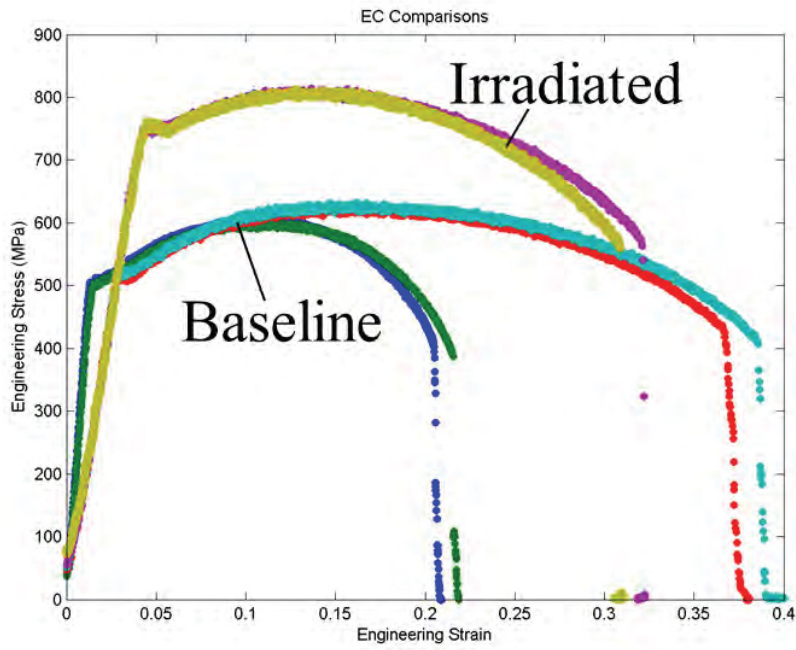


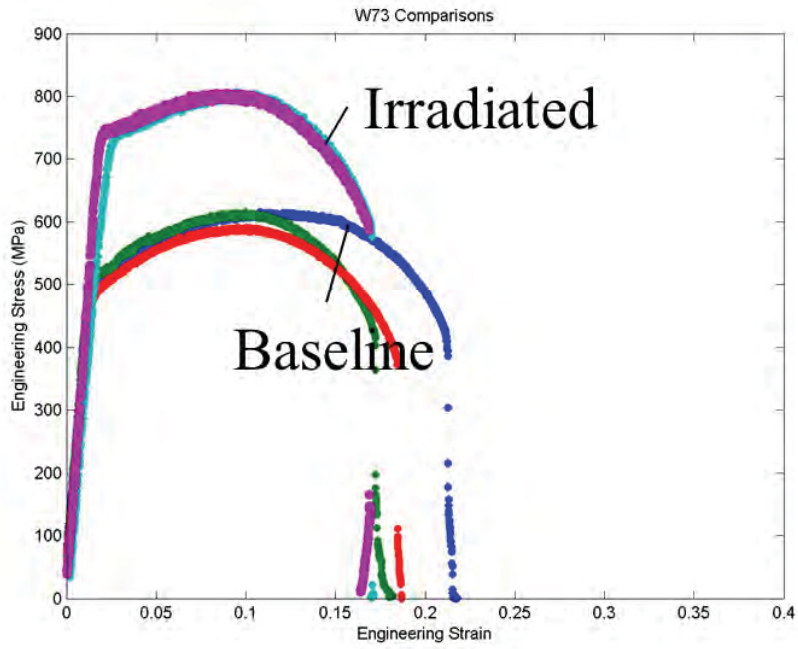




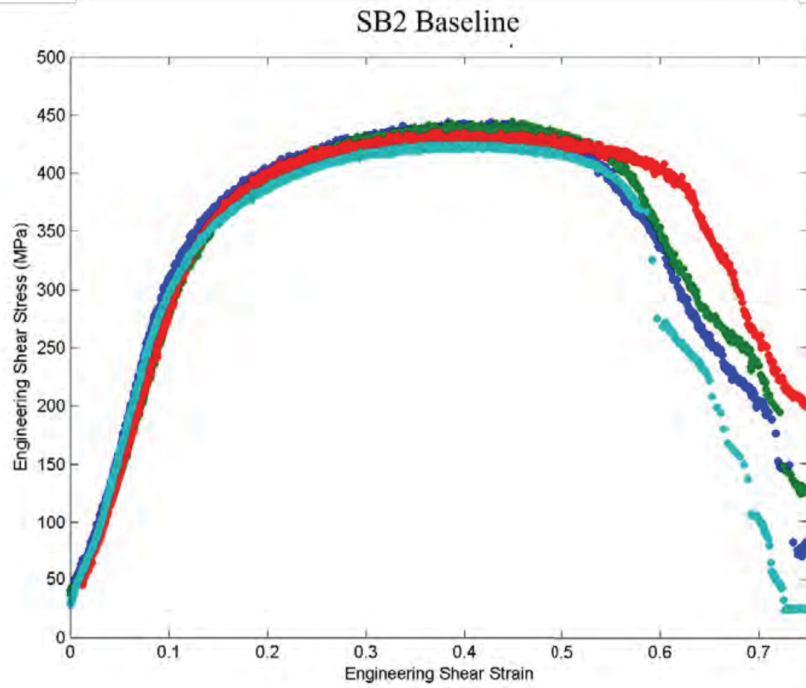
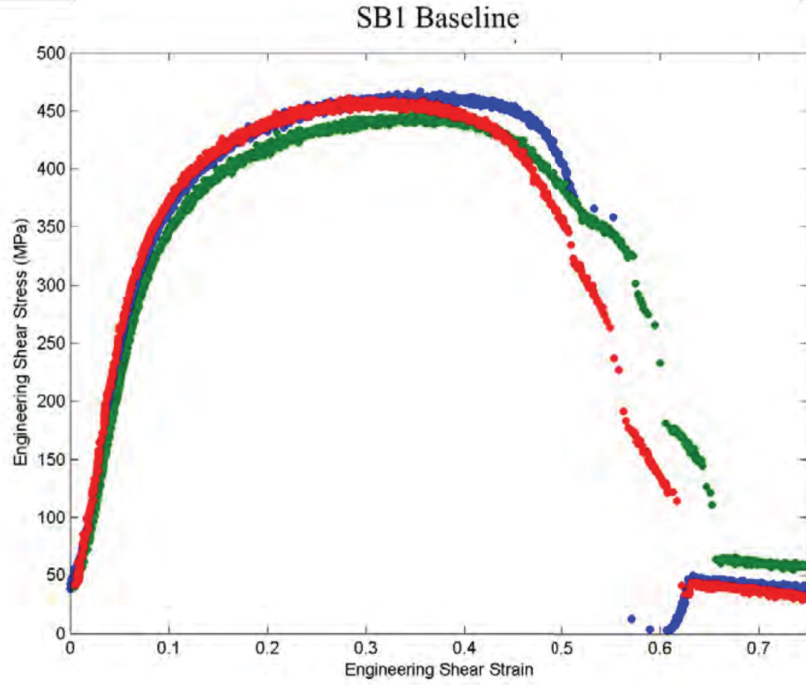


A.2 Comparison of Irradiated and Baseline Stress-Strain Curves for Program Alloys

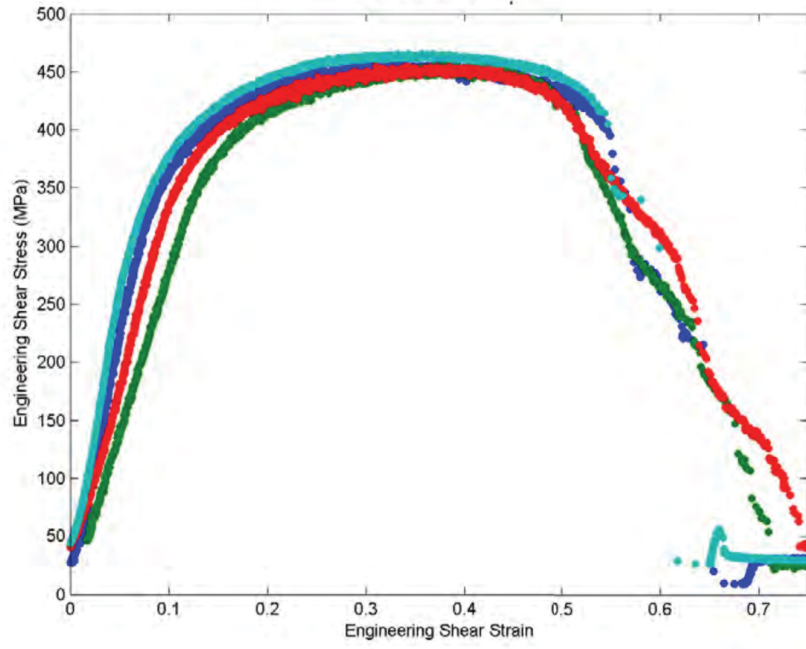




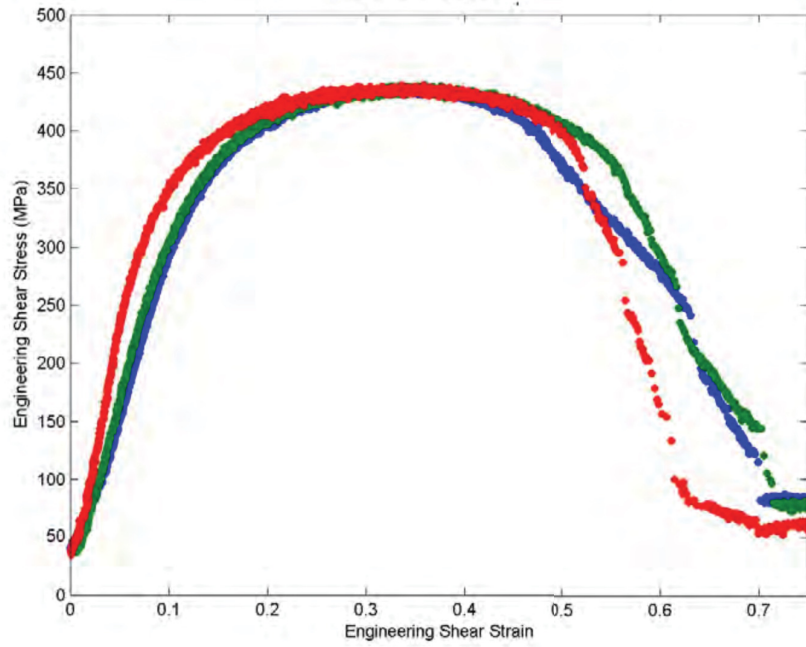
A.3 Shear Punch Curves for the Surveillance Baseline Alloys



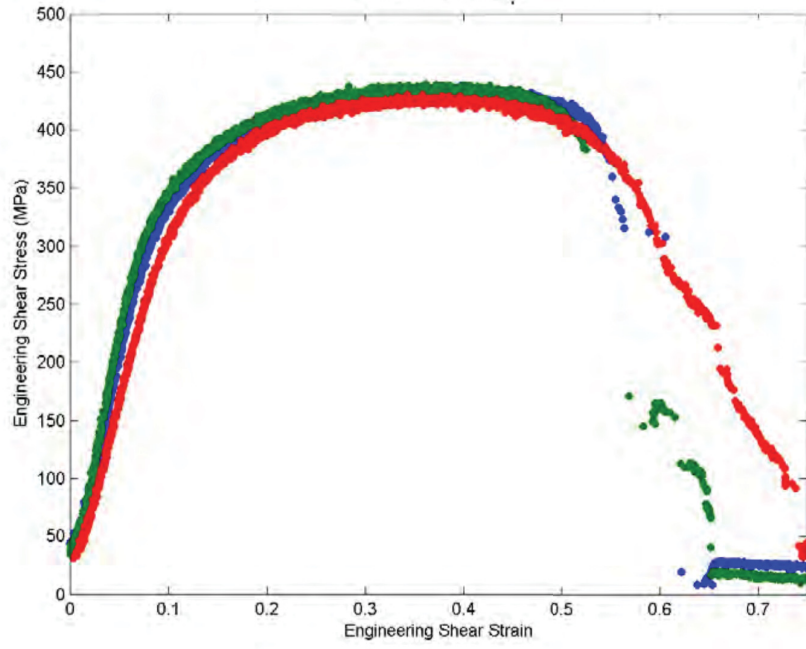
SB3 Baseline



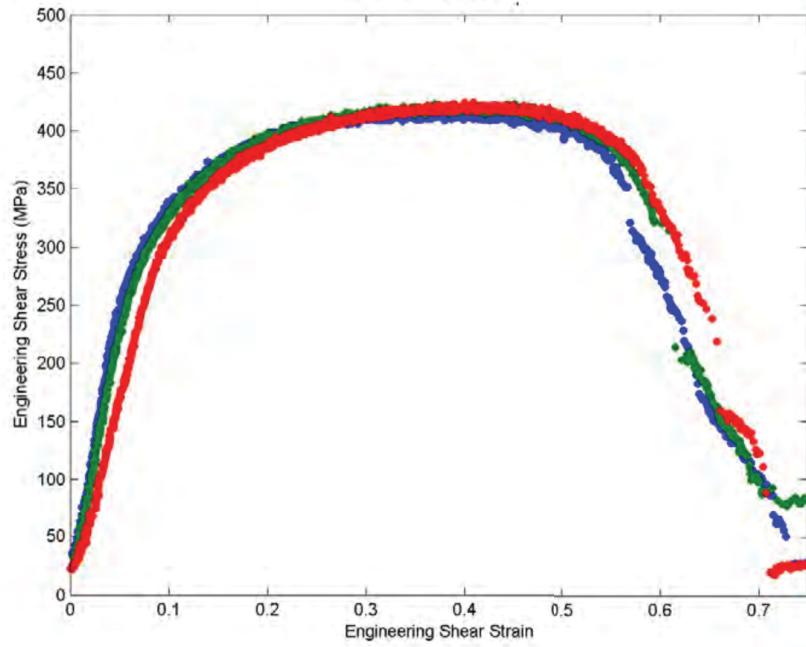
SW1 Baseline



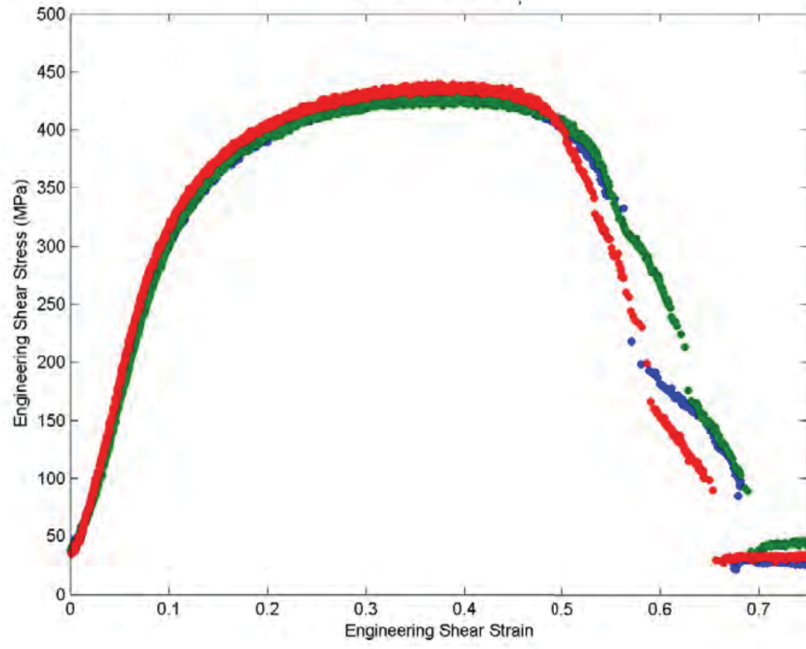
SW3 Baseline



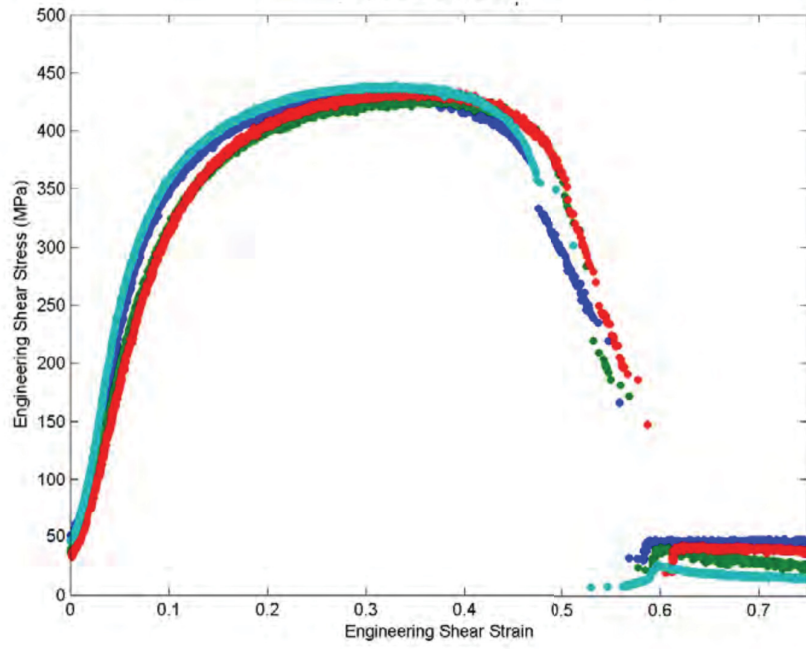
SW4 Baseline



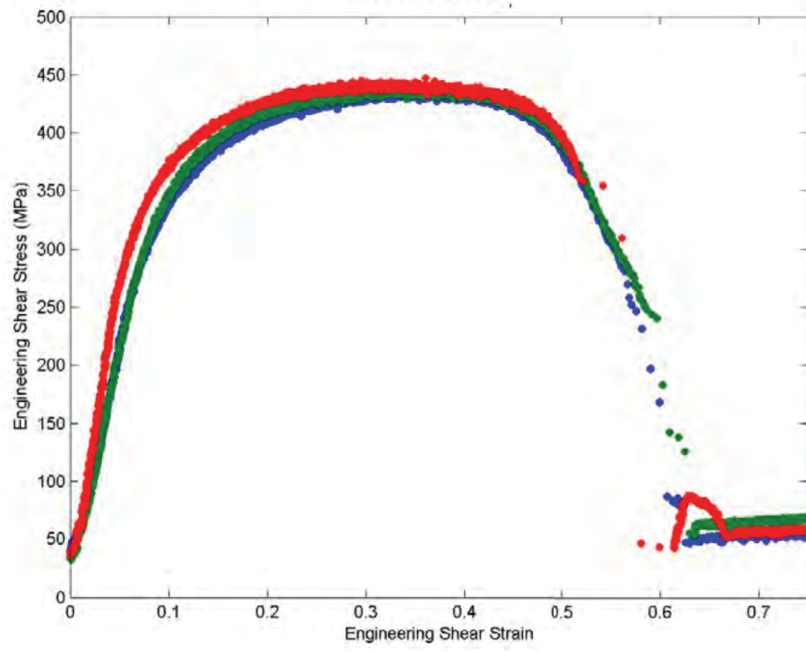
SW5 Baseline



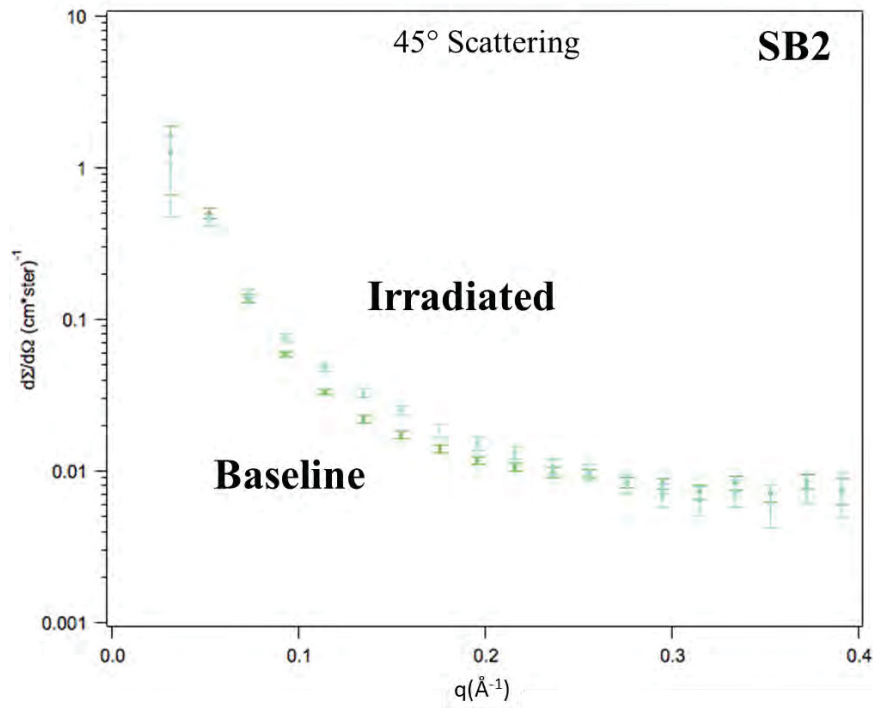
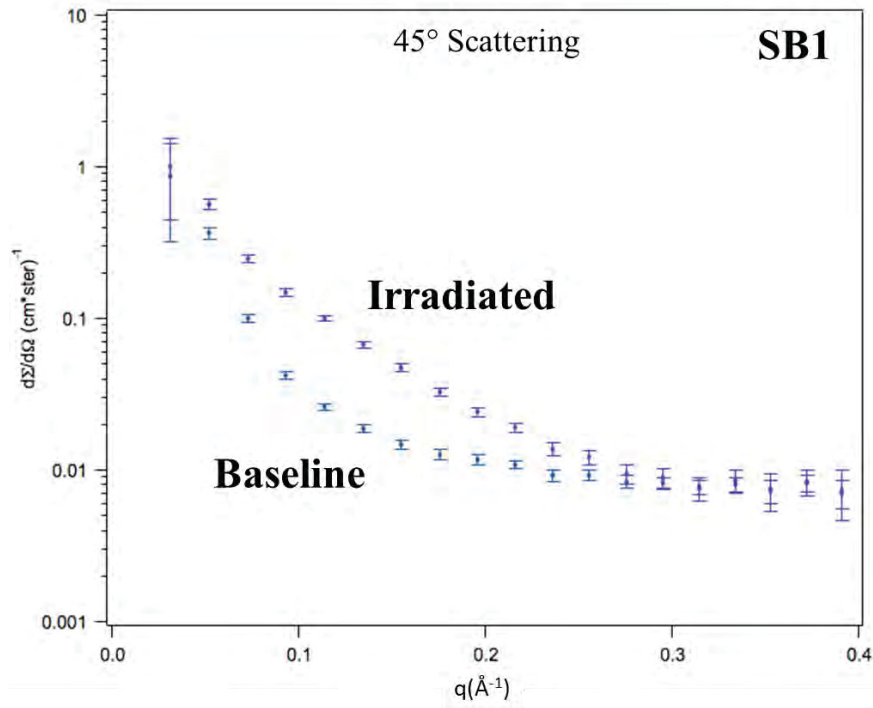
QC1 Baseline

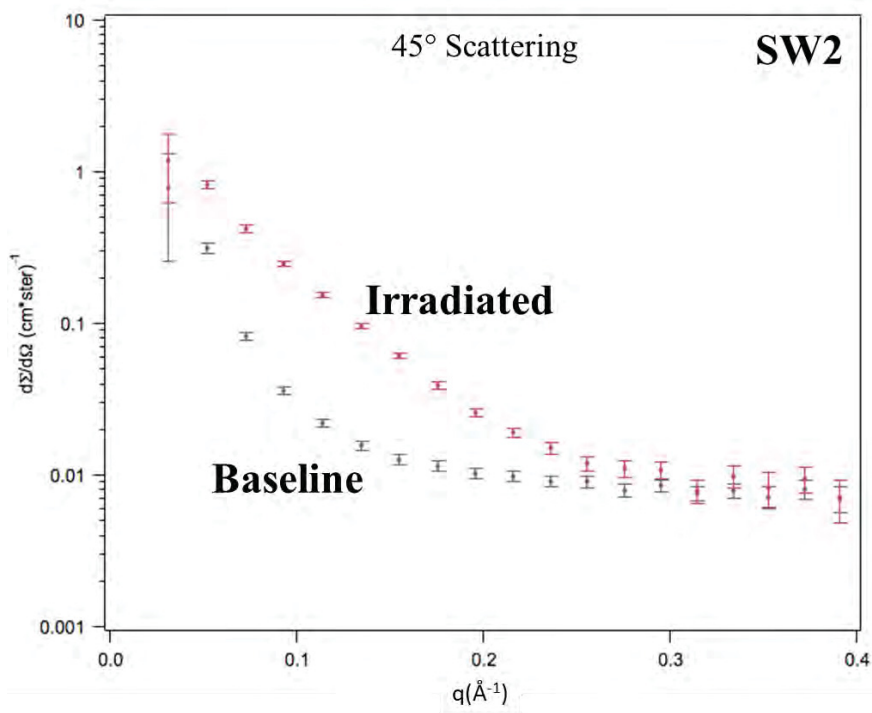
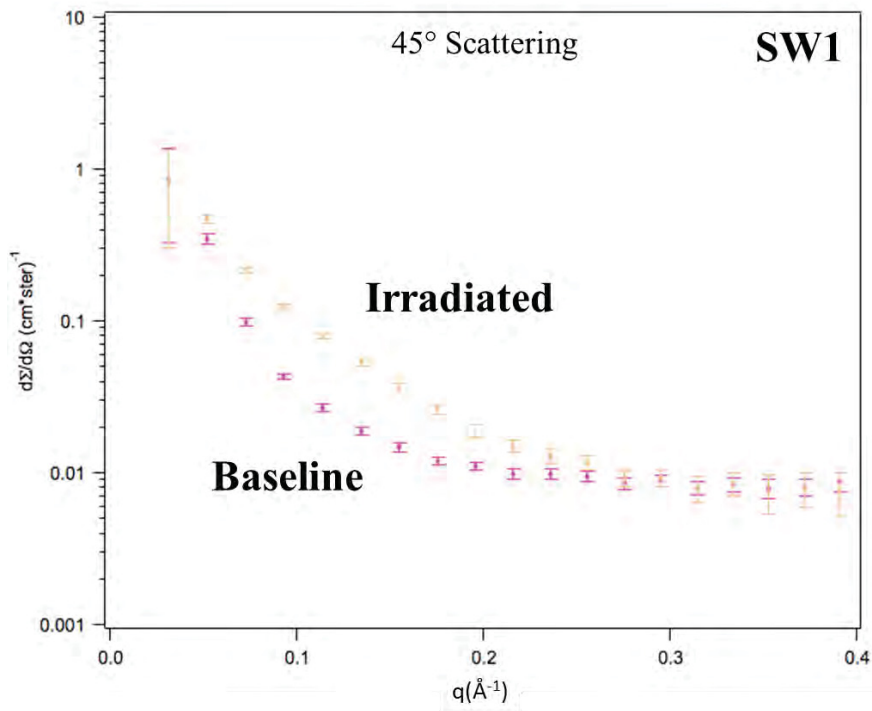


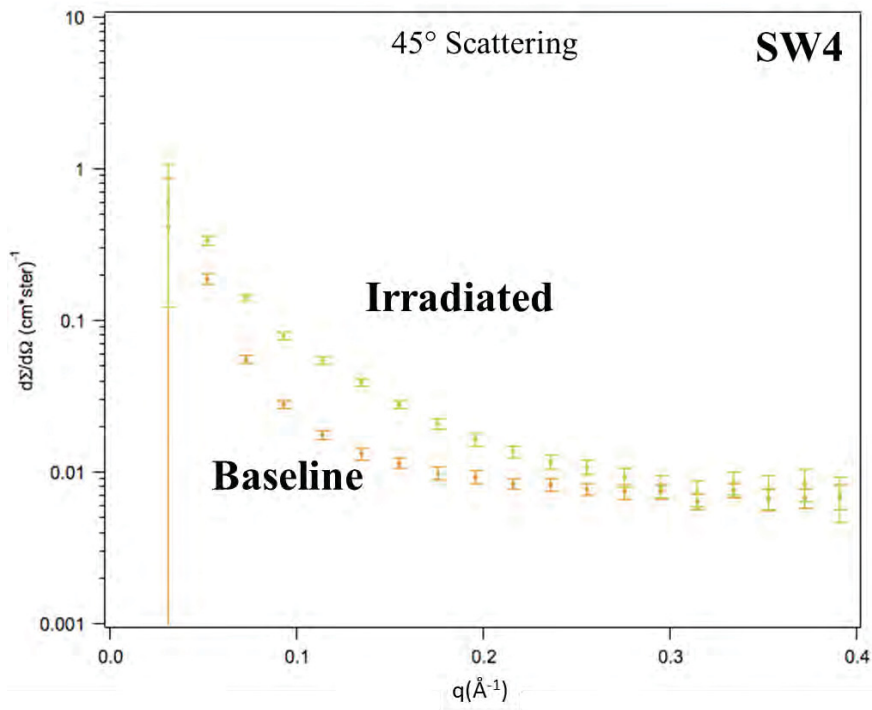
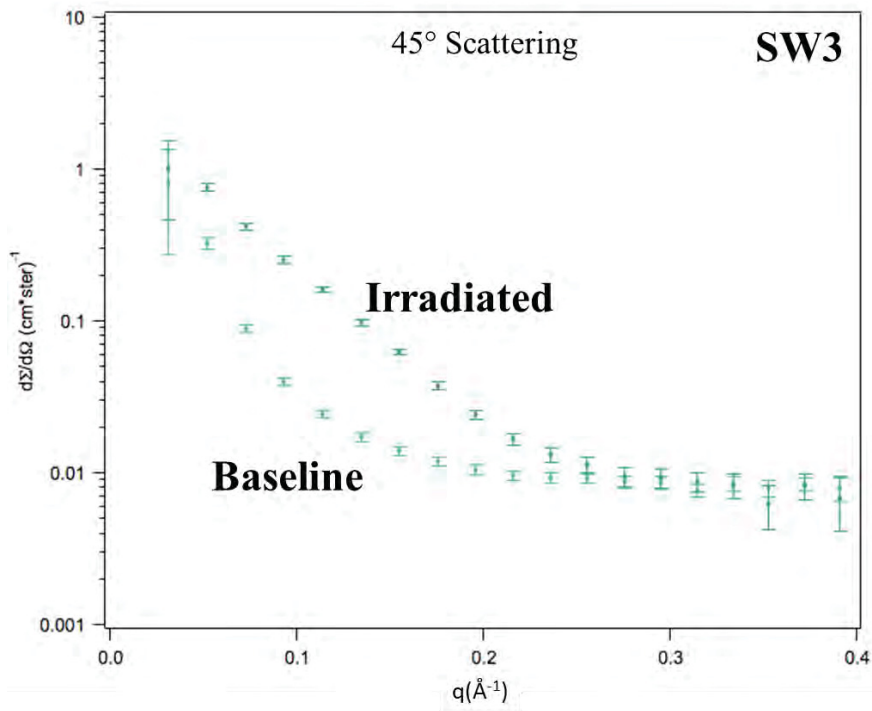
D3 Baseline

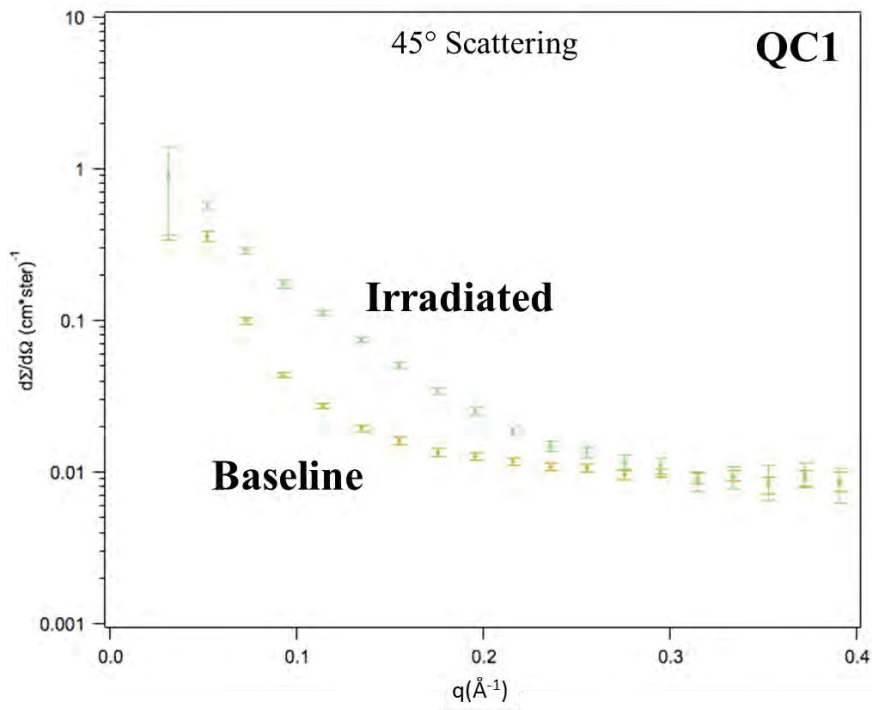
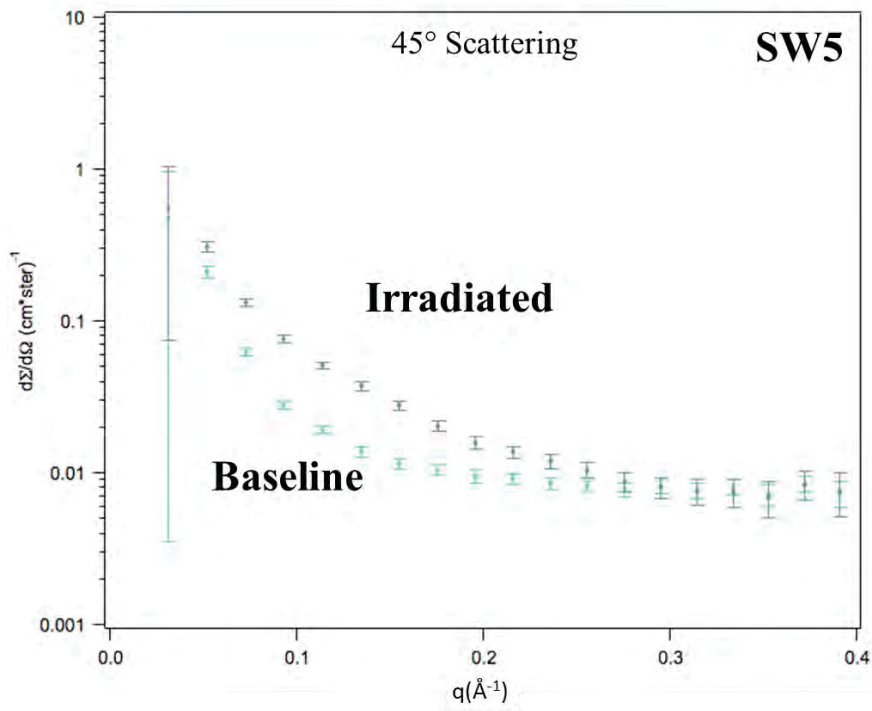


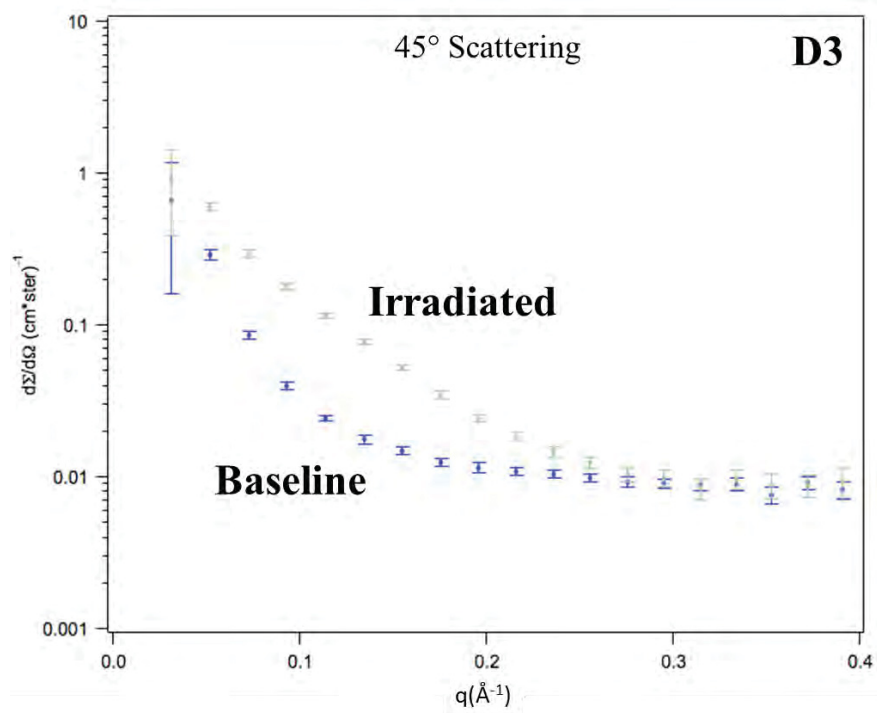
A.4 SANS Curves for the Surveillance Alloys at 45° with Respect to the Magnetic Field



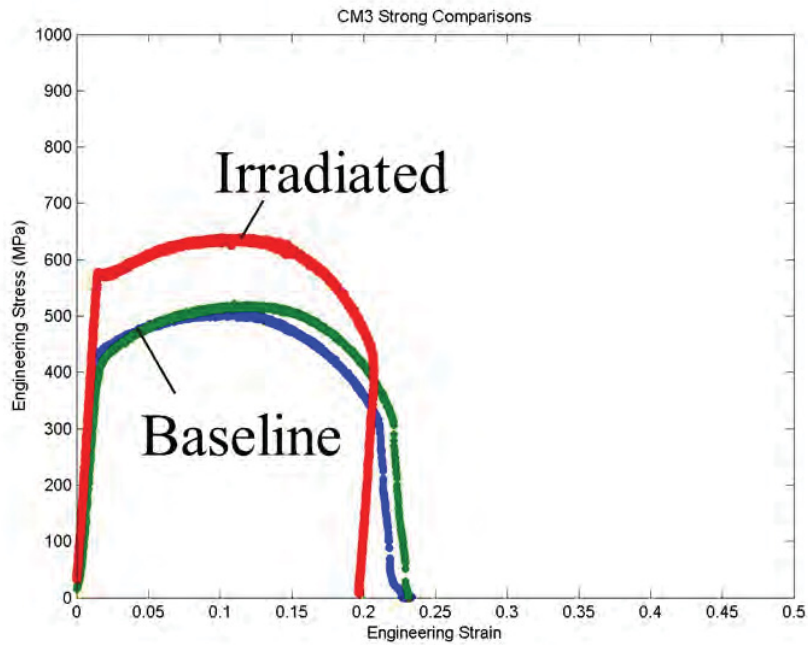
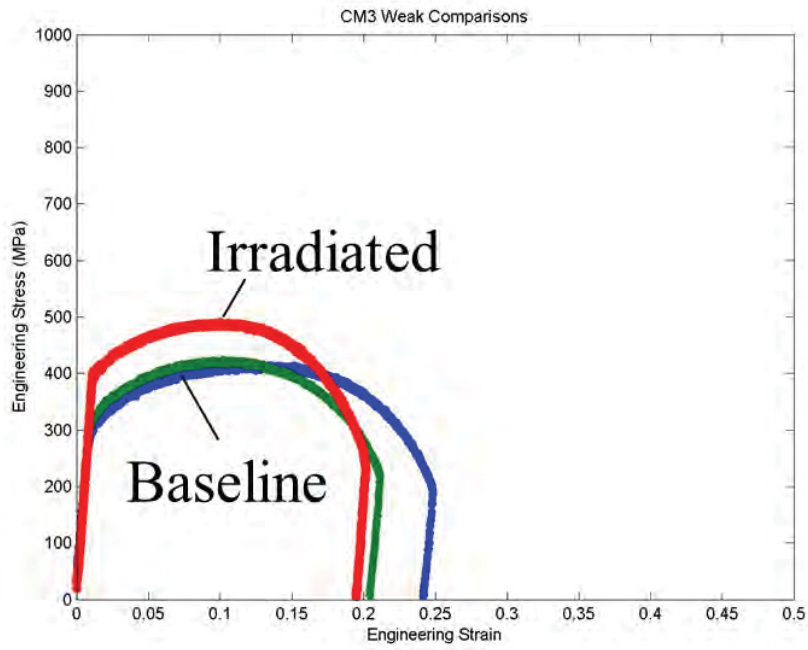


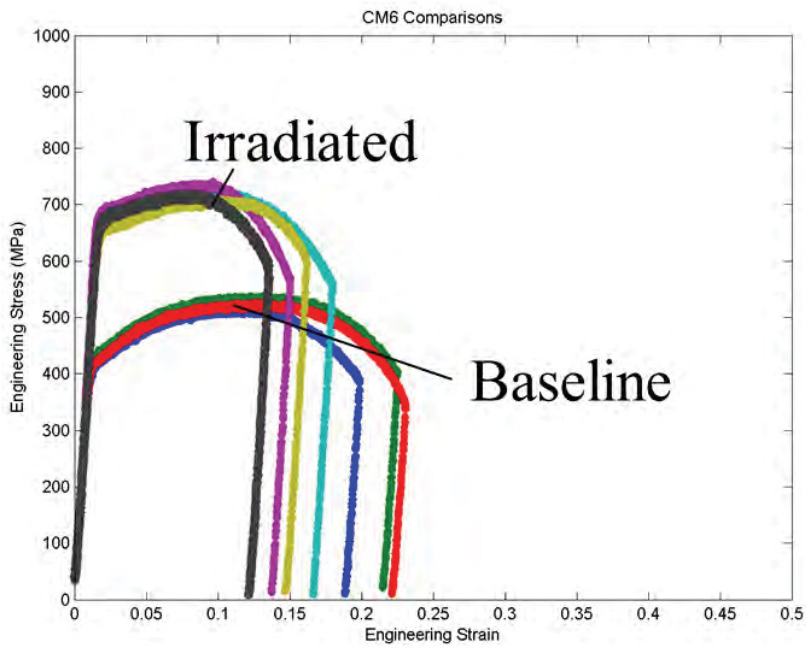
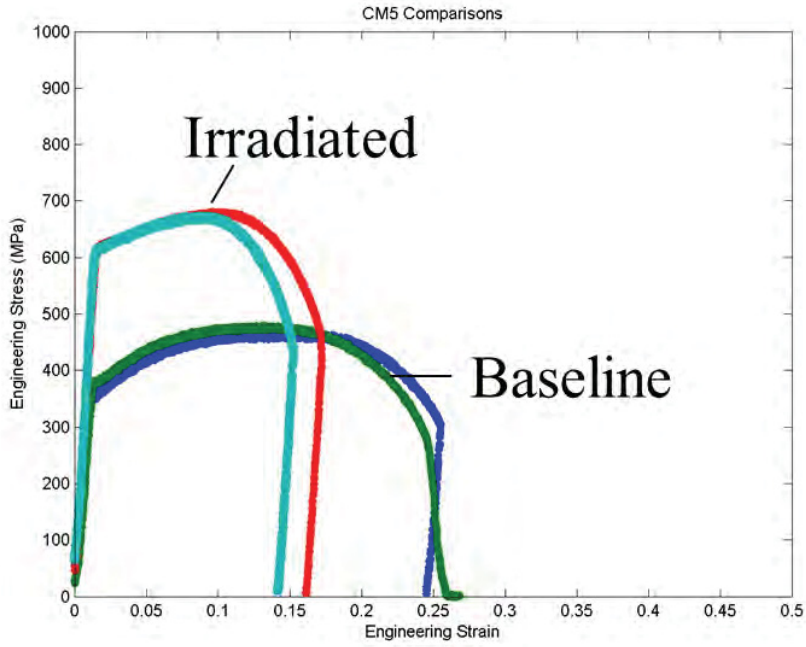


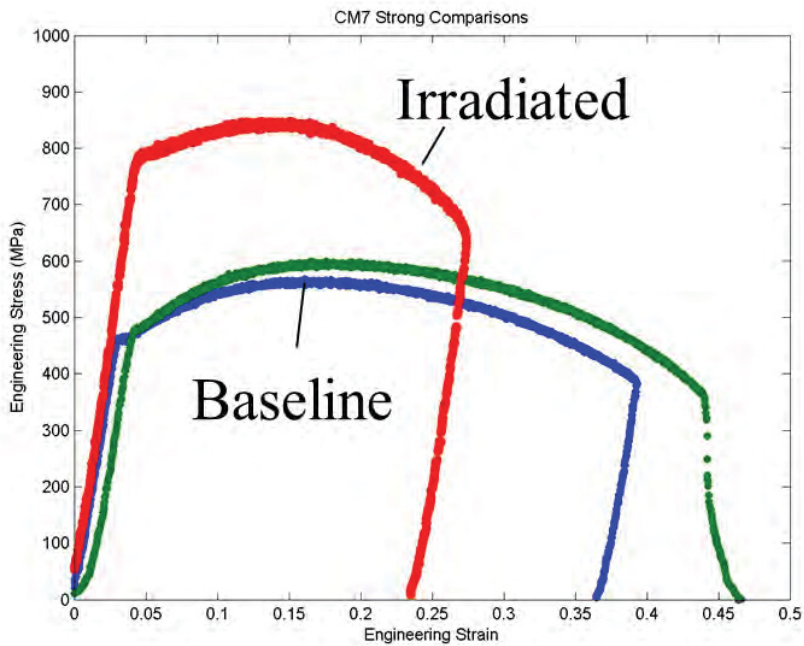
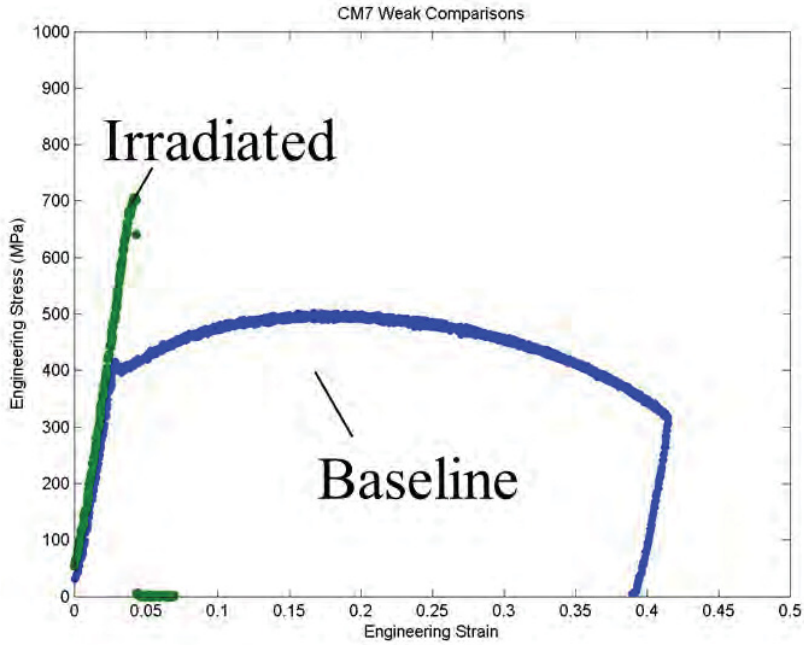


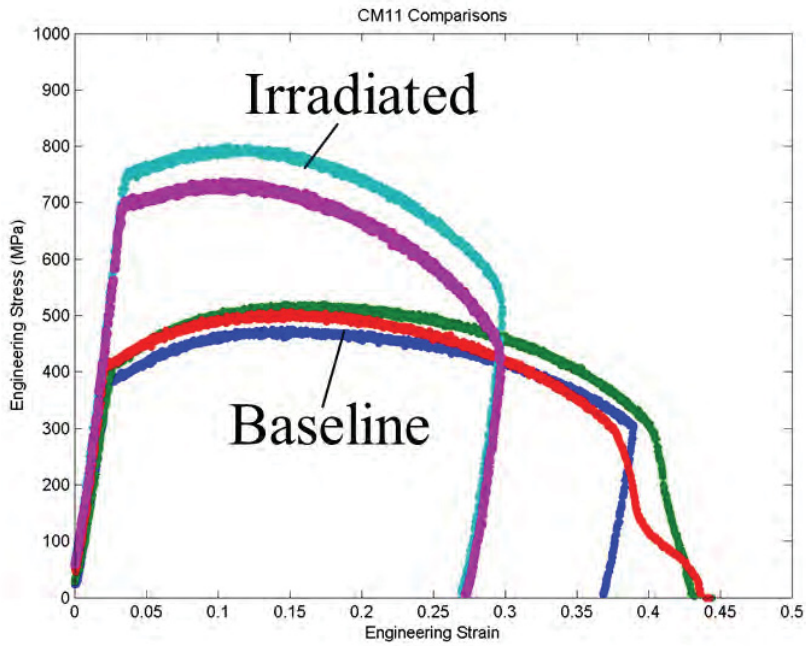
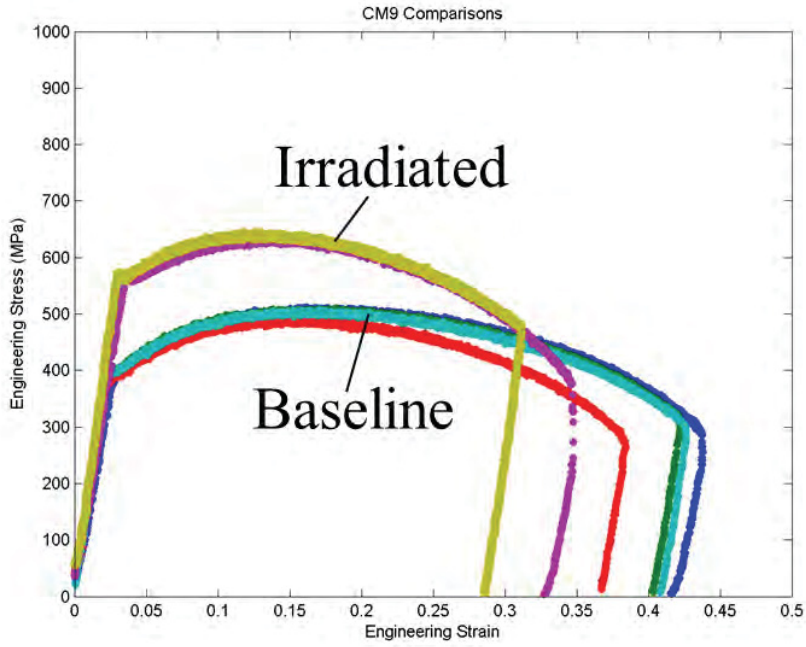


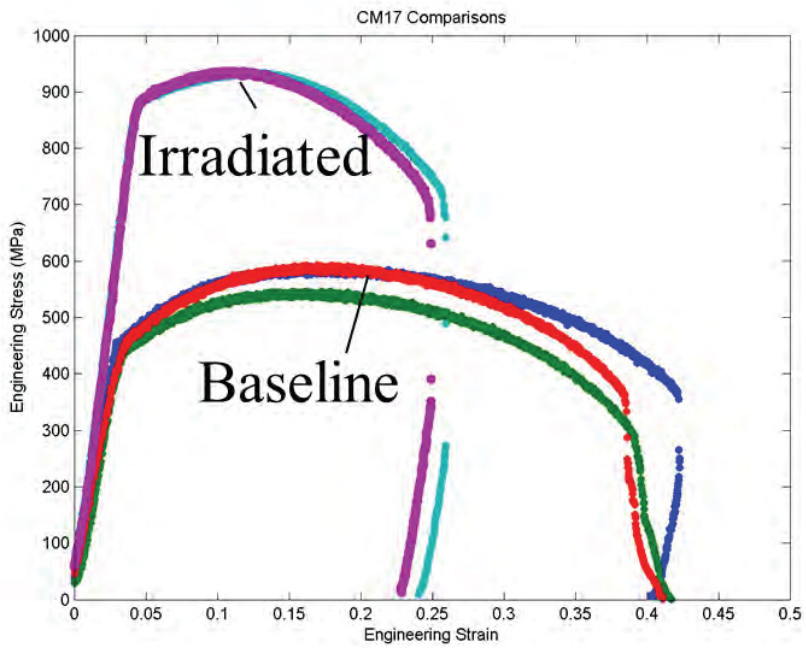
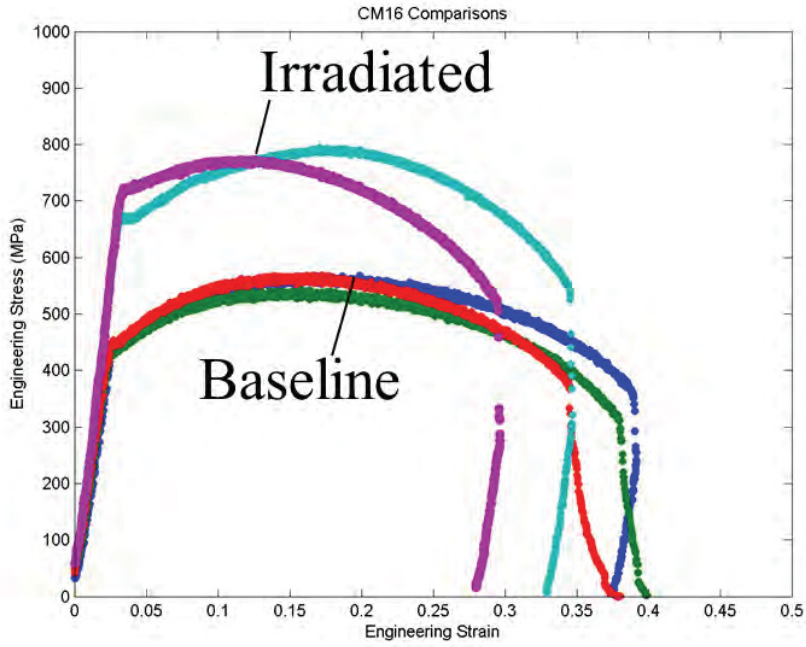
A.5 Comparison of Irradiated and Baseline Stress-Strain Curves for UCSB SMS

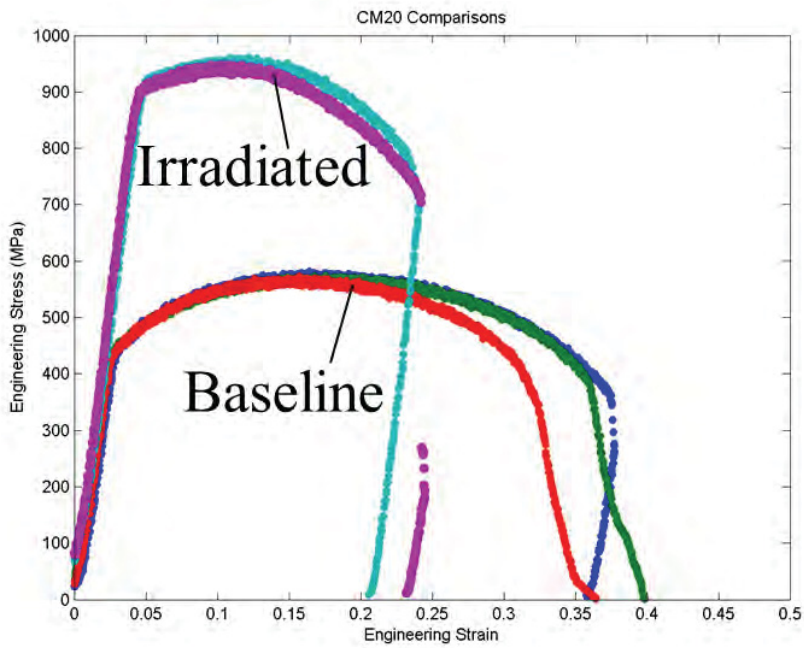
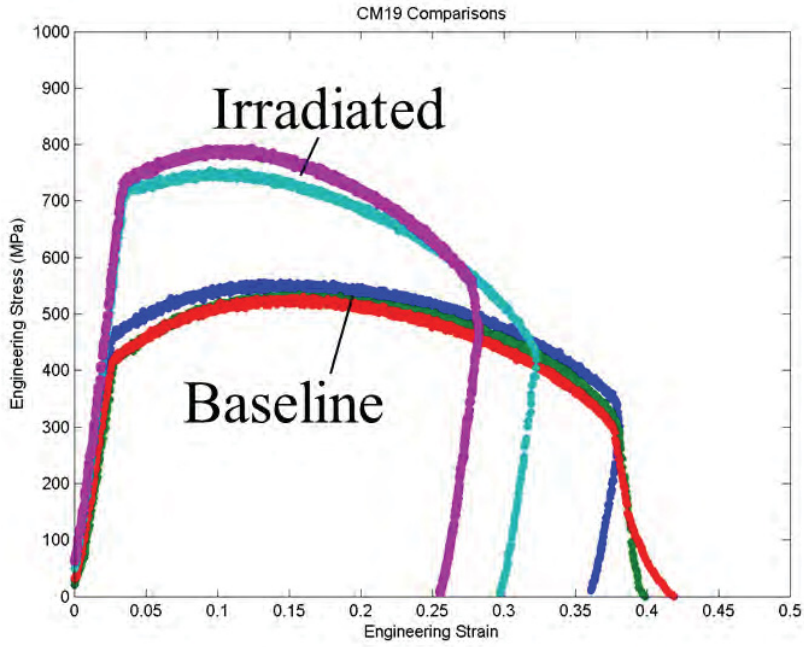


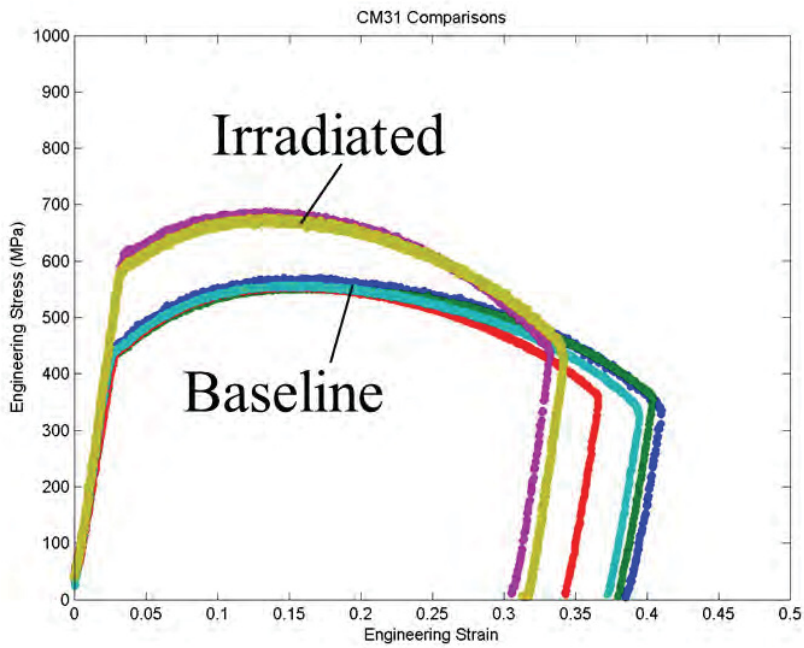
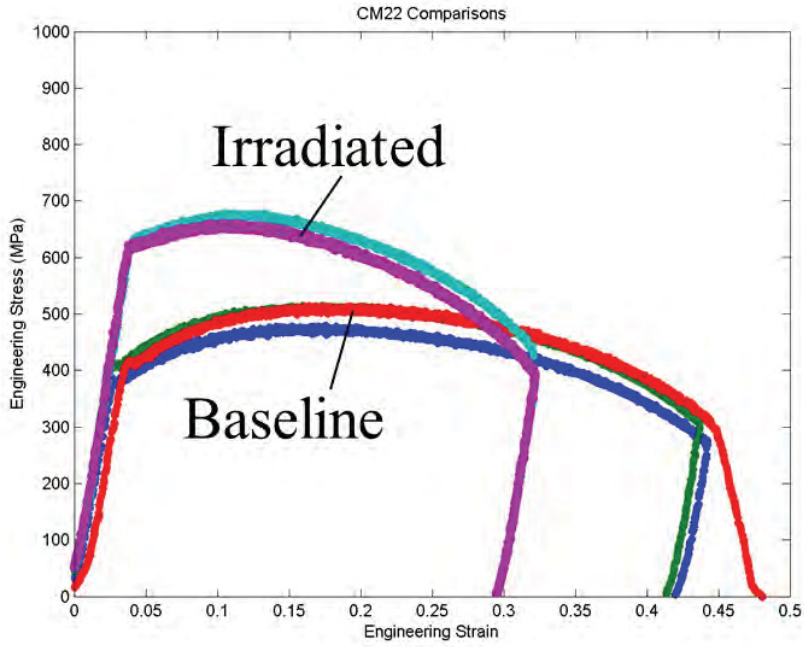


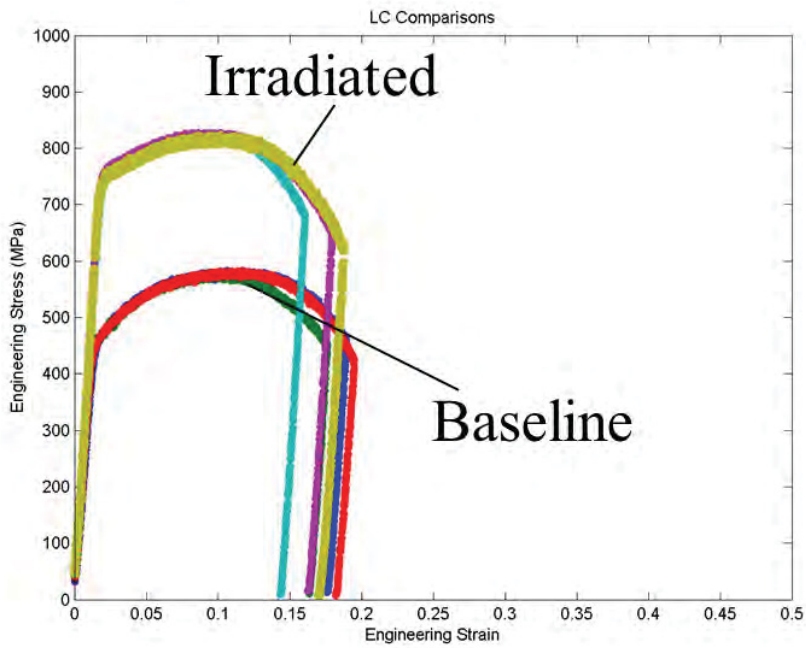
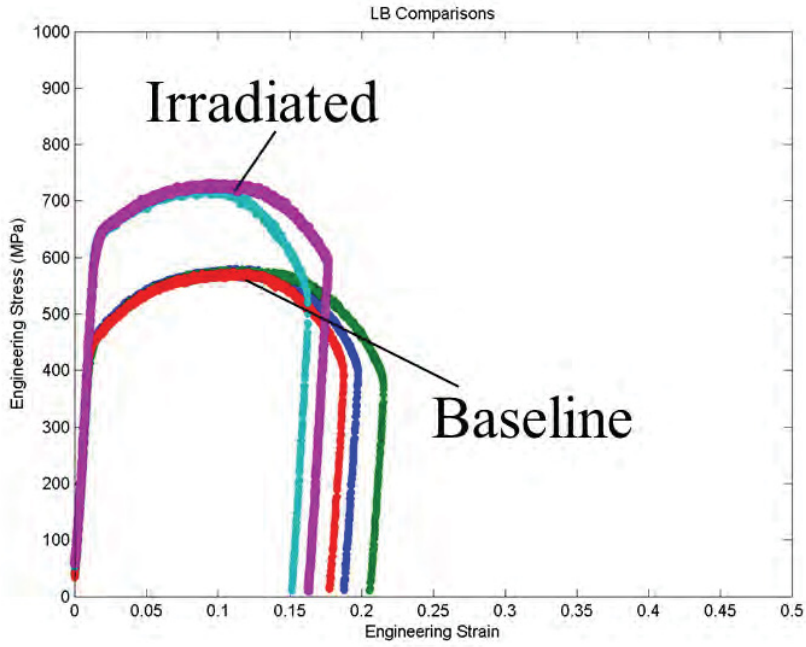


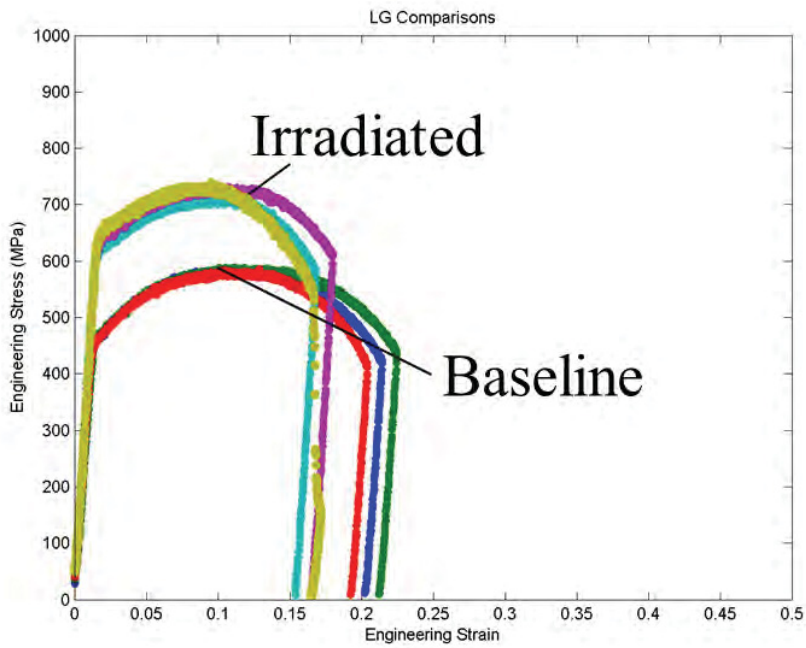
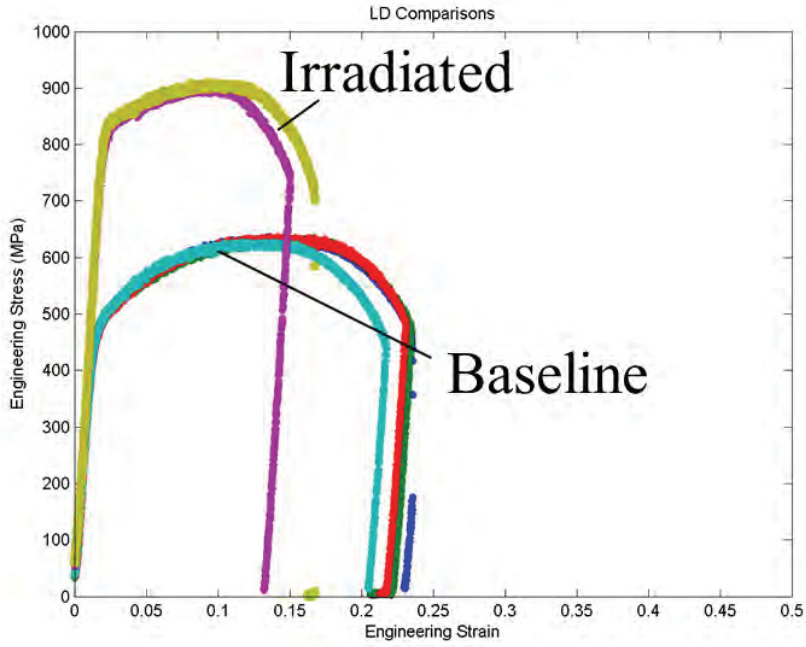


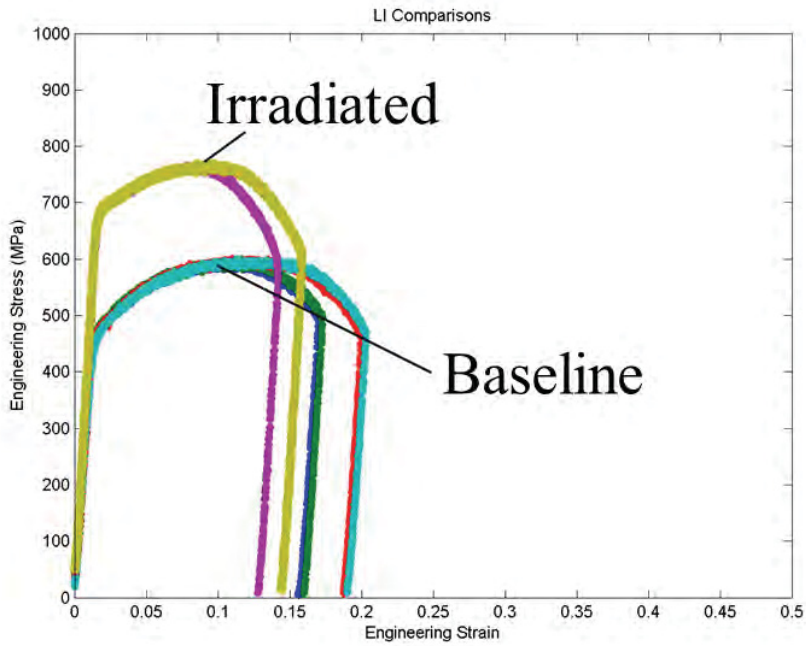
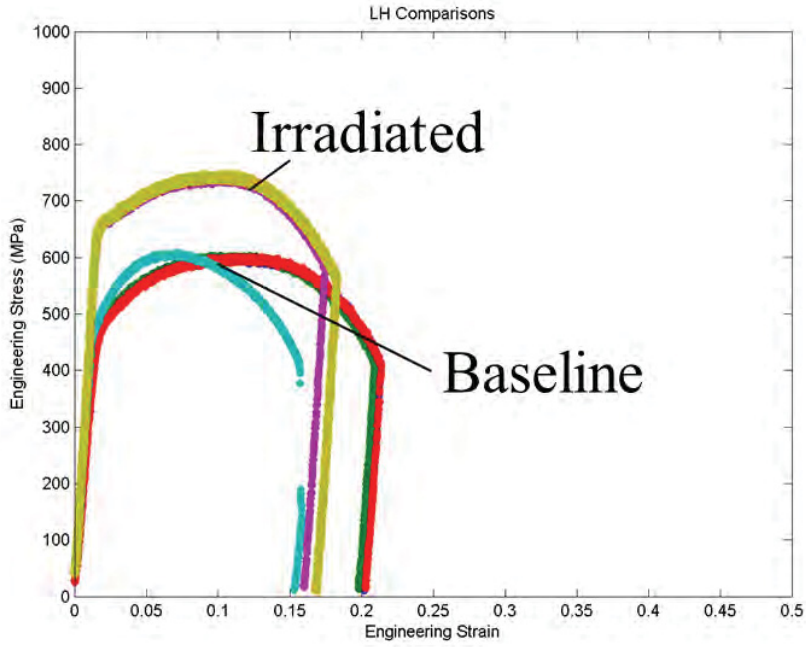


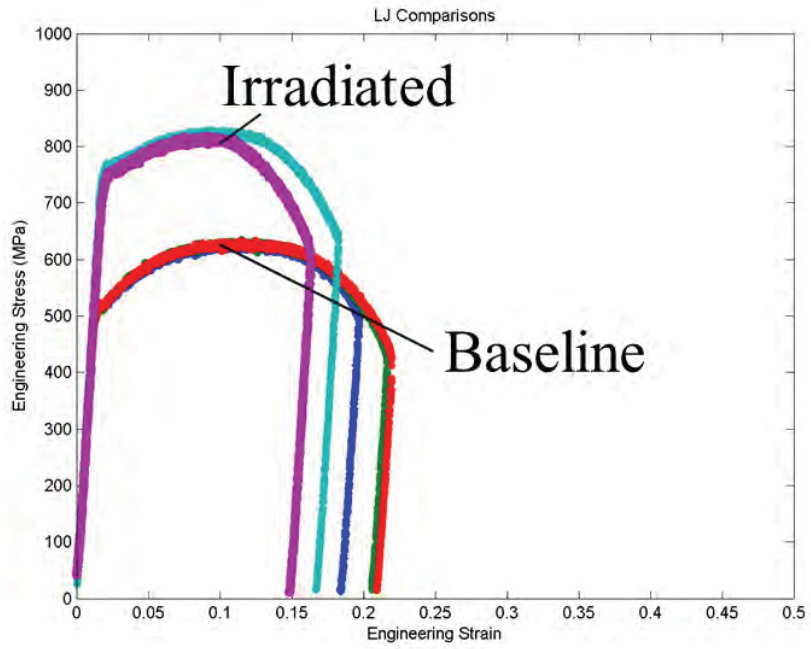












A.6 $\Delta\sigma_y$ versus fluence for the UCSB alloy matrix including a large number of data from previous test irradiations

